

**Targeting Phosphatidylserine for Positron Emission Tomography Imaging of Cell
Death: Annexin V versus Phosphatidylserine-Binding Peptides**

by

Amanda Christine Perreault

A thesis submitted in partial fulfillment of the requirements for the degree of

Master of Science

in

Experimental Oncology

Department of Oncology
University of Alberta

© Amanda Christine Perreault, 2016

ABSTRACT

There is currently no clinically approved, widely used molecular imaging agent for *in vivo* detection of cell death. Such an agent would be highly useful for early assessment of treatment efficacy in cancer patients, as well as for monitoring many other diseases in which cell death plays an important role. Phosphatidylserine (PS), a phospholipid that is normally confined to the inner leaflet of the cell membrane, becomes externalized on cells undergoing cell death. The accessibility of PS on dying cells makes it an attractive target for a cell death imaging probe. In this study, we have radiolabelled and evaluated several PS-targeting biomolecules as potential candidates for positron emission tomography (PET) imaging of chemotherapy-induced tumour cell death, including the well-known PS-targeting protein annexin V and three literature-reported PS-binding peptides.

Wild-type annexin V was labelled with fluorine-18 (^{18}F) using two techniques: a random labelling approach that targets any of the 23 primary amines present on the protein, and a site-selective labelling approach that targets the protein's single cysteine residue. Using an EL4 mouse lymphoma cell binding assay, we determined that both labelling techniques produced an ^{18}F -labelled product that could detect cell death induced by chemotherapeutic agent camptothecin, and that labelling technique did not have a significant effect on the ability of ^{18}F -labelled annexin V to bind to PS.

Using a well-established mouse EL4 tumour model of cell death induced by combination treatment with etoposide and cyclophosphamide, we were unable to demonstrate the ability of ^{18}F -annexin V to image EL4 tumour cell death *in vivo*. This is in contrast to previous reports that have shown successful preclinical imaging of

chemotherapy-induced cell death using ^{18}F -labelled wild-type annexin V. Possible reasons for our negative result include poor penetration of ^{18}F -annexin V into EL4 tumours, lack of sufficient Ca^{2+} concentrations required for ^{18}F -annexin V binding to PS, and lack of imaging during the time of greatest PS exposure.

We also investigated three literature-reported PS-binding peptides as potential candidates for development of a PET agent for imaging cell death: LIKKPF, PGDLSR, and PS-binding peptide 6 (PSBP-6). We developed a novel competitive radiometric PS binding assay that revealed very poor PS-binding affinities of LIKKPF- and PGDLSR-based peptide conjugates, while PSBP-6-based conjugates showed more favourable affinities.

We radiolabelled each of the PS-binding peptides with positron-emitting radionuclides to develop them for PET imaging. Hexapeptides PGDLSR and LIKKPF were successfully labelled with ^{18}F , but neither of these radiolabelled peptides showed suitable stability *in vivo*. PSBP-6 was conjugated with metal chelator 1,4,7-triazacyclononane-triacetic acid (NOTA) to be labelled with radiometals gallium-68 (^{68}Ga) and copper-64 (^{64}Cu). Both ^{68}Ga -NOTA-PSBP-6 and ^{64}Cu -NOTA-PSBP-6 showed much better *in vivo* stability than the radiolabelled hexapeptides.

Our cell binding assay showed that ^{64}Cu -NOTA-PSBP-6 could detect camptothecin-induced cell death in the absence of Ca^{2+} . However, supplementation with Ca^{2+} seemed to enhance the ability of ^{64}Cu -NOTA-PSBP-6 to detect cells undergoing cell death. Using our EL4 lymphoma tumour model, we found that ^{64}Cu -NOTA-PSBP-6 uptake was significantly higher in tumours receiving chemotherapeutic treatment compared to controls, which was apparent 5 minutes after injection with the radiopeptide.

However, tumour retention of ^{64}Cu -NOTA-PSBP-6 was poor, likely due to a combination of low affinity for PS, rapid proteolytic breakdown in the plasma, and fast blood clearance.

We also labelled PSBP-6 with fluorescein isothiocyanate (FITC), and flow cytometry studies showed significantly higher binding of this fluorescent peptide to EL4 cells treated with camptothecin compared to untreated cells. Fluorescence microscopy studies revealed that FITC-PSBP-6 is not internalized while the cell membrane is still intact, but remains bound to the cell membrane.

Further evaluation of the ability of ^{18}F -labelled wild-type annexin V to detect tumour cell death *in vivo* will require optimization of the current EL4 model or the use of other preclinical tumour models of therapy-induced cell death. On the other hand, ^{64}Cu -labelled PS-binding peptide PSBP-6 shows promise as an alternative probe for imaging cell death *in vivo* using PET. Modifications to further improve the PS-binding affinity, metabolic stability, blood clearance profile and tumour retention of ^{64}Cu -NOTA-PSBP-6 are needed in order to “fine-tune” this radiopeptide for optimal imaging.

PREFACE

Parts of this thesis have been published or accepted for publication as the following:

Perreault A, Knight J, Wang M, Way J, Wuest F. ^{18}F -labeled wild-type annexin V: Comparison of random and site-selective radiolabeling methods. *Amino Acids*. 2016;48(1):65-74. doi: 10.1007/s00726-015-2068-0. Knight J developed the radiolabelling procedures, and I assisted with data collection and analysis of radiolabellings. I performed/analyzed the flow cytometry and confocal microscopy studies as well as the cell binding assays. Wang M optimized the cell binding assay procedure and assisted with cell-based studies. I was responsible for manuscript composition, and Knight J assisted with manuscript edits. Way J synthesized the [^{18}F]SFB used for radiolabelling. Wuest F was the supervisory author and was involved with concept formation and manuscript composition.

Wuest M, **Perreault A**, Kapy J, Richter S, Foerster C, Bergman C, Way J, Mercer J, Wuest F. Radiopharmacological evaluation of ^{18}F -labeled phosphatidylserine-binding peptides for molecular imaging of apoptosis. *Nucl Med Biol*. 2015;42(11):864-74. doi: 10.1016/j.nucmedbio.2015.06.011. Wuest M performed the animal experiments and was responsible for data analysis/interpretation and manuscript composition. I developed the competitive radiometric PS binding assay and was responsible for data collection and analysis of the assays. Kapy J collected and analyzed data for radiolabelling experiments, cell binding assays and radiopeptide stability studies. Richter S assisted with radiolabelling procedure optimization and radiopeptide stability studies. Foerster C developed and performed ^{64}Cu -NOTA-annexin V synthesis. Bergman C synthesized the peptides. Way J synthesized the ^{18}F -containing prosthetic groups. Mercer

J and Wuest F were the supervisory authors and were involved with concept formation and manuscript composition.

Perreault A, Richter S, Foerster C, Bergman C, Wuest M, Wuest F. ⁶⁸Ga-labeled peptides for targeting phosphatidylserine (PS) in apoptosis. *J Labelled Comp Radiopharm.* 2015;58(1):S131. I performed the experiments, analyzed the data and wrote the abstract. Richter S assisted with radiolabelling and metabolic stability studies. Wuest M assisted with metabolic stability studies. Foerster C prepared the ⁶⁴Cu-NOTA-annexin V used in PS binding assays. Bergman C synthesized the peptides used in PS binding assays. Wuest F was the supervisory author and was involved with concept formation and abstract composition.

Foerster C, **Perreault A**, Wuest M, Bergman C, Wuest F. A novel radiometric phosphatidylserine (PS) binding assay based on [⁶⁴Cu]Cu-NOTA-annexin-V. *Nucl Med Biol.* 2014;41(7):642–3. doi:10.1016/j.nucmedbio.2014.05.126. Foerster C was responsible for the radiochemistry and wrote the abstract. I was responsible for the PS binding assays. Wuest M assisted with data analysis. Bergman C synthesized the peptides used in the PS binding assays. Wuest F was the supervisory author and was involved with concept formation and abstract composition.

Knight J, **Perreault A**, Wang M, Way J, Wuest F. Radiolabeling annexin-V with fluorine-18: random and site-selective approaches. *J Labelled Comp Radiopharm.* 2013;56(1):S159. Knight J and I were the primary data collectors, Knight J wrote the abstract, and I contributed to abstract edits. Wang M assisted with cell based studies. Way J synthesized the ¹⁸F-containing prosthetic groups. Wuest F was the supervisory author and was involved with concept formation and abstract composition.

ACKNOWLEDGEMENTS

First and foremost, I would like to thank my supervisor, Dr. Frank Wuest, for taking me on as a student and providing me with constant guidance and support throughout my entire thesis project. I feel extremely fortunate to have been a part of his lab group and a part of NSERC-CREATE cMIP, as I have been afforded so many special and unique opportunities, such as attending conferences, sharing and collaborating with other research groups, and attending various professional development training seminars. This research project and all of these opportunities would not have been possible without the financial support provided by NSERC-CREATE cMIP.

I would also like to thank Dr. James Knight, who graciously mentored me when I first began this project and patiently trained me in radiochemistry. I had very little research experience when he took me under his wing, and I am very grateful for his guidance and kindness while working together on the annexin V project. Dr. Susan Richter is another important person who mentored me throughout my thesis. I would like to thank her for generously lending her time and expertise to train me in peptide radiochemistry and assist me with the peptide work done in this project. I am very grateful to Dr. Melinda Wuest for her immense contributions to this project, as she conducted all of the animal studies as well as provided guidance and advice as both lab colleague and supervisory committee member. I would also like to thank my other two supervisory committee members, Dr. Ing Swie Goping and Dr. Mary Hitt, for their guidance and expertise. I also gratefully acknowledge Monica Wang for training and assisting me with much of the biological work, Cody Bergman for all of his work synthesizing the numerous peptides investigated in this project, and Jenilee Way for

preparing the ^{18}F -containing prosthetic groups each day that I did ^{18}F radiochemistry. I would like to thank Dr. Christian Foerster, who was always willing to lend help and advice and who synthesized the ^{64}Cu -NOTA-annexin V used in the PS binding assays. Thank-you to Alison Marshall, who in addition to helping with the cell work, has been a lovely friend and officemate. I also thank the entire Wuest lab group for providing me with such a collaborative, helpful, team-based environment to work in. I have received plenty of advice and help from many different experts in this group, and for this I am very grateful.

I would like to thank the Imaging Facility and Flow Cytometry Lab in the Department of Experimental Oncology at the Cross Cancer Institute for helping me with the cell imaging and flow cytometry studies. I also gratefully acknowledge the Cyclotron Facility and Edmonton PET Centre at the Cross Cancer Institute for providing ^{18}F and ^{18}F -containing radiotracers, as well as the Washington University School of Medicine for providing ^{64}Cu .

Finally, I would like to express my extreme gratitude to my mother, who has always been a tremendous support for me. I would also like to thank the rest of my family and friends for their love and encouragement.

TABLE OF CONTENTS

1. Introduction	1
1.1. Molecular response of tumours to anticancer therapy	7
1.2. Agents for molecular imaging of cell death	14
1.3. Annexin V-based imaging of apoptosis	16
1.4. PS-binding peptides for imaging apoptosis	21
1.5. Hypothesis and objectives	24
2. Materials and Methods	26
2.1. General	26
2.2. Synthesis of peptides, labelling precursors and cold references	29
2.2.1. Synthesis of peptides and conjugates (general procedure)	29
2.2.2. Synthesis of PGDLSR	30
2.2.3. Synthesis of FBz-PGDLSR	30
2.2.4. Synthesis of CPGDLSR	31
2.2.5. Synthesis of LIKKPF	31
2.2.6. Synthesis of FBz-LIKKPF	31
2.2.7. Synthesis of CLIKKPF	32
2.2.8. Synthesis of PSBP-6	32
2.2.9. Synthesis of C-PSBP-6	32
2.2.10. Synthesis of FBz-PSBP-6	33
2.2.11. Synthesis of NOTA-Bn-thiourea-Ava-PSBP-6 (NOTA-PSBP-6)	33
2.2.12. Labelling NOTA-PSBP-6 with cold Ga ³⁺	33

2.2.13. Labelling NOTA-PSBP-6 with cold Cu ²⁺	34
2.2.14. Coupling of FBAM to CPGDLSR, CLIKKPF and C-PSBP-6 (general procedure)	35
2.2.15. Synthesis of FBAM-CPGDLSR	35
2.2.16. Synthesis of FBAM-CLIKKPF	35
2.2.17. Synthesis of FBAM-C-PSBP-6	36
2.2.18. Synthesis of FITC-Ava-PSBP-6 (FITC-PSBP-6)	36
2.3. Radiochemistry	37
2.3.1. Synthesis of ¹⁸ F-labelled prosthetic groups	37
2.3.1.1. Synthesis of [¹⁸ F]SFB	37
2.3.1.2. Synthesis of [¹⁸ F]FBEM	37
2.3.1.3. Synthesis of [¹⁸ F]FBAM	38
2.3.2. Radiolabelling wild-type annexin V with ¹⁸ F-containing prosthetic groups	38
2.3.2.1. Labelling wild-type annexin V with [¹⁸ F]SFB	38
2.3.2.2. Labelling wild-type annexin V with [¹⁸ F]FBEM	39
2.3.3. Synthesis of ⁶⁴ Cu-NOTA-annexin V	40
2.3.3.1. Synthesis of NOTA-annexin V	40
2.3.3.2. Labelling NOTA-annexin V with ⁶⁴ Cu	41
2.3.4. Radiolabelling PGDLSR with [¹⁸ F]SFB	42
2.3.5. Radiolabelling LIKKPF with [¹⁸ F]SFB	42
2.3.6. Radiolabelling PSBP-6 with [¹⁸ F]SFB	43
2.3.7. Radiolabelling C-PSBP-6 with [¹⁸ F]FBAM	45

2.3.8.	Radiolabelling NOTA-PSBP-6 with ⁶⁸ Ga	46
2.3.9.	Radiolabelling NOTA-PSBP-6 with ⁶⁴ Cu	47
2.4.	Competitive radiometric PS-binding assay	47
2.5.	Cell culture	49
2.6.	Inducing apoptosis in EL4 cells	49
2.7.	Cell binding assay	50
2.7.1.	Cell binding assay for ¹⁸ F-labelled annexin V	50
2.7.2.	Cell binding assay for radiopeptides	51
2.8.	Flow cytometry	52
2.8.1.	Flow cytometry using FITC-annexin V	52
2.8.2.	Flow cytometry using FITC-PSBP-6	53
2.9.	Fluorescence confocal microscopy	54
2.9.1.	Fluorescence confocal microscopy using FITC-annexin V	54
2.9.2.	Fluorescence confocal microscopy using FITC-PSBP-6	55
2.10.	EL4 lymphoma mouse tumour model	56
2.11.	Dynamic PET imaging	56
2.12.	Determination of radiopeptide lipophilicity	57
2.13.	Determination of blood distribution and metabolic stability in vivo	58
2.14.	Data analysis	59
3.	Results	60
3.1.	Labelling wild-type annexin V with ¹⁸ F for PET imaging of cell death	60
3.1.1.	Radiolabelling annexin V using random and site-selective approaches	60

3.1.2. <i>In vitro</i> evaluation of ^{18}F -labelled annexin V	62
3.1.2.1. Inducing apoptosis in EL4 cells using camptothecin	62
3.1.2.2. Cell binding assay using [^{18}F]SFB-annexin V and [^{18}F]FBEM-annexin V	63
3.1.3. Preclinical PET imaging of apoptosis using ^{18}F -labelled annexin V	67
3.2. Evaluation of PS-binding peptides for PET imaging of apoptosis	71
3.2.1. Competitive radiometric PS binding assay to determine binding potency	71
3.2.2. Labelling PS-binding peptides with ^{18}F	74
3.2.2.1. Labelling PGDLSR with ^{18}F	74
3.2.2.2. Labelling LIKKPF with ^{18}F	74
3.2.2.3. Labelling PSBP-6 with ^{18}F	75
3.2.3. Labelling PS-binding peptides with radiometals	76
3.2.3.1. Labelling PSBP-6 with ^{68}Ga	77
3.2.3.2. Labelling PSBP-6 with ^{64}Cu	78
3.2.4. Metabolic stability studies	79
3.2.5. Cell binding assay using ^{64}Cu -NOTA-PSBP-6	82
3.2.6. Preclinical PET imaging of apoptosis in EL4 tumour-bearing mice using ^{64}Cu -labelled PSBP-6	84
3.3. Evaluation of fluorescently-labelled PS-binding peptides for detection of apoptosis	87
3.3.1. Flow cytometry of EL4 cells using FITC-PSBP-6	87

3.3.2. Confocal fluorescence microscopy using FITC-PSBP-6	88
4. Discussion	90
4.1. Comparison of wild-type annexin V radiolabelled with fluorine-18 using random vs. site-selective approaches	90
4.2. Limitations and challenges of using annexin V for molecular imaging of apoptosis	94
4.3. PS-binding peptides as promising alternatives for molecular imaging of apoptosis	99
5. Conclusions and future directions	118
6. References	122

LIST OF FIGURES

Figure 1. Depiction of how a PET scan is carried out.	4
Figure 2. Fused PET/CT image using [^{18}F]FDG as radiotracer showing many metastases in a patient with melanoma.	5
Figure 3. Intrinsic and extrinsic pathways for initiation of apoptosis.	11
Figure 4. Biological features of cell death typically exploited for imaging cell death.	14
Figure 5. Crystal structure of annexin V.	16
Figure 6. Imaging cell death using annexin V (annexin A5).	18
Figure 7. Random and site-specific labelling of annexin V with [^{18}F]SFB and [^{18}F]FBEM.	60
Figure 8. Quality control of ^{18}F -labelled annexin V.	61
Figure 9. Flow cytometric analysis of EL4 cells undergoing camptothecin-induced apoptosis using FITC-annexin V as fluorescent stain.	62
Figure 10. Fluorescence confocal microscopy images of apoptotic EL4 cells stained with FITC-annexin V and PI.	63
Figure 11. EL4 cell binding of [^{18}F]SFB-annexin V.	64
Figure 12. Effect of Ca^{2+} concentration on control EL4 cell binding of [^{18}F]SFB-annexin V.	65
Figure 13. Effect of Ca^{2+} concentration on camptothecin-treated EL4 cell binding of [^{18}F]SFB-annexin V.	65
Figure 14. EL4 cell binding of [^{18}F]FBEM-annexin V.	66
Figure 15. Preclinical PET/CT images of EL4 tumour uptake of ^{18}F -labelled annexin V in a control (untreated) mouse.	68
Figure 16. TACs of the blood clearance profile and radioactivity profile in control (untreated) EL4 tumours in mice injected with ^{18}F -labelled annexin V.	68
Figure 17. Preclinical PET images of EL4 tumour response to treatment with cyclophosphamide and etoposide using ^{18}F -labelled annexin V as radiotracer.	69

Figure 18. Effect of treatment with cyclophosphamide and etoposide on EL4 tumour uptake of ^{18}F -labelled annexin V in C57Bl6 mice.	70
Figure 19. Inhibitory binding effect of unmodified and modified hexapeptides on PS binding of ^{64}Cu -NOTA-annexin V.	72
Figure 20. Inhibitory binding effect of unmodified, cysteine-tagged and fluorobenzylylated PSBP-6 on PS binding of ^{64}Cu -NOTA-annexin V.	73
Figure 21. Inhibitory binding effect of NOTA-conjugated PSBP-6 coordinated with cold Ga^{3+} or Cu^{2+} on PS binding of ^{64}Cu -NOTA-annexin V.	73
Figure 22. Synthesis of ^{18}F]FB-PGDLSR.	74
Figure 23. Synthesis of ^{18}F]FB-LIKKPF.	75
Figure 24. Synthesis of ^{18}F]FBAM-C-PSBP-6.	76
Figure 25. Radiolabelling NOTA-PSBP-6 with ^{68}Ga .	78
Figure 26. Radiolabelling NOTA-PSBP-6 with ^{64}Cu .	79
Figure 27. Stability of ^{68}Ga -NOTA-PSBP-6 in BALB/c mouse plasma over time.	80
Figure 28. Blood distribution of ^{68}Ga -NOTA-PSBP-6 over time.	81
Figure 29. Stability of ^{64}Cu -NOTA-PSBP-6 in BALB/c mouse plasma over time.	81
Figure 30. Blood distribution of ^{64}Cu -NOTA-PSBP-6 over time.	82
Figure 31. Binding of ^{64}Cu -NOTA-PSBP-6 to control and camptothecin-treated EL4 cells in the absence and presence of Ca^{2+} .	83
Figure 32. EL4 tumour and muscle uptake of ^{64}Cu -NOTA-PSBP-6 in C57Bl6 mice in response to treatment with cyclophosphamide and etoposide.	85
Figure 33. Representative preclinical PET images of EL4 tumour response to treatment with cyclophosphamide and etoposide using ^{64}Cu -NOTA-PSBP-6 as radiotracer, shown as MIPs.	86
Figure 34. Representative preclinical PET images of EL4 tumour response to treatment with cyclophosphamide and etoposide using ^{64}Cu -NOTA-PSBP-6 as radiotracer, shown as coronal, sagittal and transaxial tumour slices.	87
Figure 35. Flow cytometric analysis of EL4 cells undergoing camptothecin-induced apoptosis using FITC-PSBP-6 as fluorescent stain.	88

Figure 36. Fluorescence confocal microscopy images of EL4 cells stained with FITC-PSBP-6, NucView 405 Caspase-3 Substrate and PI to image camptothecin-induced cell death.	89
Figure 37. Structure of [¹⁸ F]FDG-MHO.	91
Figure 38. Structure of SAAC-PSBP-6 complexed with Re or ^{99m} Tc.	102

LIST OF ABBREVIATIONS

3D - three-dimensional

ABC transporter - ATP-binding cassette-transporter

Aoc - aminooctanoic acid

Ava - aminovaleric acid (aminopentanoic acid)

BBN - bombesin

BCA - bicinchoninic acid

Bn - benzyl

Boc - tert-butyloxycarbonyl

BSA - bovine serum albumin

c-FLIP - cellular FLICE (FADD-like IL-1 β -converting enzyme)-inhibitory protein

CT - x-ray computed tomography

^{64}Cu - copper-64

$[\text{}^{64}\text{Cu}]\text{Cu}(\text{OAc})_2$ - $[\text{}^{64}\text{Cu}]$ copper (II) acetate

$\text{Cu}(\text{OAc})_2$ - copper (II) acetate

Cys - cysteine

DCM - dichloromethane

DIPEA - N,N-diisopropylethylamine

DISC - death-inducing signaling complex

DMF - dimethylformamide

DMSO - dimethyl sulfoxide

DNA - deoxyribonucleic acid

DOTA - 1,4,7,10-tetraazacyclododecane-1,4,7,10-tetraacetic acid

DTPA - diethylenetriaminepentaacetic acid

DTT - dithiothreitol

EDT - 1,2-ethanedithiol

EDTA - ethylenediaminetetraacetic acid

ER - endoplasmic reticulum

ESI - electrospray ionization

^{18}F - fluorine-18

FADD - Fas-associated protein with death domain

FAM - 5-carboxyfluorescein

FasL - Fas ligand

FBAM - *N*-[6-(4-fluoro-benzylidene)aminoxyhexyl]maleimide

FBEM - *N*-[2-(4-fluorobenzamido)ethyl]maleimide

FBz - 4-fluorobenzoyl (4-fluorobenzoic acid)

FBS - fetal bovine serum

^{18}F FDG - ^{18}F fluorodeoxyglucose

^{18}F FDG-MHO - ^{18}F fluorodeoxyglucose-maleimidehexyloxime

^{18}F FBAM - *N*-[6-(4- ^{18}F fluoro-benzylidene)aminoxyhexyl]maleimide

^{18}F FBEM - *N*-[2-(4- ^{18}F fluorobenzamido)ethyl]maleimide

FITC - fluorescein isothiocyanate

Fmoc - fluorenylmethyloxycarbonyl

^{18}F SFB - *N*-succinimidyl-4- ^{18}F fluorobenzoate

^{68}Ga - gallium-68

GPCR - G-protein coupled receptor

HBTU - O-benzotriazole-N,N,N',N'-tetramethyl-uronium-hexafluoro-phosphate

HEPES - 4-(2-hydroxyethyl)-1-piperazineethanesulfonic acid

HPLC - high performance liquid chromatography

HYNIC - hydrazinonicotinic acid

¹¹¹I - indium-111

¹²³I - iodine-123

¹²⁴I - iodine-124

¹²⁵I - iodine-125

IAPs - inhibitors of apoptosis proteins

IC₅₀ - half maximal inhibitory concentration

ICMT-11 - (S)-1-((1-(2-fluoroethyl)-1H-[1,2,3]-triazol-4-yl)methyl)-5-(2(2,4-difluorophenoxy)methyl)-pyrrolidine-1-sulfonyl)isatin

%ID/g - percent of injected dose per gram

K_d - dissociation constant

LR-MS - low resolution mass spectrometry

¹⁷⁷Lu - lutetium-177

mAb - monoclonal antibody

MALDI - matrix-assisted laser desorption ionization

MALDI-TOF - matrix-assisted laser desorption ionization-time of flight

MAP - maximum a posteriori

MBHA - 4-methylbenzhydramine

MIP - maximum intensity projection

ML-10 - 2-(5-fluoro-pentyl)-2-methyl-malonic acid

MOMP - mitochondrial outer membrane permeablization

MRI - magnetic resonance imaging

MW - molecular weight

m/z - mass-to-charge ratio

NaOAc - sodium acetate

NH₄OAc - ammonium acetate

NHS - *N*-hydroxysuccinimide

NOTA - 1,4,7-triazacyclononane-triacetic acid

NSCLC - non-small cell lung cancer

Oxyma - ethyl-2-cyano-2-(hydroxyimino) acetate

Pbf - 2,2,4,6,7-pentamethyldihydrobenzofuran-5-sulfonyl

PBS - phosphate-buffered saline

PEG - polyethylene glycol

PET - positron emission tomography

P.i. - post-injection

PI - propidium iodide

PC - phosphatidylcholine

PE - phosphatidylethanolamine

PS - phosphatidylserine

PSBP-6 - PS-binding peptide 6 (sequence FNFRLKAGAKIRFG)

r² - coefficient of determination

Radio-TLC - radio-thin-layer chromatography

R_f- retention factor

RBC - red blood cell

RCP - radiochemical purity

RCY - radiochemical yield

ROI - region(s) of interest

SAAC - single amino acid chelate

SCN - thiocyanate

SDS - sodium dodecyl sulfate

SDS-PAGE - sodium dodecyl sulfate polyacrylamide gel electrophoresis

SEC - size-exclusion chromatography

SEM - standard error of the mean

SPECT - single photon emission computed tomography

SPPS - solid-phase peptide synthesis

SPR - surface-plasmon resonance

SFB - *N*-succinimidyl-4-fluorobenzoate

SUV - standardized uptake value

$t_{1/2}$ - half-life

TAC - time-activity curve

^{99m}Tc - technetium-99m

TFA - trifluoroacetic acid

TLC - thin-layer chromatography

$\text{TNF}\alpha$ - tumour necrosis factor α

t_R - retention time

TRAIL - tumor necrosis factor-related apoptosis-inducing ligand

Trt - triphenylmethyl

TUNEL - terminal deoxynucleotidyl transferase-mediated deoxyuridine triphosphate

nick-end labelling

USPIO - ultrasmall superparamagnetic iron oxide

UV - ultraviolet

xg - times gravity

v/v - volume/volume

^{90}Y - yttrium-90

Zn^{2+} -DPA - zinc(II)-dipicolylamine

^{89}Zr - zirconium-89

STANDARD AMINO ACID ABBREVIATIONS

Ala (A) - Alanine

Arg (R) - Arginine

Asn (N) - Asparagine

Asp (D) - Aspartic acid

Cys (C) - Cysteine

Gln (Q) - Glutamine

Glu (E) - Glutamic acid

Gly (G) - Glycine

Leu (L) - Leucine

Lys (K) - Lysine

Phe (F) - Phenylalanine

Pro (P) - Proline

Tyr (Y) - Tyrosine

Val (V) - Valine

1. INTRODUCTION

Cancer patients can be treated by surgery, radiation therapy, chemotherapy, or any combination of these methods. Monitoring patient response to therapy is very important, as patients with the same type of cancer frequently respond differently when given the same treatment¹. Tumour heterogeneity between patients of the same cancer type leads to differences in sensitivity of each patient to therapy, particularly targeted drug therapy. Since each tumour displays a different genotype and set of biomarkers, they will each respond differently to specific targeted drugs, and this has led to the need for personalized medicine². Tumour cells can also develop drug resistance by acquiring adaptive mutations, leading to proliferation and progression of a new subpopulation of tumour cells that are unresponsive to a treatment that had previously been effective³. Furthermore, interpatient differences in drug metabolism rates (cytochrome p450 activity), ABC transporter expression, diet, interactions with other drugs, and other environmental factors can cause differences in patient response to therapy, including the dose required to have an effect⁴. Since cytotoxic drugs often have steep dose-response relationships and narrow therapeutic windows, each patient must be monitored to ensure they are given an appropriate dose to have a therapeutic effect without too much toxicity. For these reasons, tumour response to therapy must be monitored in order to ensure that the patient is receiving effective treatment.

The current gold standard for monitoring response to radiation therapy and chemotherapy in cancer patients is the use of anatomical imaging techniques such as X-ray computed tomography (CT) and magnetic resonance imaging (MRI) to observe

changes in the size and morphology of tumours⁵. However, these methods have several limitations. Some tumours are not visible, such as micrometastases, and mass lesions of unknown activity often persist, even when therapy has effectively inactivated the cancer⁶. Changes in tumour size do not always reflect clinical condition, as patients can show clinical signs of disease progression without an increase in tumour size⁷. Tumour measurement reproducibility is poor due to observer variations in determining lesion boundary position, particularly with irregular or infiltrating lesions⁸. In addition, it often takes 6-12 weeks for therapy to produce any anatomical changes in a tumour⁹, and these changes have been shown to lag behind the physiological and metabolic response of the tumour^{10,11}. If the treatment is ineffective, this results in unnecessary expense, and patients must endure increased toxic side effects. Delaying the initiation of a better, more effective therapy can also result in tumour progression and increased morbidity⁵. In addition, new tumour growth may have occurred during those 6-12 weeks, even if therapy invoked a response, which would result in a false negative when it could have been a matter of just adjusting the dose. Heterogeneity within and between tumours and their microenvironments complicates assessment of therapy response, as a treatment may have been effective at killing only a subpopulation of tumour cells or specific region of the tumour, while the rest of the tumour is still active¹². Clearly, anatomical changes in a tumour should not be used as the only measure of therapy response. Changes at the molecular level must be monitored in order to detect microscopic events in tumour cells and their microenvironments, allowing for earlier assessment of therapy response and better understanding of the molecular response induced by therapy.

Although *in vitro* and *ex vivo* techniques can be used to examine molecular processes in tumour tissue extracted by biopsy or surgery, these procedures are invasive and time consuming, and do not provide information on the “whole picture”. Intratumour heterogeneity often results in sampling bias³, and it is difficult to do follow-up studies with these microscopic techniques, making them more appropriate for diagnosis rather than assessment of therapeutic response¹³. As a result, increasing attention is being focused on using non-invasive, *in vivo* functional imaging techniques such as single photon emission computed tomography (SPECT) and positron emission tomography (PET) to assess patient response to therapy. These nuclear imaging methods use radioactive probes (radiotracers) that bind to specific molecular targets in the body to visualize biological processes at the molecular level, including the presence of biomarkers. In order to develop a nuclear imaging probe, an appropriate target specific to the molecular process of interest must first be identified. A ligand that selectively binds to that target with high affinity, which may be a pre-existing biomolecule or can be rationally designed, must then be labelled with a radioactive isotope. For PET imaging, which is the most sensitive molecular imaging technique that produces the highest resolution images, the radioactive isotope used must be a positron emitter, such as iodine-124 (¹²⁴I), gallium-68 (⁶⁸Ga), copper-64 (⁶⁴Cu), or, most commonly, fluorine-18 (¹⁸F). Once injected into the patient’s body at a subpharmacological dose (tracer dose), the radiotracer localizes at the target, where the radioisotope emits a positron, which annihilates with an electron in the tissue to produce two gamma ray photons travelling in opposite directions¹⁴. The photons are measured by a ring of detectors surrounding the patient, and computer software uses these measurements to construct a three-dimensional

(3D) image of the location and concentration of the radiotracer. This process is depicted in figure 1. A radiolabelled probe should localize at the intended site at high concentrations, while exhibiting good blood clearance and contributing little to background signal, so as to produce a high target-to-background ratio¹⁵.

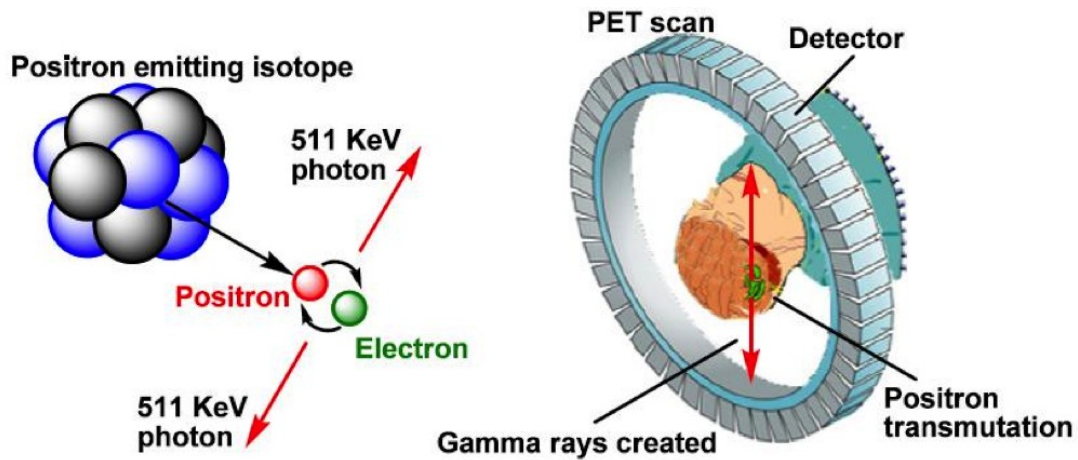


Figure 1. Depiction of how a PET scan is carried out. Adapted from Li and Conti¹⁶.

Many processes can be targeted in oncologic nuclear imaging. The most well-known PET imaging agent is [¹⁸F]fluorodeoxyglucose ([¹⁸F]FDG), a radiolabelled analogue of glucose that is taken up into cells via glucose transporters to be metabolized. Thus, cell uptake of [¹⁸F]FDG is a measure of glucose metabolism, and since tumour cells have much higher glucose metabolism rates than normal tissues, [¹⁸F]FDG accumulates in tumours¹⁴. This method is excellent for diagnosis of cancer, particularly metastases that cannot be detected by anatomical imaging methods (figure 2).

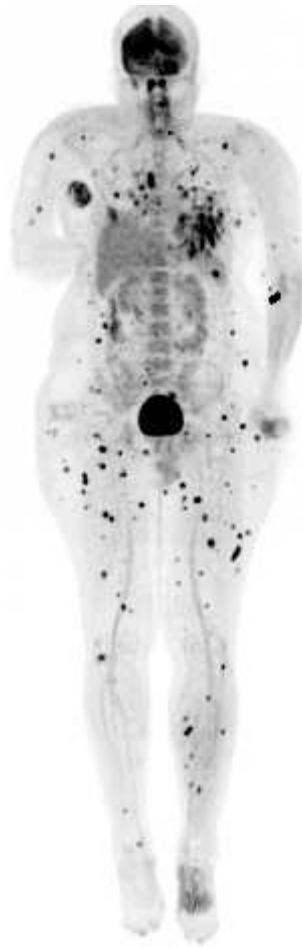


Figure 2. Fused PET/CT image using [^{18}F]FDG as radiotracer showing many metastases in a patient with melanoma¹⁷.

It can also be used to assess the metabolic response of a tumour to therapy, and studies have demonstrated that changes in tumour uptake of [^{18}F]FDG are a better predictor of survival than changes in tumour morphology and density^{14,18}. However, some cancers such as neuroendocrine, thyroid, testicular, renal, hepatocellular and bladder cancers have low or variable [^{18}F]FDG uptake, limiting the use of this radiotracer for measuring metabolic changes in these types of tumours¹⁸. Also, results for studies observing the utility of [^{18}F]FDG–PET in predicting patient response to therapy are conflicting¹⁹. A decrease in [^{18}F]FDG uptake does not necessarily mean that a tumour is

regressing, as many tumours can acquire mutations that allow them to utilize other energy sources, such as fructose²⁰. Furthermore, a “flare” effect is often seen with [¹⁸F]FDG–PET, whereby a transient increase in [¹⁸F]FDG occurs in the tumour soon after treatment, subsequently followed by tumour regression and a decrease in [¹⁸F]FDG uptake. This can be due to a number of factors, including recruitment of inflammatory cells with high glucose metabolism to the tumour site, or induction of apoptosis in the tumour cells, which is an energy-dependent process²¹. In order to avoid false negatives due to the flare effect, guidelines for using [¹⁸F]FDG –PET to assess tumour response to therapy indicate that patients should wait between 2-12 weeks after therapy before getting a [¹⁸F]FDG–PET scan, depending on the cancer type²². This does not allow for early, efficient assessment of tumour response. Apart from glucose metabolism, there are other tumour-specific processes that can be targeted for PET monitoring of tumours, including cell proliferation, cell membrane metabolism, angiogenesis, tumour cell hypoxia, antigen/receptor expression, amino acid transport, and synthesis of DNA, proteins, and lipids^{14,18,23,24}. Like with [¹⁸F]FDG–PET, observing changes in these processes only provides an indirect measurement of tumour response to therapy, and are not optimal for this purpose due to flare effects and adaptive mutations. The most direct and accurate way to assess tumour response to therapy would be to image cell death, for which there is currently no widely-used, clinically accepted method. Since tumour regression results from a combination of tumour cell death and decreased cancer growth, cell death monitoring would reveal the effect of cell death alone on tumour response. Molecular imaging of cell death would also capture regional tumour heterogeneity by showing areas of the tumour that are drug resistant. Since the molecular mechanisms underlying cell

death have been shown to precede changes in tumour size and morphology^{25,26}, molecular imaging of cell death would allow for early assessment of treatment efficacy. Moreover, the ability to visualize cell death kinetics would lead to improved dosing. These advantages have important implications for patient care, as physicians would be able to adjust and optimize individual treatment regimens more efficiently. In addition, imaging cell death would be extremely valuable for drug development, at both the preclinical and clinical level. Animal models of cancer can be used to test the efficacy of novel treatments, and the ability to image cell death in these models using preclinical PET would allow researchers to better understand the molecular response induced by a drug²⁷. PET imaging of cell death would also provide an earlier, more accurate indication of therapy response in clinical trials. The ability to screen novel drug efficacy more efficiently would speed up the process of drug development and reduce unnecessary expenses²⁸.

In addition to its importance in oncology, imaging cell death would also be very useful in monitoring a variety of pathological conditions associated with aberrant cell death. For example, neurodegenerative diseases such as Parkinson's, Alzheimer's and Huntington's disease, autoimmune disorders such as rheumatoid arthritis, as well as cardiovascular disease are all associated with excessive, uncontrolled death of healthy cells²⁹.

1.1. Molecular response of tumours to anticancer therapy

Effectiveness of an anticancer therapy depends on its ability to permanently inactivate tumour cells. This can occur through either cellular senescence, whereby the

cell undergoes permanent cell cycle arrest, or through some form of cell death³⁰. Cellular senescence, which manifests in a flattened and granular phenotype as well as expression of the senescence-associated β -galactosidase enzyme, can initially help to limit tumour progression. However, the continued presence of senescent cells can actually contribute to tumour progression by secreting inflammatory and tumour-promoting factors into the microenvironment, which induces proliferation and tumourigenesis in surrounding cells³¹. Thus, the desired effect of anticancer therapy is tumour cell death. There are various pathways by which cells can die, although these pathways are not mutually exclusive and can often overlap. Many dying cells exhibit biochemical or morphological features from more than one pathway, and a cell that is undergoing one type of cell death can later switch to another mode^{32,33}. Necrosis is an uncontrolled form of cell death induced by excessive, traumatic cell damage, and is characterized by cell swelling, organelle degradation, and plasma membrane rupture followed by a release of intracellular components into the surrounding environment, including cytokines and other pro-inflammatory factors. This often results in a local inflammatory response in the surrounding tissue, which can have a tumour-promoting effect, since immune inflammatory cells have been shown to induce cell proliferation, angiogenesis and tumour cell invasiveness³⁴. Programmed necrosis, or “necroptosis”, which occurs in a controlled, regulated manner but still exhibits the morphological features of necrosis, can also occur³⁵. Autophagy is a controlled protein degradation system that is activated when a cell is not getting enough nutrients, and can facilitate either cell survival or cell death, depending on the extent of cell starvation. This dual role has complex implications in tumour response to therapy, as autophagy can either contribute to tumour cell death or to

therapy resistance³⁶. Autophagic cell death manifests in formation of autophagic vacuoles and double-membraned autophagosomes, an increase in lysosomal activity, partial chromatin condensation and membrane blebbing. Mitotic catastrophe, another mode of cell death, has gained recognition in more recent years. It is induced by deficient cell-cycle checkpoints and cell damage leading to aberrant mitosis, and is associated with the formation of giant, multinucleate cells³⁷. Although any combination of these cell death pathways may be induced in cancer cells by anticancer therapies, the most understood and well-characterized mode of cell death and perhaps the most desired effect of anticancer therapy is apoptosis.

Apoptosis is a natural, tightly regulated process of programmed cell death that has an important role in normal physiological processes such as embryonic development, immune system regulation, and tissue homeostasis³⁸. Apoptosis can be initiated by an intrinsic pathway or an extrinsic pathway (figure 3). The intrinsic pathway is triggered by intracellular stressors such as endoplasmic reticulum (ER) stress, oxidative damage, ischemia, and DNA damage, and is initiated when cytochrome c is released into the cytosol through channels on the mitochondrial membrane. Mitochondrial outer membrane permeabilization (MOMP) and subsequent release of cytochrome c is regulated by the bcl-2 family of proteins. Anti-apoptotic bcl-2 proteins (bcl-2 and bcl-xl) function to keep mitochondrial membrane channels closed, while pro-apoptotic bcl-2 proteins such as bax and bak function to open the channels to release cytochrome c and initiate apoptosis. Other regulators of apoptosis initiation include inhibitor of apoptosis proteins (IAPs), which contribute to anti-apoptotic signaling, while other proteins such as DIABLO, which inhibits IAPs, promote apoptosis. When pro-apoptotic signals

overwhelm the anti-apoptotic signals, cytochrome c is released and forms a complex with the Apaf-1 protein, which is called the apoptosome. The apoptosome cleaves initiator caspase-9 (a cysteine aspartic acid-specific protease), initiating a signaling cascade of protease cleavages that results in the activation of executioner caspases -3, -6 and -7. These executioner caspases induce cell death by cleaving many different death substrates, whose cleavage causes critical cellular components to be destroyed³⁹.

Alternatively, the extrinsic pathway functions through the activation of death receptors on the cell surface. Upon binding of death ligands such as tumour necrosis factor α (TNF α) or Fas ligand (FasL), the death receptors form a death-inducing signaling complex (DISC) with adaptor protein FADD and initiator procaspases -8 and -10 on the cytosolic domain of the receptor. DISC then induces cleavage/activation of caspases -8 and -10, which directly cleave and activate the executioner caspases. This is where the extrinsic and intrinsic pathways converge: the execution phase. Caspases -8 and -10 might also cleave and activate the proapoptotic protein Bid, which induces cytochrome c release from the mitochondria. This demonstrates the cross-talk that occurs between the extrinsic and intrinsic pathways⁴⁰. Anti-apoptotic protein c-FLIP contributes to regulatory signaling of the extrinsic pathway by inhibiting FADD and/or caspases -8/-10. Apoptosis can also be induced by Granzyme B released from immune cells, which activates caspase-3 and contributes to mitochondrial disruption and pro-apoptotic signaling⁴¹.

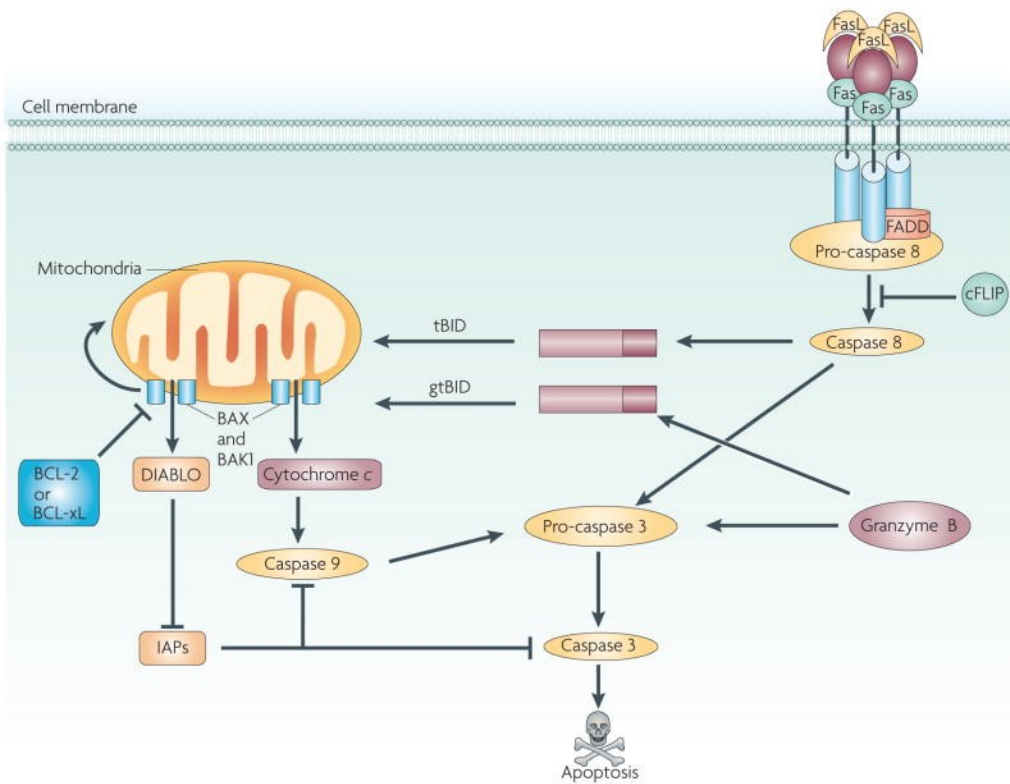


Figure 3. Intrinsic and extrinsic pathways for initiation of apoptosis⁴².

The execution phase of apoptosis is characterized by a series of biochemical and morphological changes to the cell. In addition to caspase activation, MOMP coordinates mitochondrial membrane depolarization and plasma membrane depolarization⁴³. Morphological changes include chromatin condensation, cell shrinkage, and controlled breakdown of cellular protein and DNA. This is followed by membrane blebbing and fragmentation of the cell into smaller, membrane-enclosed “apoptotic bodies” which are then consumed by phagocytes⁴⁴. Another defining characteristic of a cell entering the execution phase is the redistribution and externalization of the phospholipid PS to the outer leaflet of the plasma membrane, which is always a feature of apoptosis, regardless of initiating stimulus⁴⁵. “Flippase”, an ATP-dependent translocase enzyme, pumps aminophospholipids, including PS and phosphatidylethanolamine (PE), from the outer

leaflet of the plasma membrane to the inner leaflet, while another translocase protein, “floppase”, actively pumps cholinephospholipids, including phosphatidylcholine (PC) and sphingomyelin, to the outer leaflet⁴⁶. These two enzymes function to maintain this plasma membrane asymmetry between the inner and outer leaflets of a healthy cell. When apoptosis is initiated, flippase and floppase are deactivated; however, the inactivity of these translocases is not enough to induce rapid externalization of PS to the outer leaflet⁴⁷. Phospholipid scramblases, which are activated by the increase in calcium ion (Ca^{2+}) levels upon induction of apoptosis, are responsible for the rapid redistribution of PS. These scramblases are passive, non-selective, bidirectional translocases that allow phospholipids to randomly distribute between the inner and outer leaflets⁴⁸. This leads to a collapse in membrane asymmetry and exposure of anionic phospholipids on the outer membrane, occurring in a matter of minutes⁴⁶. PS is the dominant anionic phospholipid present in the cell membrane, comprising 2-10% of the membrane phospholipids⁴⁹. Membrane phospholipid redistribution in apoptotic cells results in exposure of 50-200 million PS molecules⁵⁰. Phagocytes recognize the externalized PS and ingest the apoptotic bodies in an organized manner that does not involve an inflammatory response⁵¹. PS exposure precedes most of the other biochemical and morphological changes that occur in the apoptosis cascade, making it a marker of early to late stage apoptosis, before engulfment by phagocytes⁵². In addition to apoptotic cells, PS also becomes gradually exposed on circulating erythrocytes as they age, which are then cleared by phagocytes at the end of their life cycle⁵³. Activated platelets expose PS at their surface as well, helping to catalyze reactions at the cell surface to facilitate blood coagulation⁵⁴. PS is also exposed on macrophages that are activated to engulf dying cells,

which seems to play a role in their ability to phagocytose⁵⁵. Although PS exposure is most associated with apoptosis, it can also occur in other cell death pathways including autophagy and mitotic catastrophe⁵⁶.

The ability to image cell death *in vivo* using radiopharmaceutical-based nuclear medicine techniques would provide important information on treatment efficacy in cancer patients. This requires the development of a radiolabelled probe that can selectively bind to a molecular target specific to cell death. However, there is no known biomarker common to all cell death pathways outlined above that is not also common to other biological processes⁵⁷. As mentioned before, there are several different cell death mechanisms that can be induced by an anticancer treatment, some more desirable than others (namely apoptosis). If various probes were developed to target biomarkers specific to each type of cell death, this would allow oncologists to observe exactly which cell death mechanisms are being induced by a treatment, if at all. With this information, medical researchers and professionals can determine which anticancer treatments are inducing a desired response, and which treatments should be adjusted or abandoned. Thus far, research efforts to develop a probe for molecular imaging of cell death have mainly focused on targeting the molecular markers of apoptosis, which are most abundant and rationally targetable. The most common cellular events that have been used as targets for imaging cell death are outlined in Figure 4.

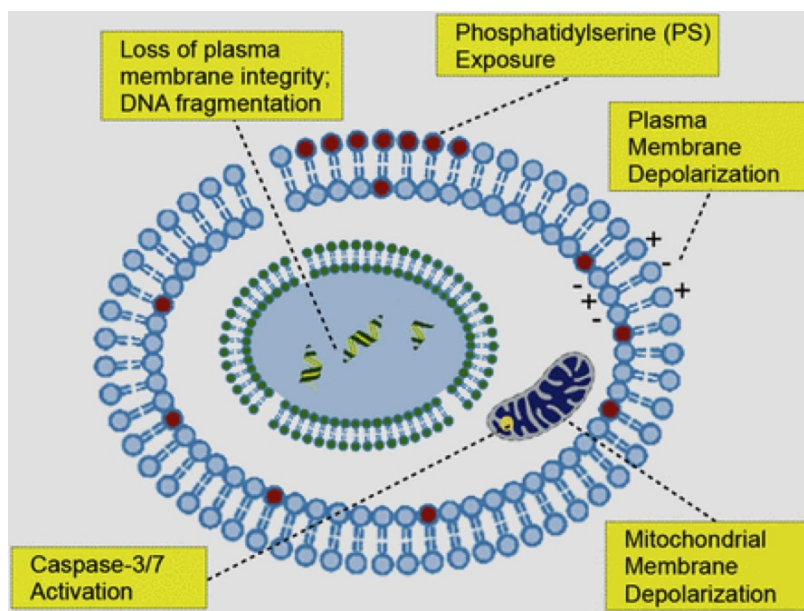


Figure 4. Biological features of cell death typically exploited for imaging cell death⁵⁸.

1.2. Agents for molecular imaging of cell death

Caspases are an attractive target for the development of an apoptosis-detecting probe due to their central role in the execution of apoptosis. The isatin sulphonamides are a family of indole derivatives that exhibit high-potency inhibition of executioner caspases-3 and -7⁵⁹. One isatin sulphonamide, (S)-1-((1-(2-fluoroethyl)-1H-[1,2,3]-triazol-4-yl)methyl)-5-(2(2,4-difluorophenoxy)methyl)-pyrrolidine-1-sulfonyl)isatin (ICMT-11), has been labelled with ¹⁸F for PET imaging of apoptosis, and its utility in detecting therapy-induced apoptosis in tumours has been demonstrated in several preclinical models⁶⁰⁻⁶². ¹⁸F-ICMT-11 has also shown promise as a PET imaging agent for neoadjuvant chemotherapy-induced apoptosis in breast tumours in a recent clinical study⁶³.

Mitochondrial membrane depolarization is another feature of cell death that has been targeted for molecular imaging. Arylphosphonium salts are membrane-permeable

lipophilic cations that accumulate at the negatively-charged inner membrane of intact mitochondria⁵⁸. Upon induction of apoptosis, the loss of mitochondrial membrane potential leads to a detectable loss of phosphonium cations from the mitochondria. ¹⁸F-fluorobenzyl triphenylphosphonium is an arylphosphonium salt developed for PET imaging of cell death, and was able to detect response of preclinical orthotopic prostate tumours to treatment with docetaxel⁶⁴.

Less well-known characteristics of cell death have also been identified and targeted for molecular imaging of tumour response to therapy. For example, one group identified a specific monoclonal antibody (mAb), APOMAB, which binds to the La/SSB antigen that becomes accessible in dying malignant cells when cell membrane integrity is lost⁶⁵. This antibody was able to detect tumour response to chemotherapy in a number of preclinical models⁶⁶⁻⁶⁸. Another group evaluated Apopep-1, a peptide that binds to histone H1 exposed on apoptotic and necrotic cells^{69,70}, in preclinical studies that demonstrated its ability to predict response of stomach tumours to combination treatment with cisplatin and cituximab⁷¹.

Small molecules from the ApoSense family have been shown to bind to apoptotic and necrotic cells via a mechanism that is not fully understood. These small molecules bind to and are transported across membranes of dying cells where they accumulate in the cytoplasm, while being excluded from healthy cells^{72,73}. The most successful of these molecules is ¹⁸F-labelled 2-(5-fluoro-pentyl)-2-methyl-malonic acid (¹⁸F-ML-10), which was shown to be effective at imaging apoptosis in preclinical models of therapy-induced tumour apoptosis^{73,74}, and has progressed to clinical trials for evaluation of therapy response in patients⁷⁵⁻⁷⁹.

Due to its accessibility, PS is an extremely attractive target for the development of a molecular imaging agent that can detect cell death. Many PS-targeting agents have been investigated for this purpose. Proteins that bind to PS include annexin V, annexin B1, the C2A domain of synaptotagmin I, and the C2 domain of lactadherin^{46,80}. The PS-targeting antibody fragment PGN635 F(ab')₂ binds to complexes of PS and β 2-glycoprotein I, and has been radiolabelled with ¹²⁴I for PET imaging of cell death in mouse prostate tumours induced by radiotherapy or docetaxel chemotherapy²⁵. PGN635 has also been labelled with positron emitter zirconium-89 (⁸⁹Zr) and was able to detect apoptosis in mice with KPL4 human breast tumours treated with paclitaxel, as well as in mice with COLO205 human colorectal tumours treated with PRO598⁸¹. Zinc(II)-dipicolylamine (Zn²⁺-DPA) complexes have also been found to bind to PS exposed on dying cells⁸². Zn²⁺-DPA has been labelled with ¹⁸F for PET imaging of apoptosis, and was able to detect cell death in a mouse model of Hepa1-6 hepatocellular carcinoma apoptosis induced by treatment with adriamycin⁸³.

1.3 Annexin V-based imaging of apoptosis

The most commonly known PS-targeting agent is annexin V, an endogenous, 36 kDa, intracellular protein that tightly binds to PS with nanomolar affinity^{84,85} in the presence of ionized calcium⁸⁶. The crystal structure of annexin V is shown in figure 5.



Figure 5. Crystal structure of annexin V⁸⁷.

The annexins are a superfamily of over 160 proteins that all exhibit Ca^{2+} -dependent binding to anionic phospholipids. They each contain a highly conserved COOH-terminal protein core that contains the Ca^{2+} and membrane binding sites⁸⁸. Annexin V is a member of this superfamily, and is expressed in many eukaryotic organisms, including humans. This protein is mainly present in the cell cytosol, but can also be found in low concentrations in the blood plasma⁸⁹. Bazzi and Nelsestuen determined that the amount of annexin V bound to PS was almost entirely determined by the calcium concentration⁹⁰. Increasing the calcium concentration produces an increase in saturation levels of bound annexin V, and binding of annexin V to PS-expressing membranes is negatively cooperative with respect to protein concentration⁹⁰. The high-affinity binding of annexin V to PS in the presence of Ca^{2+} makes this protein a sensitive probe for detecting dying cells (figure 6). While it is most associated with the detection of apoptosis, it also detects other modes of cell death because PS is often expressed in cells undergoing autophagy and mitotic catastrophe, and any loss of cell membrane integrity (i.e., necrosis) allows annexin V to reach PS confined to the inner leaflet of the membrane^{56,89}.

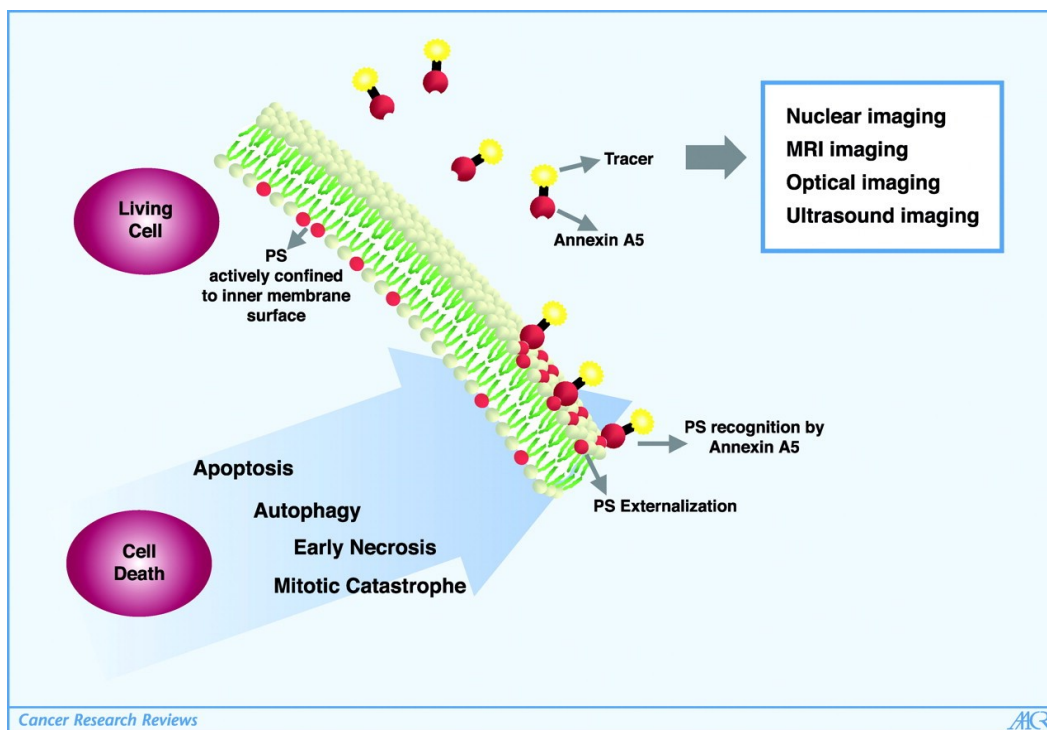


Figure 6. Imaging cell death using annexin V (annexin A5)⁹¹. Tracer can be radioactive or fluorescent.

Flourescently-labelled annexin V is used as a standard staining technique to determine apoptosis levels *in vitro* via flow cytometry and confocal microscopy⁹². Since annexin V was proven to be an effective apoptosis-detecting agent *in vitro*, efforts to develop this protein as a probe for molecular imaging of apoptosis *in vivo* have been extensive. Thus, a large amount of research has focused on the development of a clinically suitable form of radiolabelled annexin V. Annexin V and annexin V mutants, which were created for easier conjugation, have been labelled with technetium-99m (^{99m}Tc), iodine-123 (¹²³I), iodine-125 (¹²⁵I), and indium-111 (¹¹¹In) for SPECT imaging of apoptosis⁹³. The most successful and extensively studied annexin V-based molecular imaging probe for apoptosis detection is annexin V conjugated with hydrazinonicotinic acid (HYNIC) complexed with ^{99m}Tc (^{99m}Tc -HYNIC-annexin V), which was first published by Blankenberg and colleagues⁹⁴. Use of ^{99m}Tc-HYNIC-annexin V as an

apoptosis-detecting probe for assessment of tumour response to therapy has been demonstrated in a wide array of preclinical⁹⁴⁻¹⁰³ and clinical studies^{26,104-115}. However, ^{99m}Tc-HYNIC-annexin V shows high non-specific uptake in the kidney, liver and spleen, resulting in a poor tumour-to-background ratio and limiting imaging of tumours around these areas. SPECT is also less sensitive than PET and produces lower resolution images, so radiolabelling annexin V with a positron-emitting radionuclide for PET imaging of apoptosis would produce better quality images and allow for more sensitive imaging. Positron-emitting radionuclides that annexin V has been labelled with thus far include ¹²⁴I, ⁶⁴Cu, ¹⁸F and ⁶⁸Ga. ¹²⁴I-labelled annexin V is subject to radiodeiodination in vivo, and failed to detect therapy-induced apoptosis in preclinical tumour models¹¹⁶⁻¹¹⁸. ⁶⁴Cu-labelled annexin V showed promise as an apoptosis-detecting PET agent in a preclinical tumour model of breast cancer treated with photodynamic therapy, but the labelling chemistry and targeting protocols were complex. A ⁶⁸Ga-labelled annexin V mutant successfully detected apoptosis in a model of anti-Fas-induced liver apoptosis, but showed less promise when used to assess therapy response in a tumour model, as well as high non-specific uptake in the kidney and liver¹¹⁹. Of the PET tracers, ¹⁸F-labelled annexin V has received the most attention due to the favourable properties of ¹⁸F for PET imaging. This radioisotope has an optimal half life for diagnostic imaging ($t_{1/2} = 109.8$ min), high positron emission (97%), a low positron energy of 0.64 MeV resulting in high resolution images and low radiation dose, and it can be produced in large amounts with high specific activity by a cyclotron¹²⁰. Since direct labelling with ionized ¹⁸F ($[^{18}\text{F}]\text{F}^-$) requires use of harsh reaction conditions that are not compatible with biomolecules like proteins and peptides, labelling these biomolecules with ¹⁸F typically requires use of a

prosthetic group¹²¹. Radiolabelling wild-type annexin V with ¹⁸F is most commonly accomplished via a random labelling approach involving the *N*-hydroxysuccinimide (NHS)-containing prosthetic group *N*-succinimidyl-4-[¹⁸F]fluorobenzoate ([¹⁸F]SFB¹²²), which can react with any of the 22 lysine residues and N-terminus present in wild-type annexin V^{123,124}. This labelling approach has been carried out by several groups^{9,123–129}, and the ability of [¹⁸F]SFB-labelled wild-type annexin V to image apoptosis in vivo has been demonstrated in preclinical models of myocardial ischemia^{126,129}, cyclohexamide-induced liver apoptosis^{123,127}, and ketamine induced neuronal apoptosis¹²⁹. However, only one group has demonstrated the utility of [¹⁸F]SFB-labelled wild-type annexin V in imaging a tumour model of therapy-induced apoptosis, in which mice with human head and neck squamous cell cancer UM-SCC-22B tumour xenografts were treated with doxorubicin¹²⁷. Tait and colleagues suggested that since the prosthetic group [¹⁸F]SFB can conjugate to any of the 23 primary amine groups (-NH₂) present on annexin V, this non-specific, amine-directed conjugation of annexin V not only results in a poorly characterized radiotracer, but also might disrupt crucial binding interactions¹³⁰. In addition, if annexin V is conjugated with [¹⁸F]SFB at multiple sites, this could lead to disproportional signalling in PET imaging¹³¹. These concerns lead to the production of annexin V mutants, or “second generation annexin V”, which contain an additional short amino acid sequence on the N-terminus that contains a cysteine residue for easy, chemoselective labelling by thiol (-SH)-reactive prosthetic groups⁸⁹. Site-specific labelling of annexin V mutants with ¹⁸F has been carried out using different maleimide-based prosthetic groups^{131,132}. However, availability of cysteine-containing second generation annexin V is limited.

On the other hand, commercially available wild-type annexin V also contains a single chemically-accessible cysteine residue at position 315. No loss of binding affinity was observed for annexin V when Cys315 was deleted or replaced with thiol-free amino acids^{133,134}. Thus, Cys315 does not appear to be required for functionality of annexin V, as modification of this residue does not alter its biological activity. Maleimide-containing prosthetic groups, which react with free thiol groups, can be used to target this single cysteine residue and thus offer a controlled, site selective approach. However, to the best of our knowledge, there is only one report successfully exploiting this approach for radiolabelling wild-type annexin V¹³⁵. Glucose-based maleimide prosthetic group [¹⁸F]FDG-maleimidehexyloxime ([¹⁸F]FDG-MHO) was shown to be suitable for bioconjugation of wild-type annexin V at Cys315¹³⁵. However, it is unknown whether wild-type annexin V that has been site-selectively labelled at Cys315 with [¹⁸F]FDG-MHO retains its PS binding function, as it has not yet been evaluated *in vitro* or *in vivo*.

1.4. PS-binding peptides for imaging apoptosis

When developing a biomolecule for molecular imaging, small peptides offer some advantages over larger proteins and antibodies. Due to their small size, peptides can efficiently penetrate tissues and are rapidly cleared from the blood, allowing for good tumour-to-background contrast. They have low immunogenicity and their production is simple and inexpensive¹³⁶. Furthermore, procedures for chemical modification and radiolabelling of peptides are relatively easy. While proteins require mild reaction conditions to retain their structural integrity, peptides can withstand harsher conditions and are thus more flexible when developing conjugating/labelling procedures¹³⁷. *In vivo*

metabolic stability is an important characteristic to consider when dealing with peptide-based probes due to proteolytic degradation in the blood. However, peptides can be structurally modified to improve stability along with other pharmacokinetic and pharmacodynamic properties¹³⁸. Phage display technology and other peptide screening techniques have provided an efficient, high-throughput way to produce libraries of biologically active peptides¹³⁹. Using these technologies, several PS-binding peptides have been identified¹⁴⁰⁻¹⁴⁷. Many of these PS-targeting peptides have been investigated in preclinical tumour models of treatment-induced apoptosis. When modifying peptides with fluorescent or radioactive labels, it is desirable to introduce the label at the N-terminus rather than on any of the amino acid side chains in order to lessen interference of the label with crucial binding properties of the peptide. CLSYPSYC, or PSP1, was N-terminally labelled with fluorescein for optical imaging of apoptosis in H460 human NSCLC xenografts in nude mice, and apoptosis was induced by treatment with camptothecin¹⁴⁵. In this model, treated NSCLC tumours showed significantly higher uptake of fluorescein-labelled PSP1 compared to untreated tumours, demonstrating its ability to detect therapy-induced tumour apoptosis. In another study using the same H460 mouse tumour model, PSP1 was labelled with the fluorescent dye Cy7.5 on its N-terminus and was able to target apoptotic tissue more efficiently than the same concentration of annexin V, even though the affinity of annexin V for PS was 10³-fold greater than that of PSP1¹⁴⁸. Another PS-targeted peptide, E3 hexapeptide (peptide sequence TLVSSL), was coupled to MR contrast agent ultrasmall superparamagnetic iron oxide (USPIO) and shown to be useful for MRI detection of radiation-induced apoptosis in mice with transplantable liver tumours¹⁴⁹. Hexapeptides LIKKPF and PGDLR,

identified by Burtea and colleagues¹⁴⁰, have been conjugated with diethylenetriaminepentaaceticacid (DTPA) and complexed with paramagnetic MRI contrast agent gadolinium chloride for MRI detection of liver apoptosis induced by anti-Fas antibody in mice¹⁴⁰. However, this MRI contrast agent was found to have low sensitivity, limiting its ability to detect small changes in PS exposure¹⁴⁰. To resolve this problem, the hexapeptides were coupled to USPIO nanoparticles that offer advantages such as higher sensitivity, and these USPIO-coupled peptides showed promise as apoptosis-imaging MRI agents in a mouse model of atherosclerotic apoptosis¹⁵⁰. Radiolabelling these peptides for PET imaging of apoptosis would also allow for higher sensitivity imaging. In an effort to develop LIKKPF and PGDLSR as PET imaging agents for detection of therapy-induced tumour apoptosis, these peptides have previously been labelled with ¹⁸F¹⁵¹. Since simple [¹⁸F]SFB labelling of the N-termini of the hexapeptides was less successful, the N-terminus of each peptide was modified with a cysteine residue for radiolabelling with thiol-selective maleimide prosthetic group *N*-[6-(4-[¹⁸F]fluoro-benzylidene)aminooxyhexyl]maleimide ([¹⁸F]FBAM)¹⁵¹. However, addition of a cysteine residue to the N-termini of these peptides resulted in a decrease in PS binding affinity¹⁴⁷. Establishment of a robust method for radiolabelling original peptides PGDLSR and LIKKPF on their N-termini using [¹⁸F]SFB would be more ideal. Another PS-binding peptide, 14-mer PS-binding peptide 6 (PSBP-6, sequence FNFRLKAGAKIRFG), has been identified and labelled on its N-terminus with ^{99m}Tc via a single amino acid chelator (SAAC) for SPECT imaging of apoptosis¹⁴⁶. This SPECT agent ^{99m}Tc-SAAC-PSBP-6 was evaluated in nude mice bearing B16/F10 murine melanoma tumours treated with paclitaxel in order to induce apoptosis. In this study,

biodistribution and autoradiography analyses of ^{99m}Tc -SAAC-PSBP-6 demonstrated much higher uptake of this tracer in tumours treated with paclitaxel versus untreated tumours¹⁴⁶. Preclinical SPECT imaging studies in mice also showed an increase in tumour uptake of ^{99m}Tc -SAAC-PSBP-6 in B16/F10 melanoma tumours after treatment with paclitaxel, as well as in 38C13 lymphoma tumours after treatment with cyclophosphamide¹⁵². Uptake of ^{99m}Tc -SAAC-PSBP-6 also negatively correlated with [^{18}F]FDG uptake in both of these tumour models, with [^{18}F]FDG uptake significantly decreasing after treatment with chemotherapy¹⁵². With such promising results demonstrating the utility of ^{99m}Tc -SAAC-PSBP-6 as a SPECT agent for imaging tumour cell death induced by chemotherapy in preclinical models, it would be useful to develop this 14-mer peptide as a PET imaging agent for cell death, which would provide better quality images and higher sensitivity.

1.5 Hypothesis and objectives

In this study, we hypothesize that a protein or peptide that targets PS exposed on dying cells can be radiolabelled with a positron-emitting radionuclide and used for *in vivo* PET imaging of drug-induced tumour cell death. We have tested this hypothesis by focusing on four objectives:

- 1) Radiolabelling PS-targeting molecules (wild-type annexin V and PS-binding peptides LIKKPF, PGDLSR and PSBP-6) with positron-emitting radionuclides, including ^{18}F , ^{68}Ga , and ^{64}Cu .
- 2) Evaluating the PS binding potencies of PS-targeting peptides LIKKPF, PGDLSR and PSBP-6 compared to annexin V.

- 3) Evaluating the ability of each PS-targeting radioligand to bind to EL4 murine lymphoma cells undergoing chemotherapy-induced cell death *in vitro*.
- 4) Evaluating the ability of the PS-targeting radioligands to image tumour cell death *in vivo* using a murine EL4 tumour model of chemotherapy-induced apoptosis.

2. MATERIALS AND METHODS

2.1. General

Purified recombinant wild-type human annexin V (1 mg or 5 mg, lyophilized) was purchased from BioVision (Milpitas, USA). Deionized water was obtained from a Barnstead Nanopure water filtration system (Barnstead Diamond Nanopure pack organic free RO/DIS). All chemicals and reagents were obtained from Sigma-Aldrich® unless otherwise stated. No-carrier added aqueous [^{18}F]F⁻ was produced in-house at the Edmonton PET Centre using an Advanced Cyclotron System TR 19/9 cyclotron. ^{68}Ga was obtained in the form of [^{68}Ga]gallium (III) chloride ([^{68}Ga]GaCl₃) in 1 M HCl from a $^{68}\text{Ge}/^{68}\text{Ga}$ generator (iThemba LABS, South Africa) purchased from isoSolutions, Inc., and was eluted using a SCINTOMICS GRP module (Fuerstenfeldbruck, Germany). ^{64}Cu was produced on a CS-15 biomedical cyclotron at Washington University School of Medicine (St. Louis, MO) in the form of [^{64}Cu]CuCl₂ in 0.1 M HCl, which was usually diluted with 100 mM ammonium acetate (NH₄OAc) buffer (pH 5.5). Water and buffers used for metal and radiometal chemistry procedures were first treated with Chelex® 100 resin (Bio-Rad) to eliminate heavy metal contamination. Radio-thin-layer chromatography (radio-TLC) detection was performed using a Bioscan AR-2000 Imaging Scanner. Semipreparative high performance liquid chromatography (HPLC) was performed on a Gilson system consisting of a 321 pump and a 171 diode array detector, and a Berthold Technologies Herm LB 500 was used as radiodetector. Analytical HPLC was performed on a Shimadzu system equipped with a DGU-20A5 degasser, SIL-20A HT autosampler, LC-20AT pump, SPD-M20A photodiode-array detector, and Ramona

Raytest radiodetector. All radiopeptides subjected to analytical HPLC were analyzed using a Phenomenex Luna® 10u C18(2) 100Å, 250 × 4.6 mm column and the following gradient of water/0.2% (v/v) trifluoroacetic acid (TFA) (A) and CH₃CN (B): 0 min: 10% B, 10 min: 30% B, 10-17 min: 50% B, 17-23 min: 70% B, 23-27 min: 90% B, 27-30 min: 90% B (flow rate = 1 mL/min). UV absorbance was monitored at 210 nm and/or 254 nm. Rotary evaporation of product solvents was carried out using a Buchi HB 140 Rotavapor-M with a Fisher Maxima C Plus Model M8C pump. Quantification of radioactive samples during radiochemistry was achieved using a Biodex ATOMLAB™ 400 dose calibrator. Reaction parameters were carried out with an Eppendorf Thermomixer®. Centrifugation of samples was done in a Hettich Zentrifugen Rotina 35R or a Fisher Scientific Mini Centrifuge. Radioactive samples were measured using a PerkinElmer 2480 Automatic Gamma Counter WIZARD2®. Cells stained with Trypan Blue were counted using a Bio-Rad TC10™/ TC20™ Automated Cell Counter. Flow cytometry was carried out using a Fluorescence Activated Cell Sorter (BD FACSCaliber™) bench top analyzer. For fluorescence confocal microscopy, a Zeiss LSM 710 confocal microscope was used.

Radio-sodium dodecyl sulfate polyacrylamide gel electrophoresis (SDS-PAGE) was performed on IDGel™ Express IR121S-20 precast gels (12% tris buffer), which were run in a Bio-Rad Mini PROTEAN® Tetra Cell with running buffer. Gels were run with a constant current of 30 mA for approximately 1 h, and Radio-SDS-PAGE gels were scanned on a Fujifilm BAS 5000 phosphor imager and analyzed by AIDA Image Analyzer Software Version 4.50. The gels were then stained with Coomassie® Brilliant Blue R-250 (Bio-Rad) for 30 min at 37 °C, and left in destaining solution overnight.

Bicinchoninic acid (BCA) protein assays were performed as instructed from the BCA Protein Assay Kit (Pierce™): standards containing bovine serum albumin (BSA) in phosphate-buffered saline (PBS) (pH 7.4) were prepared at concentrations of 0, 50, 100, 200, 300, 400, 600, and 800 µg/mL. 25 µL of each concentration of standard was pipetted into a 96-well plate, as well as 25 µL of the sample with unknown protein content. A solution of 2% BCA Reagent B (Pierce™) in BCA Reagent A (Pierce™) was made, and 200 µL of this solution was added to each well containing standard or sample. The plate was left to incubate for 25 min at 37 °C (Fisher Scientific Isotemp Incubator Model 546). Protein content in each well was then determined from absorbance measurements using a Molecular Devices Spectramax 340PC microplate reader.

In-house preparations of buffers were as follows: Phosphate-buffered saline (PBS) (140 mM NaCl, 2.7 mM KCl, 5.4 mM Na₂HPO₄, 570 µM KH₂PO₄, pH 7.4), 2.5 mM Ca²⁺ binding buffer (10 mM 4-(2-hydroxyethyl)-1-piperazineethanesulfonic acid (HEPES) (pH 7.4), 140 mM NaCl, 2.5 mM CaCl₂), 1.25 mM Ca²⁺ binding buffer (10 mM HEPES (pH 7.4), 140 mM NaCl, 1.25 mM CaCl₂), Ca²⁺-negative binding buffer (10 mM HEPES (pH 7.4), 140 mM NaCl), running buffer for SDS-PAGE (25 mM Tris, 192 mM glycine, 0.1% SDS), Destaining solution (10% glacial acetic acid, 20% methanol, 70% deionized water).

2.2. Synthesis of peptides, labelling precursors and cold references

2.2.1. Synthesis of peptides and conjugates (general procedure)

The 4-benzyloxybenzyl alcohol (Wang) resin, preloaded with the C-terminal amino acid (Phe, loading 0.61 mmol/g; Arg, 0.63 loading mmol/g), provided the solid support for the synthesis of peptides LIKKPF, FBz-LIKKPF, CLIKKPF, PGDLSR, FBz-PGDLSR, and CPGDLSR. Rink Amide 4-methylbenzhydrylamine (MBHA) resin (100-200 mesh) provided the solid support for synthesis of peptides H₂N-FNFRLKAGAKIRFG-CONH₂ (PSBP-6), H₂N-CFNFRLKAGAKIRFG-CONH₂ (C-PSBP-6), FBAM-CFNFRLKAGAKIRFG-CONH₂ (FBAM-C-PSBP-6), and NOTA-Bz-thiourea-Ava-FNFRLKAGAKIRFG-CONH₂ (NOTA-PSBP-6). Peptides were synthesized by solid-phase peptide synthesis (SPPS) using a fully automated peptide synthesizer (Syro I, Multisyn-tech/Biotage). The used method consisted of swelling pre-loaded resin (Wang or Rink Amide MBHA) in 2 mL of dimethylformamide (DMF) for 15 min. Fluorenylmethyloxycarbonyl (fmoc) group deprotection was achieved by the treatment with 40% piperidine/DMF for 5 min and followed by a second incubation with 20% piperidine/DMF for 15 min. Fmoc-protected amino acids or N-terminal 4-fluorobenzoic acid (FBz) (5 eq) were activated and coupled using 5 eq of O-benzotriazole-N,N,N',N'-tetramethyl-uronium-hexafluoro-phosphate (HBTU), 5 eq of ethyl-2-cyano-2-(hydroxyimino) acetate (Oxyma), and 10 eq of N,N-diisopropylethylamine (DIPEA) over a 60 min time period followed by washing steps with DMF. Incubation with an acidic cocktail containing 87.5% TFA, 5% water, 5% thioanisole, and 2.5% 1,2-ethanedithiol (EDT) for 3.5 h led to the cleavage of the

assembled peptides from the resin with simultaneous deprotection of amino acid side chains. The peptides were separated from the resin through a syringe filter and precipitated by the addition of ice-cold diethyl ether. The crude peptides were obtained by removing the residual ether using a syringe filter and dried under vacuum. Purification by HPLC and subsequent lyophilization gave sufficiently pure peptides (>95% purity based on HPLC analysis) as white solids. SPPS procedures and peptide quality controls were carried out by Cody Bergman. Conjugation of peptides with nonradioactive groups FBz, *N*-[6-(4-[¹⁸F]fluoro-benzylidene)aminooxyhexyl]maleimide (FBAM), FITC or NOTA were also carried out by Cody Bergman.

2.2.2. *Synthesis of PGDLSR*

PGDLSR was synthesized according to the general procedure starting with 50 mg of Fmoc-Arg-Wang resin, and purified by semi-preparative HPLC using a gradient of water/0.2% TFA (A) and CH₃CN (B): 20% eluent B for 5 min, increased to 35% eluent B over an additional 5 min, then to 70% eluent B over 20 min, holding at that point for a final 10 min. Analysis: $t_R = 10.7$ min. MW C₂₆H₄₅N₉O₁₀ calculated 643.33, found low resolution mass spectrometry (LR-MS) (electrospray ionization (ESI), positive) m/z 644.3 [M + H]⁺, 666.3 [M + Na]⁺, 322.7 [M + 2H]²⁺.

2.2.3. *Synthesis of FBz-PGDLSR*

FBz-PGDLSR was synthesized according to the general procedure using 50 mg of FBz, and purified by semi-preparative HPLC using the same gradient used for PGDLSR purification. Analysis: $t_R = 20.6$ min. MW C₃₃FH₄₈N₉O₁₁ calculated 765.35, found LR-

MS (matrix-assisted laser desorption ionization (MALDI), positive) m/z 766.4 $[M + H]^+$, 788.4 $[M + Na]^+$.

2.2.4. *Synthesis of CPGDLSR*

CPGDLSR was obtained according to the general procedure and purified by semi-preparative HPLC using the same gradient used for PGDLSR purification. Analysis: $t_R = 21.3$ min. MW $C_{29}H_{50}N_{10}O_{11}S$ calculated 746.34, found LR-MS (MALDI, positive) m/z 747.3 $[M + H]^+$.

2.2.5. *Synthesis of LIKKPF*

LIKKPF was synthesized according to the general procedure starting with 50 mg of Fmoc-Phe-Wang resin, and purified by semi-preparative HPLC using the same gradient used for PGDLSR purification. Analysis: $t_R = 17.0$ min. MW $C_{38}H_{64}N_8O_7$ calculated 744.49, found LR-MS (ESI, positive) m/z 745.5 $[M + H]^+$, 373.3 $[M + 2H]^{2+}$.

2.2.6. *Synthesis of FBz-LIKKPF*

FBz-LIKKPF was obtained according to the general procedure using 50 mg of FBz, and purified by semi-preparative HPLC using the same gradient used for PGDLSR purification. Analysis: $t_R = 23.6$ min. MW $C_{45}FH_{67}N_8O_9$ calculated 866.51, found LR-MS (ESI, positive) m/z 867.5 $[M + H]^+$, 889.5 $[M + Na]^+$, 434.3 $[M + 2H]^{2+}$.

2.2.7. Synthesis of CLIKKPF

CLIKKPF was obtained according to the general procedure, and purified by semi-preparative HPLC using the same gradient used for PGDLSR purification. Analysis: $t_R = 18.9$ min. MW $C_{41}H_{69}N_9O_8S$ calculated 847.50, found LR-MS (ESI, positive) m/z 848.5 $[M + H]^+$, 870.5 $[M + Na]^+$, 424.8 $[M + 2H]^{2+}$.

2.2.8. Synthesis of PSBP-6

PSBP-6 was synthesized according to the general procedure starting with 50 mg of Rink Amide MBHA resin. It was purified by semi-preparative HPLC using a gradient of water/0.2% TFA (A) and CH_3CN (B): 10% eluent B for 5 min, increased to 30% eluent B over an additional 5 min, then to 50% eluent B over 15 minutes, then to 80% eluent B over 5 min, holding at that point for a final 10 min. Analysis: $t_R = 22.0$ min. MW $C_{77}H_{122}N_{24}O_{15}$ calculated 1622.95, found LR-MS (ESI, positive) m/z 1623.9 $[M + H]^+$, 1661.9 $[M + K]^+$.

2.2.9. Synthesis of C-PSBP-6

C-PSBP6 was synthesized according to the general procedure starting with 50 mg of Rink Amide MBHA resin, and purified by semi-preparative HPLC using the same gradient used to purify PSBP-6. Analysis: $t_R = 24.0$ min. MW $C_{80}H_{127}N_{25}O_6S$ calculated 1726.00, found LR-MS (ESI, positive) m/z 1726.9 $[M + H]^+$, 1749.9 $[M + Na]^+$.

2.2.10. Synthesis of FBz-PSBP-6

FBz-PSBP-6 was obtained according to the general procedure using 50 mg of FBz, and purified by semi-preparative HPLC using the same gradient used to purify PSBP-6. Analysis: $t_R = 27.8$ min. MW $C_{84}H_{125}FN_{24}O_{16}$ calculated 1746.04, found LR-MS (ESI, positive) m/z 1746.1 $[M + H]^+$, 1768.1 $[M + Na]^+$.

2.2.11. Synthesis of NOTA-Bn-thiourea-Ava-PSBP-6 (NOTA-PSBP-6)

PSBP-6 was conjugated with metal chelating group NOTA on its N-terminal amino group via an aminovaleric acid (ava) spacer. NOTA-PSBP-6 was synthesized according to the general procedure starting with 50 mg of Rink Amide MBHA resin. After the final amino acid (ava), 22 mg of p-SCN-Bn-NOTA (1.1 eq to resin loading) and 55 μ L (10 eq to resin loading) of triethylamine were added to the swelled resin in 0.5 mL of DMF. The resin was left to react for 17.5 h at room temperature, washed, and cleaved as per the general procedure. NOTA-PSBP-6 was purified by semi-preparative HPLC using the same gradient used to purify PSBP-6. Analysis: $t_R = 26.9$ min. MW $C_{102}H_{157}N_{29}O_{22}S$ calculated 2172.2, found LR-MS (matrix-assisted laser desorption ionization-time of flight (MALDI-TOF), positive) m/z 2173.8 $[M + H]^+$.

2.2.12. Labelling NOTA-PSBP-6 with cold Ga^{3+}

To synthesize cold reference Ga-NOTA-PSBP-6, 40 eq of cold $GaCl_3$ (measured out under a stream of $N_{2(g)}$ to prevent fuming) was added to excess EDTA in 100 mM NH_4OAc buffer (pH 5.5) and left to incubate for 5 min at room temperature. One eq of precursor NOTA-PSBP-6 in 100 mM ammonium acetate (NH_4OAc) buffer (pH 5.5) was

then added to the GaCl₃-EDTA mixture (2 mL total reaction volume) and incubated at 60 °C for 1 h, after which the temperature was lowered to 37 °C and the reaction proceeded overnight. The Ga-NOTA-PSBP-6 product was purified by semi-preparative HPLC using a gradient of water/0.2% TFA (A) and CH₃CN (B): 0-10 min: 10% B, 10-25 min: increase to 50% B, 25-30 min: increase to 80% B, 30-40 min: isocratic at 80% B. Analysis: t_R = 29.5 min. HPLC product was lyophilized and pure peptide was obtained as a white powder. MW C₁₀₂H₁₅₄GaN₂₉O₂₂S calculated 2240.3, found LR-MS (MALDI-TOF, positive) *m/z* 2240.5 [M + H]⁺.

2.2.13. Labelling NOTA-PSBP-6 with cold Cu²⁺

To synthesize cold reference Cu-NOTA-PSBP-6, 30 eq of cold copper (II) chloride (CuCl₂) was added to excess EDTA in 100 mM NH₄OAc buffer (pH 6) and left to incubate for 30 min at room temperature. 1 eq of precursor NOTA-PSBP-6 in 100 mM NH₄OAc buffer (pH 6) was added to the CuCl₂-EDTA mixture (2 mL total reaction volume) and incubated at 60 °C for 1 h, after which the temperature was lowered to 37 °C and the reaction proceeded overnight. The Cu-NOTA-PSBP-6 product was purified by semi-preparative HPLC using a gradient of water/0.2% TFA (A) and CH₃CN (B): 0-10 min: 10% B, 10-25 min: 50% B, 25-30 min: 80% B, 30-40 min: 80% B. Analysis: t_R = 25.8 min. HPLC product was lyophilized and pure peptide was obtained as a light green powder. MW C₁₀₂H₁₅₄CuN₂₉O₂₂S calculated 2234.1, found LR-MS (MALDI-TOF, positive) *m/z* 2235.4 [M + H]⁺.

2.2.14. Coupling of FBAM to CPGDLSR, CLIKKPF and C-PSBP-6 (general procedure)

Coupling of CPGDLSR and CLIKKPF with FBAM was achieved by adding 1 eq of non-radioactive FBAM in 120 μ L of CH₃CN to 1.5 eq of precursor peptide dissolved in 120 μ L of PBS (pH 7.2). The two solutions were mixed and incubated for 2-2.5 h at 60 °C. Purification by HPLC and subsequent lyophilization gave sufficiently pure peptides as white solids.

2.2.15. Synthesis of FBAM-CPGDLSR

FBAM-CPGDLSR was synthesized according to the general procedure and purified by semi-preparative HPLC using a gradient of water/0.2% TFA (A) and CH₃CN (B): 10% eluent B for 5 min, increased to 25% eluent B over an additional 5 min, to 50% eluent B over 15 min, then to 80% eluent B over 5 minutes, then holding at that point for a final 10 min. Analysis: t_R = 31.2 min. MW C₄₆H₆₉FN₁₂O₁₄S calculated 1064.48, found LR-MS (MALDI, positive) m/z 1065.5 [M + H]⁺.

2.2.16. Synthesis of FBAM-CLIKKPF

FBAM-CLIKKPF was obtained according to the general procedure, and purified by semi-preparative HPLC using the same gradient used to purify FBAM-CPGDLSR. Analysis: t_R = 32.2 min. MW C₅₈H₈₈FN₁₁O₁₁S calculated 1165.64, found LR-MS (MALDI, positive) m/z 1166.6 [M + H]⁺, 1188.6 [M + Na]⁺.

2.2.17. Synthesis of FBAM-C-PSBP-6

The non-radioactive reference compound FBAM-C-PSBP-6 was prepared according to the general procedure. HPLC purification of the products was accomplished using a gradient of water/0.2% TFA (A) and CH₃CN (B): 10% eluent B for 5 min, increased to 30% eluent B over an additional 5 min, then to 50% eluent B over 15 minutes, then to 80% eluent B over 5 min, holding at that point for a final 10 min. Analysis: $t_R = 32.2$ min. MW C₉₈H₁₄₇FN₂₆O₁₉S calculated 2044.4, found LR-MS (ESI, positive) m/z 2045.1 [M + H]⁺.

2.2.18. Synthesis of FITC-Ava-PSBP-6 (FITC-PSBP-6)

The fluorescent compound FITC-PSBP-6 was prepared according to the general procedure. PSBP-6 was conjugated with FITC on its N-terminal amino group via an ava spacer. 1 eq of FITC-N=C=S was added to the resin loading in 500 μ L of 12:7:5 Pyridine:DMF:DCM and allowed to couple overnight. HPLC purification of the products was accomplished using a gradient of water/0.2% TFA (A) and CH₃CN (B): 10% eluent B for 5 min, increased to 30% eluent B over an additional 5 min, then to 50% eluent B over 15 minutes, then to 80% eluent B over 5 min, holding at that point for a final 10 min. Analysis: $t_R = 27.4$ min. MW C₁₀₃H₁₄₂N₂₆O₂₁S calculated 2112.5, found LR-MS (MALDI-TOF, positive) m/z 2113.8 [M + H]⁺.

2.3. Radiochemistry

2.3.1. Synthesis of ^{18}F -labelled prosthetic groups

2.3.1.1. Synthesis of $[^{18}\text{F}]\text{SFB}$

The prosthetic group *N*-succinimidyl-4- $[^{18}\text{F}]$ fluorobenzoate ($[^{18}\text{F}]\text{SFB}$) was prepared by Jenilee Way or Cody Bergman via a three-step procedure using a remotely controlled GE TRACERlab™ FX automated synthesis module according to Maeding et al¹⁵³. To ensure a high radiochemical purity of $[^{18}\text{F}]\text{SFB}$ for radiolabelling annexin V, 1 mL of $[^{18}\text{F}]\text{SFB}$ in CH_3CN obtained off the GE TRACERlab™ FX module was purified by HPLC using a Phenomenex LUNA® C18(2) (100Å, 250 × 10 mm, 10 μm) column and the following gradient: solvent A: water; solvent B: CH_3CN . 0 min: 15% B, 8 min: 50% B, 9-25 min: 70% B (flow rate = 3 mL/min). At a retention time of about 15 min, the broad $[^{18}\text{F}]\text{SFB}$ peak was collected into a 50 μL pear-shaped flask, and solvent was removed by a rotary evaporator. The dry $[^{18}\text{F}]\text{SFB}$ was then used for radiolabelling annexin V.

2.3.1.2. Synthesis of $[^{18}\text{F}]\text{FBEM}$

N-[2-(4- ^{18}F -fluorobenzamido)ethyl]maleimide ($[^{18}\text{F}]\text{FBEM}$) was manually synthesized by Dr. James Knight from $[^{18}\text{F}]\text{SFB}$ in a modified version of the procedure reported by Cai et al¹⁵⁴. 3 mg of *N*-(2-aminoethyl)maleimidetrifluoroacetate salt (the amine) was dissolved in 500 μL of 50 mM borate buffer (pH 8.4) and reacted with 500 μL of $[^{18}\text{F}]\text{SFB}$ in CH_3CN (obtained from the GE TRACERlab™ FX module) for 20 min

at 50 °C. [¹⁸F]FBEM was purified by HPLC using the same column and gradient that was used for [¹⁸F]SFB purification, and it also eluted with a retention time of about 15 min. The purified [¹⁸F]FBEM solution was placed on a rotary evaporator until all solvent was removed, and the resulting dry [¹⁸F]FBEM was used for radiolabelling annexin V.

2.3.1.3. Synthesis of [¹⁸F]FBAM

N-[6-(4-[¹⁸F]fluoro-benzylidene)aminoxyhexyl]maleimide ([¹⁸F]FBAM)¹⁵⁵ was synthesized by Jenilee Way or Cody Bergman on an automated synthesis GE TRACERlab™ FX module according to Kniess et al¹⁵⁶. It was used directly from the automated synthesis unit for radiolabelling peptides.

2.3.2. Radiolabelling wild-type annexin V with ¹⁸F-containing prosthetic groups

I assisted Dr. James Knight with the optimization of procedures for radiolabelling annexin V with ¹⁸F.

2.3.2.1. Labelling wild-type annexin V with [¹⁸F]SFB

An annexin V aliquot (100-200 µg in 100 µL of either PBS (pH 7.4) or tris HCl buffer (pH 8.2) frozen at -20 °C) was warmed to room temperature and added to the dry [¹⁸F]SFB in a 50 µL pear-shaped flask, vortexed for 30 s, and then transferred to an eppendorf. Another 50 µL of PBS was used to rinse the walls of the flask and added to the reaction mixture. Minimization of liquid transfers and contact surface area with reaction vessels were necessary in order to reduce surface adsorption of the protein. The reaction mixture was then placed on the thermoshaker at 30 °C for 40 min to produce

[¹⁸F]SFB-annexin V. [¹⁸F]SFB-annexin V was purified by size exclusion chromatography (SEC) using either a PD-10 desalting column (GE Healthcare) or a 10DG desalting column (Bio-Rad Econo-Pac®) eluted with PBS into 250 µL fractions (8 drops per fraction). The collected high molecular weight fractions containing the highest activity were directly used for cell binding or preclinical PET imaging studies. For quality control, a 5 µL sample of the crude reaction mixture and a 5 µL sample of purified [¹⁸F]SFB-annexin V were reduced with dithiothreitol (DTT) at 95 °C for 5 min and subjected to SDS-PAGE. The SDS-PAGE gels were then analyzed by phosphor imaging and staining/destaining. Specific activity of [¹⁸F]SFB-annexin V used for animal imaging studies was determined by measuring the activity of a purified fraction with a dose calibrator, and then conducting a BCA assay to quantify the protein in the fraction.

2.3.2.2. *Labelling wild-type annexin V with [¹⁸F]FBEM*

Once [¹⁸F]FBEM was manually synthesized from [¹⁸F]SFB and rotovapped to dryness, the same procedure that was used to label annexin V with [¹⁸F]SFB was used by Dr. James Knight to label annexin V with [¹⁸F]FBEM. Like [¹⁸F]SFB-annexin V, [¹⁸F]FBEM-annexin V was purified by size exclusion chromatography and directly used for cell binding or preclinical PET imaging studies. SDS-PAGE was carried out on crude and purified samples for quality control.

2.3.3. *Synthesis of ⁶⁴Cu-NOTA-annexin V*

⁶⁴Cu-NOTA-annexin V synthesis was developed and carried out by Dr. Christian Foerster, and the product was handed off to me for quality control and subsequent PS binding assays.

2.3.3.1. *Synthesis of NOTA-annexin V.*

In order to label wild-type annexin V with ⁶⁴Cu, it was first randomly functionalized with NOTA through bioconjugation of p-NCS-Bn-NOTA via thiourea formation with primary amino groups present in the protein (lysine residues and N-terminus). To do this, 500 μ L of annexin V stock solution (23.4 μ M in PBS) was re-buffered in 2 mL of carbonate buffer (100 mM sodium bicarbonate, 280 mM of NaCl, pH 9.15) by spin filtration (Millipore Amicon ultra-4 10k MWCO; regenerated cellulose; preconditioned by filtrating 1 mL of carbonate buffer at 4000 xg for 15 min at room temperature using a swinging bucket centrifuge). The mixture was centrifuged at 4000 xg for 15 min at room temperature and the filtrate was discarded. The procedure was repeated 3 times resulting in a dilution factor of ~50,000. Remaining annexin V was recovered by adding 400 μ L of carbonate buffer. In order to remove potential metal ions non-specifically bound to annexin V, 100 μ L of NOTA stock solution (11.7 mM in carbonate buffer) were added to the annexin V solution, and the mixture was shaken at 30 °C for 30 min. Subsequently, 19.5 μ L of p-NCS-Bn-NOTA stock solution (3.0 mM in carbonate buffer) was added and shaken at 30 °C for 180 min. The reaction was quenched by adding 1 mL NH₄OAc buffer (100 mM NH₄OAc, 140 mM NaCl, pH 7.4) and was shaken at 30 °C for 30 min. The reaction mixture was purified by spin filtration. For each

purification step, 3 mL of NH₄OAc buffer was added and centrifuged. The final product was dissolved in 500 μL of 100 mM NH₄OAc buffer (pH 7.4), producing a concentration of 0.64 mg/mL as determined by BCA protein quantification. Each annexin V molecule was conjugated with an average of 1.4 NOTA groups, determined by titration of NOTA-annexin V with [⁶⁴Cu]Cu(OAc)₂.

2.3.3.2. Labelling NOTA-annexin V with ⁶⁴Cu.

100 μL of 100 mM NH₄OAc buffer (pH 5.5) was added to 90 μg (2.5 nmol) of NOTA_{1.4}-annexin V. This was reacted with 15-20 MBq of [⁶⁴Cu]CuCl₂ at 30 °C for 45 min to give ⁶⁴Cu-labelled NOTA-annexin V. To bind free [⁶⁴Cu]Cu²⁺ in solution and to remove nonspecifically annexin V-bound [⁶⁴Cu]Cu²⁺, 5 μL of 10 mM EDTA (in 100 mM NH₄OAc buffer; pH 5.5) was added, and the mixture was shaken for an additional 15 min at 30 °C. Radio-TLC of the crude reaction mixture showed radiolabelling yields of > 95%, performed using Alugram® RP-18W UV254 (Machery-Nagel) as solid phase and 10 mM EDTA in 100 mM NH₄OAc (pH 5.5) as mobile phase (R_f of product = 0.0). SEC was applied to purify the product in PBS, producing radiochemical purities of > 98%. For the radiometric PS binding assay studies, ⁶⁴Cu-NOTA-annexin V was further diluted to an activity concentration of 1 kBq/μL, corresponding to 4.3 ng/μL of NOTA-annexin V. For quality control, a 5 μL sample of purified ⁶⁴Cu-NOTA-annexin V was reduced with DTT at 95 °C for 5 minutes and subjected to SDS-PAGE. The SDS-PAGE gel was then analyzed by phosphor imaging and staining/destaining.

2.3.4. Radiolabelling PGDLSR with [¹⁸F]SFB

Amine-directed prosthetic group [¹⁸F]SFB was used to label the N-terminal primary amino group on peptide PGDLSR. I worked with Dr. Susan Richter on procedure development and optimization. Approximately 0.5 mg of PGDLSR was dissolved in 200 μL of disodium phosphate (Na₂HPO₄) buffer (0.05 M, pH 9). To this solution, 100 μL (~100 MBq) of [¹⁸F]SFB in CH₃CN obtained directly off the GE TRACERlab™ FX module was added, and the reaction mixture was placed on the thermoshaker at 60 °C for 45 min. The resulting product ([¹⁸F]FB-PGDLSR) was purified by semi-preparative HPLC using a Phenomenex Jupiter® 10 μm Proteo C12 (90 Å, 250 x 10 mm) column and the following gradient of water/0.2% (v/v) TFA (A) and CH₃CN (B): 0-10 min: 10% B, 10-25 min: increase to 50% B, 25-30 min: increase to 70% B, 30-35 min: isocratic at 70% B, 35-39 min: increase to 90% B, 39-45 min: isocratic at 90% B (flow rate = 2 mL/min). Purified [¹⁸F]FB-PGDLSR was obtained at t_R = 30.8 min, with radiochemical yields of 36 ± 7.7% (decay-corrected). Radiochemical purities of > 96% were achieved, as determined by analytical radio-HPLC (t_R = 16.9 min).

2.3.5. Radiolabelling LIKKPF with [¹⁸F]SFB

Amine-directed prosthetic group [¹⁸F]SFB was used to label the N-terminal primary amino group on peptide LIKKPF. I worked with Dr. Susan Richter on procedure development and optimization. To prevent [¹⁸F]SFB from reacting with the two lysine residues present on LIKKPF, these primary amine-containing side chains were protected by tert-butyloxycarbonyl ("boc") protecting groups, with the C-terminus of the peptide still bound to resin. 200 μL DMF was added to 10 mg of boc-protected LIKKPF,

allowing the resin to swell for 15 min. [^{18}F]SFB obtained from the GE TRACERlab™ FX module was placed on the rotary evaporator until all solvent was removed, and the dry [^{18}F]SFB was dissolved in 2 x 50 μL of DMF and added to the peptide solution along with 100 μL of Na_2PO_4 buffer (0.05 M, pH 9). This mixture was left to react at 50 °C for 45 min with vigorous shaking. The mixture was then filtered and the resulting resin-protected product was washed with 1 mL DMF and then 1 mL DCM. To remove the boc protecting groups from the radiolabelled product, 300 μL of an acidic cleavage solution (95:4:1 TFA:H₂O:trispropylsilane) was added to the boc-protected radiolabelled product, which was then placed on the thermoshaker at 50 °C for 20 minutes with gentle shaking. The resulting deprotected product ([^{18}F]FB-LIKKPF) was then pushed through a filter to remove the cleaved resin, and this product-containing filtrate was purified by semi-preparative HPLC using the same column and gradient that was used to purify [^{18}F]FB-PGDLSR. Purified [^{18}F]FB-LIKKPF was obtained at $t_r = 31.1$ min, with radiochemical yields of $25 \pm 1.5\%$ (decay-corrected). Radiochemical purities of $> 99\%$ were achieved, as determined by analytical radio-HPLC ($t_R = 18.8$ min).

2.3.6. Radiolabelling PSBP-6 with [^{18}F]SFB

In order to label PSBP-6 with ^{18}F , Dr. Susan Richter and I first attempted to label the N-terminus of PSBP-6 with [^{18}F]SFB in solution (no protection groups). Generally, 200-300 μL of buffer was added to PSBP-6 (precursor), to which 100-500 μL of [^{18}F]SFB in acetonitrile obtained from the GE TRACERlab™ FX module was added and then placed on the thermoshaker. A range of reaction parameters were tried, using 0.5-1.5 mg of PSBP-6 (precursor) buffered in Na_2HPO_4 buffer (pH 9) or potassium

phosphate/borax buffer (pH 7.8, 8.0, 8.2 and 8.4), reaction temperatures ranging from 40-50 °C, and reaction times between 10-30 min. Our cold reference FBz-PSBP-6 showed a retention time of 30.5 min when analyzed by semi-preparative HPLC using the same column and gradient used to purify the other two [¹⁸F]SFB-labeled peptides. However, when we attempted to purify the crude [¹⁸F]SFB-labeled reaction product via this HPLC method, we observed no product with this desired retention time. Thus, we were unable to synthesize our desired N-terminally labeled product in solution.

Since PSBP-6 contains many amino acid side chains that may react with [¹⁸F]SFB, we also tried the labelling using resin-attached PSBP-6 with many protecting groups to shield these side chains from reacting. Triphenylmethyl (trt) groups were used to protect asparagine side chains, 2,2,4,6,7-pentamethyldihydrobenzofuran-5-sulfonyl (Pbf) groups were used to protect arginine side chains, and lysine residues were protected with boc groups (protected peptide sequence: Phe-Asn(trt)-Phe-Arg(pbf)-Leu-Lys(boc)-Ala-Gly-Ala-Lys(boc)-Ile-Arg(pbf)-Phe-Gly-NH-Resin). About 10 mg of protected peptide was added to 200 µL of DMF to allow the resin to swell for 15 min. 1-2 mL of [¹⁸F]SFB obtained from the GE TRACERlab™ FX module was placed on the rotary evaporator until all solvent was removed, and the dry [¹⁸F]SFB was dissolved in 2 x 50 µL of DMF, which was then added to the protected peptide in DMF. To this solution, 100 µL of Na₂PO₄ buffer (0.05 M, pH 9) was added, and this mixture was left to react at 50 °C for 45 min with vigorous shaking. The mixture was then filtered and the resulting resin-protected product was washed with 1 mL DMF and then 1 mL DCM. To remove the protecting groups, 300 µL of an acidic cleavage solution (95:4:1 TFA:H₂O:trispropylsilane) was added to the protected radiolabelled product, which was

then placed on the thermoshaker at 50 °C for 20 min with gentle shaking. The resulting deprotected product was then pushed through a filter to remove the cleaved resin, and this product-containing filtrate was purified by semi-preparative HPLC. We were able to isolate our desired N-terminally labelled product [¹⁸F]FB-PSBP-6 at t_R = 30.8 min (Quality control was carried out by analytical radio-HPLC (t_R = 18.3 min, co-injected with cold reference)). However, we were only able to obtain radiochemical yields of <2%. Thus, labelling of PSBP-6 with ¹⁸F using [¹⁸F]SFB was unsuccessful, and a different ¹⁸F radiolabelling approach was required.

2.3.7. Radiolabelling C-PSBP-6 with [¹⁸F]FBAM

In order to use a thiol-directed radiolabelling approach to label PSBP-6 with ¹⁸F, Dr. Susan Richter and I used maleimide-containing prosthetic group [¹⁸F]FBAM to react with the thiol group of a cysteine residue added to the peptide N-terminus (C-PSBP-6, sequence CFNFRLKAGAKIRFG-CONH₂). ~0.5 mg of C-PSBP-6 was first dissolved in 100 μL of 50:50 dimethyl sulfoxide (DMSO):PBS (pH 7.4) containing 1 mM of reducing agent tris(2-carboxyethyl)phosphine (TCEP), which prevents disulfide bond formation between cysteine residues and thus dimerization of the peptide. 60 μL of [¹⁸F]FBAM in CH₃CN (obtained off the GE TRACERlab™ FX module) was added to the peptide solution, and was left to react at 60 °C for 45 min. The resulting [¹⁸F]FBAM-C-PSBP-6 product was purified by semi-preparative HPLC with a retention time of 31.9 min as verified by co-injection with cold reference FBAM-C-PSBP-6.

2.3.8. Radiolabelling *NOTA-PSBP-6* with ^{68}Ga

Dr. Susan Richter assisted with development and optimization of the procedure for labelling *NOTA-PSBP-6* with ^{68}Ga . 200 μL of 4 M sodium acetate (NaOAc) buffer (pH 9) was added to 40 μg (20 nmol) of *NOTA-PSBP-6*. 600 μL (\sim 100 MBq) of [^{68}Ga]GaCl₃ in 1 M HCl eluted from the $^{68}\text{Ge}/^{68}\text{Ga}$ generator was added to the peptide solution to obtain a reaction pH of 3.5, which was left to react at 60 °C for 15 min. 12 μL of 10 mM EDTA (100 mM NH₄OAc buffer; pH 5.5) was then added, and the solution was placed back on the thermoshaker for 10 min at 60 °C. The labelled peptide was purified by solid-phase extraction on an Oasis® HLB cartridge (Waters) preconditioned with PBS and ethanol. ^{68}Ga -*NOTA-PSBP-6* was loaded onto the cartridge with 5 mL PBS, and washed with another 5 mL PBS. Eluting the labelled peptide was difficult, as it became trapped at the top of the cartridge where it was loaded. In order to recover ^{68}Ga -*NOTA-PSBP-6*, the cartridge was flipped upside-down and the labelled peptide was slowly eluted (30 seconds) with \sim 1 mL ethanol. Quality control was carried out by radio-TLC using two systems: EMD Merck silica gel 60 F₂₅₄ TLC plates with 10 mM EDTA in 100 mM NH₄OAc as mobile phase (R_f of product = 0.0); and DC-Fertigfolien ALUGRAM® RP-18W/UV₂₅₄ TLC plates with 1 M NH₄OAc/methanol (1:1 v/v) as mobile phase (R_f of product = 0.0). Analytical HPLC was also used for quality control during metabolic stability studies, and the retention time for ^{68}Ga -*NOTA-PSBP-6* was 16.5 min, as determined by co-injection with cold reference *Ga-NOTA-PSBP-6*.

2.3.9. Radiolabelling *NOTA-PSBP-6* with ^{64}Cu

10-32 μL aliquots containing 2 μg (1 nmol) of precursor (*NOTA-PSBP-6*) were prepared. 100 μL of 100 mM NH_4OAc buffer (pH 5.5-6) was added to the aliquot, followed by 5-50 MBq of ^{64}Cu in 100 mM NH_4OAc buffer (pH 5.5). This mixture was left to react for 60 min at 60 $^\circ\text{C}$. Quality control of the product was performed by radio-TLC using EMD Merck silica gel 60 F₂₅₄ TLC plates with 10 mM EDTA in 100 mM NH_4OAc as mobile phase (R_f of product = 0.0), semi-preparative HPLC using a Phenomenex LUNA[®] C18(2) (100 \AA , 250 \times 10 mm, 10 μm) column and the following gradient of water/0.2% TFA (A) and CH_3CN (B): 0-10 min: 10% B, 10-25 min: increase to 50% B, 25-30 min: increase to 90% B, 30-35 min: isocratic at 90% B (flow rate = 2 mL/min) (t_R = 30.1 min), or analytical HPLC using the usual peptide gradient (t_R = 16.4 min). No purification step was necessary, as radiochemical yields of > 95% (RCP > 95%) were obtained without purification, verified by all three quality control methods. The crude product in NH_4OAc buffer (pH 5.5-6) was directly used for cell binding or preclinical PET imaging studies.

2.4. Competitive radiometric PS-binding assay

In order to examine the PS-binding potencies of the peptides, we developed a competitive radiometric binding assay using ^{64}Cu -*NOTA*-annexin V as radiotracer. We also wanted to observe any effects on PS binding caused by conjugation/labelling of the peptides, so we conducted this assay on the following peptides, labelling precursors and cold references: PGDLSR, LIKKPF, FBz-PGDLSR, FBz-LIKKPF, FBAM-C-PGDLSR, FBAM-C-LIKKPF, PSBP-6, FBz-PSBP-6, C-PSBP-6, *NOTA-PSBP-6*, Ga-*NOTA-*

PSBP-6, and Cu-NOTA-PSBP-6. We were unable to examine FBAM-C-PSBP-6 in this assay, as synthesis of this cold reference was unsuccessful. The day before the assay, 0.3-0.5 μg of PS (1,2-Dipalmitoyl-sn-glycero-3-phospho-L-serine sodium salt, Sigma-Aldrich) dissolved in 9:1 chloroform:methanol (further diluted in ethanol) was immobilized in each well of a BRANDplates® 96 well Strip Plate (Life Sciences). The plate was left at room temperature overnight to allow the solvent to evaporate, forming a light film. On the day of the experiment, the wells were washed twice with PBS to remove unbound PS. To reduce non-specific binding, 5% non-fat dry milk (Bio-Rad) in PBS was added to each well and left to incubate at room temperature for 2 h. The blocking buffer was removed and wells were washed twice with PBS.

Serial dilutions of each peptide/peptide conjugate (10^{-7} to 10^{-2} M) and unlabelled, wild-type annexin V as internal reference (10^{-11} to 10^{-6} M) were prepared using 2.5 mM Ca^{2+} binding buffer. Binding of ^{64}Cu -NOTA-annexin V to PS was determined in the presence of increasing concentrations of peptide/peptide conjugate and wild-type annexin V. 200 μL of each concentration of PS-binding peptide or cold annexin V was added to the wells in triplicate. 10 μL (10 KBq) of ^{64}Cu -NOTA-annexin V in PBS was added to each well, and the plate was left to incubate at room temperature for 2 h. After 2 h, the wells were washed twice with Ca^{2+} buffer to remove any unbound ligand, and the plate was broken apart into individual wells. Each well was placed into a scintillation vial, and bound activity was counted in a Wizard gamma counter. To determine maximum binding of the radiotracer for normalization, ^{64}Cu -NOTA-annexin V was added to wells that contained just PS and Ca^{2+} buffer (no competition). Nonspecific binding of ^{64}Cu -NOTA-annexin V was determined in wells that contained just Ca^{2+} buffer (no immobilized PS).

Data were analyzed as percent inhibition of ^{64}Cu -NOTA-annexin V binding. Concentrations for half-maximum inhibition (IC_{50}) were calculated from dose-response curves generated with GraphPad Prism® 5.0 software.

2.5. Cell culture

EL4 murine T-cell lymphoma cells (TIB-39™), which readily undergo apoptosis when introduced to cytotoxic agents, were purchased from the American Type Tissue Culture Center (ATCC) (Manassas, VA, USA) and maintained in RPMI 1640 medium (Gibco®) containing 20 mM HEPES, 10% fetal bovine serum (FBS) (Gibco®), 2 mM L-glutamine (Invitrogen) and 1% penicillin/streptomycin (Invitrogen). Cell density was maintained in the range of 2×10^5 cells/mL to 2×10^6 cells/mL, and cell growth medium was added or changed every other day. Cells were incubated at 37 °C in a humidified incubator with a 5% (v/v) CO_2 atmosphere (ThermoForma Series II Water Jacketed CO_2 Incubator).

2.6. Inducing apoptosis in EL4 cells

In order to evaluate the ability of each radioligand to bind to apoptotic cancer cells, an *in vitro* model of chemotherapy-induced apoptosis was used^{140,147,157}. (s)-(+)-camptothecin (Sigma-Aldrich), a DNA-topoisomerase I inhibitor, was used to induce apoptosis in EL4 cells. This *in vitro* model of cell death was used for subsequent cell binding assays.

2.7. Cell binding assay

22-24 h prior to the cell binding assay, two T75 flasks were prepared containing 15 mL of EL4 cells at a cell density of 1 million cells/mL. To one flask, 9 μ L of the stock solution of camptothecin (2.5 mM in 1 M NaOH) was added to the 15 mL of medium to produce a final camptothecin concentration of 1.5 μ M. To the control flask, 9 μ L of 1 M NaOH solution was added. To prevent direct contact of 1 M NaOH and 2.5 mM camptothecin with the cells, NaOH/camptothecin was first added to the medium, which was then added to the cells. Control and treated cells were then left to incubate for one day at 37°C.

2.7.1. Cell binding assay for ¹⁸F-labelled annexin V

On the day of experiment, control and treated cells were spun down, growth medium was removed, and cells were washed once with PBS, and once with 2.5 mM Ca²⁺-containing binding buffer. Cells were resuspended in binding buffer to 5 x 10⁶ cells/mL. Using two 12-well plates (one for control cells and one for treated cells), 300 μ L of cell solution was added to each well. The ¹⁸F-labelled annexin V tracer being investigated was diluted in binding buffer to 0.5 kBq/ μ L, and 200 μ L of this ¹⁸F-annexin V solution was added to each well in order to get approximately 0.1 MBq/well. Cells were left to incubate at room temperature for 1, 15, 30 or 60 min. At each time point, the cells were transferred to an eppendorf tube, rinsing the well with an additional 500 μ L of binding buffer and adding this to the tube. Cells were spun down to form a cell pellet. The supernatant was removed along with any unbound tracer. The pellet was resuspended/washed in 500 μ L of binding buffer, and this solution was transferred to a

new eppendorf in order to remove unbound tracer that was non-specifically stuck to the eppendorf tube. Cells were again spun down to get a pellet, and the supernatant removed. The amount of ^{18}F -annexin V bound to the cells was then measured by a Wizard gamma counter. Calculated uptake values were expressed as percentage of total activity normalized to amount (in mg) of cellular protein content. Monica Wang assisted with optimization of this cell binding assay procedure. In order to acknowledge the effect of Ca^{2+} concentration on ^{18}F -labelled annexin V binding to apoptotic cells, another set of cell binding assays were carried out using a lower Ca^{2+} concentration, 1.25 mM, which is suggested to be more representative of physiological Ca^{2+} levels¹⁵⁸.

To determine protein content, cells (control and treated) were lysed with CellLytic™ (200 μL) for 10 min at 4 °C, centrifuged at 4 °C at 10000 rpm for 8 min, and left in the freezer for at least one night. The lysate was then thawed and protein content was analyzed by a BCA protein assay.

2.7.2. Cell binding assay for radiopeptides

On the day of experiment, control and treated cells were spun down, growth medium was removed, and cells were washed once with PBS, and once with binding buffer. In order to ensure that radiopeptide binding to PS was Ca^{2+} -independent, two sets of binding assays were conducted: one set of binding assays were performed in Ca^{2+} -negative binding buffer, and another set were performed in Ca^{2+} -positive (2.5 mM CaCl_2) binding buffer. Cells were resuspended in their respective binding buffer to 5×10^6 cells/mL. 300 μL of the cell suspensions were aliquoted into LoBind eppendorf tubes. 200 μL (~0.1 MBq) of radiopeptide diluted in the desired binding buffer was added to

each eppendorf, incubating for 1, 15, 30 and 60 min. Binding was terminated at each time point by centrifuging the cells at 1500 rpm for 2 min. Most of the supernatant was removed by aspiration (~50 μ L left behind), the tubes were spun down again (1500 rpm for 2 min), and the rest of the supernatant was removed with a pipette. The amount of radiopeptide bound to the cell pellets was measured by a Wizard gamma counter.

To determine protein content, cells (control and treated) were lysed with CellLytic™ (200 μ L) for 10 min at 4 °C, centrifuged at 4 °C at 10000 rpm for 8 min, and left in the freezer for at least one night. The lysate was then thawed and protein content was analyzed by a BCA protein assay.

2.8. Flow cytometry

2.8.1. Flow cytometry using FITC-annexin V

In order to determine the optimal concentration of camptothecin to induce sufficient apoptosis in EL4 cells, flow cytometry was used to evaluate apoptosis levels in EL4 cells treated with increasing doses of the drug. The FITC Annexin V Apoptosis Detection Kit 1 (BD Pharmingen™) was used to detect apoptotic cells. From this kit, fluorescein isothiocyanate conjugated annexin V (FITC-annexin V), which binds to PS, was used to stain apoptotic cells. Propidium iodide (PI), a membrane impermeant nucleic acid stain, was used to stain cells that had lost their membrane integrity (necrotic/late apoptotic cells). The use of PI allowed for discrimination between early apoptotic and late apoptotic/necrotic cells. A 6-well plate was prepared with 3 mL of RPMI medium containing 3 million cells (cell density of 1 million cells/mL) in each well. Each well had

a different concentration of camptothecin: 0.5 μM , 1.0 μM , 1.5 μM , and 2.0 μM , and the control well contained just NaOH without camptothecin. The cells were left to incubate for 22-24 h at 37 $^{\circ}\text{C}$. The next day, the cells were centrifuged, washed twice with PBS, and resuspended in Ca^{2+} -containing binding buffer (BD Pharmingen™) to a cell density of 1 million cells/mL. 100 μL of each cell solution was transferred to its own flow cytometry tube. To each tube, 3 μL of FITC-annexin V and 3 μL of PI were added. The tubes were gently shaken and left to incubate in the dark for 15 min at room temperature. 400 μL of binding buffer was then added to each tube, and apoptotic and necrotic cells in each tube were counted by a fluorescence activated cell sorter.

2.8.2. Flow cytometry using FITC-PSBP-6

Flow cytometry was also used to examine the ability of FITC-PSBP-6, a fluorescent PS-binding peptide, to bind to apoptotic cells. EL4 cells were treated with 1.5 μM camptothecin for 22-24 h. A fresh stock solution of 50-100 μM of FITC-PSBP-6 was prepared on the day of the experiment by dissolving the lyophilized peptide in DMSO and then diluting it in deionized water to achieve < 1% DMSO. PI from the FITC Annexin V Apoptosis Detection Kit 1 (BD Pharmingen™) was also used to stain the cells in order to discriminate between apoptotic and necrotic/late apoptotic cells. Cells were washed once with PBS and once with Ca^{2+} -negative binding buffer (prepared in-house), then resuspended in Ca^{2+} -negative binding buffer to 1 million cells/mL. 200 μL of cell solution (treated or control) was transferred to its own flow cytometry tube. To each tube, 1 μM (final concentration) of FITC-PSBP-6 and 30 μL of PI from the BD Pharmingen kit were added. The tubes were left to incubate in the dark for approximately 30 min at room

temperature. 300 μL of binding buffer was then added to each tube, and stained cells in each tube were counted by a fluorescence activated cell sorter.

2.9. Fluorescence confocal microscopy

2.9.1. Fluorescence confocal microscopy using FITC-annexin V

Fluorescence confocal microscopy was used to image the apoptosis-inducing effect of camptothecin on EL4 lymphoma cells. Only two groups of cells were imaged by fluorescence confocal microscopy: control (untreated) cells, and cells treated with 1.5 μM camptothecin, the optimal concentration to produce sufficient apoptosis levels determined by flow cytometry. These cells were prepared and treated using the same method that was used in the flow cytometry studies, one day prior to fluorescence imaging. Like the fluorescence staining done in the flow cytometry studies, FITC-annexin V and PI were used to detect apoptotic cells and necrotic cells, respectively. After 1 day of treatment, cells were spun down, washed once in PBS and once in binding buffer, and then resuspended in binding buffer to a cell density of 2×10^5 cells/mL. 30 μL of FITC-annexin V and 30 μL of PI were added to 500 μL of this cell solution, and the cells were incubated in the dark at room temperature for 15 min. Cells were then spun down and resuspended in 1 mL binding buffer, and 500 μL of each cell solution was added to its own well of a Nunc™ Lab-Tek™ II Chambered Coverglass System. The cells were then viewed and imaged under a Zeiss confocal microscope available in the Cell Imaging Facility of the Cross Cancer Institute (Edmonton, Alberta).

2.9.2. Fluorescence confocal microscopy using FITC-PSBP-6

In order to visualize binding of FITC-PSBP-6 to EL4 cells undergoing cell death, confocal microscopy was used. In addition to FITC-PSBP-6, NucView™ 405 Caspase-3 Substrate (Biotium) was used as an additional apoptosis detecting agent. This caspase probe is a fluorogenic DNA dye coupled to a caspase-3/7 DEVD recognition sequence that is cleaved by activated caspases in apoptotic cells to release the DNA dye, which accumulates in apoptotic cells. PI from the FITC Annexin V Apoptosis Detection Kit 1 (BD Pharmingen™) was also used to stain cells with non-intact membranes (late apoptotic/dead/necrotic cells). EL4 cells were treated with 1.5 μM of camptothecin for 22-24 h following the same procedure as outlined above. Cells were washed once with PBS and once with Ca^{2+} -negative binding buffer, then resuspended in Ca^{2+} -negative binding buffer to 1 million cells/mL. 200,000 cells were added to a LoBind eppendorf tube and centrifuged at 3000 rpm for 2 min. The supernatant was carefully removed, and a 500 μL solution containing 1 μM FITC-PSBP-6, 1 μM of NucView™ 405 Caspase-3 Substrate and 60 μL of PI from the BD Pharmingen kit in deionized water was used to resuspend the cell pellet. The cells were left to incubate at room temperature in the dark for approximately 30 min. The cells were then centrifuged, washed once with Ca^{2+} -negative binding buffer, and resuspended in 1 mL of Ca^{2+} -negative binding buffer. 500 μL of this solution was added to the well of a Nunc™ Lab-Tek™ II Chambered Coverglass System. The cells were then imaged under a Zeiss confocal microscope.

2.10. EL4 lymphoma mouse tumour model

All animal experiments were carried out in accordance with guidelines of the Canadian Council on Animal Care and were approved by the local Animal Ethics Committee of the Cross Cancer Institute. Animals were handled by Dr. Melinda Wuest and Monica Wang. The EL4 lymphoma tumour model in C57/BL6 mice has been established previously in order to evaluate molecular probes targeting tumour apoptosis *in vivo*⁶⁸. EL4 cells (1×10^6) were injected subcutaneously into the left flank of wild-type female C57/BL6 mice. 7-10 days after injection, mouse tumours were measured to be about 12-14 mm long and 7-10 mm wide (weighing approximately 500 mg), suitable for chemotherapy treatment and subsequent PET imaging. Apoptosis in these tumours was induced by intraperitoneal injection of cyclophosphamide (100 mg/kg) and etoposide (76 mg/kg) in 50% DMSO/saline (total injected volume 100-200 μ L) for either one day (for radiopeptide imaging studies) or two consecutive days (for ¹⁸F-annexin V imaging studies). After 2 consecutive days of this treatment, mice lost > 2 g of weight and tumours shrank to about half of their original size.

2.11. Dynamic PET imaging

EL4 tumour-bearing C57/BL6 mice were used for PET imaging experiments, which were performed by Dr. Melinda Wuest. Tumour uptake of radiotracer (¹⁸F-annexin V or ⁶⁴Cu-NOTA-PSBP-6) was evaluated in both control (untreated) mice and mice treated with the apoptosis-inducing mixture of cyclophosphamide and etoposide. The animals were anesthetized through inhalation of isoflurane in 40% oxygen/60% nitrogen (gas flow, 1 L/min), and body temperature was maintained at 37 °C. Mice were

immobilized in the prone position and placed in the center of the field of view of the Inveon® PET scanner (Siemens Preclinical Solutions, Knoxville, TN, USA). The amount of radioactivity present in the injection solution in a 0.5 mL syringe was determined with a dose calibrator, which was cross-calibrated with the scanner. The emission scan of a 60 min dynamic PET acquisition was started. After a delay of approximately 15 s, 5-8 MBq of the radiotracer of interest diluted in 70-130 µL sterile saline (0.9%) or 100 mM NH₄OAc buffer (pH 6) was injected through a tail vein catheter. Data acquisition continued for 60 min in 3D list mode. The list mode data were sorted into sinograms with 54 time frames (10×2, 8×5, 6×10, 6×20, 8×60, 10×120 and 6×300 s). The frames were reconstructed using maximum a posteriori (MAP) reconstruction mode. The pixel size was 0.085×0.085×0.12 cm, and the resolution in the centre field of view was 1.8 mm. No correction for partial volume effects was performed. The image files were further processed using the ROVER v2.0.21 software (ABX GmbH, Radeberg, Germany). Masks for defining 3D regions of interest (ROI) were set and the ROIs were defined by 50% thresholding. ROI time-activity curves (TAC) were generated for subsequent data analysis. Standardized uptake values [SUV = (activity/mL tissue)/ (injected activity/body weight), mL/g] were calculated for each ROI. Dr. Melinda Wuest provided all PET images and time-activity curves (TACs) for the preclinical PET studies, and contributed to data interpretation.

2.12. Determination of radiopeptide lipophilicity

To determine the lipophilicity of radiopeptides, the shake-flask method¹⁵⁹ was used. The partition coefficients of the radiopeptides were determined using n-octanol as

organic phase and PBS (pH 7.4) as aqueous phase. 500 μ L of each phase were added to a LoBind eppendorf tube, to which > 1 MBq of radiopeptide was added, and the mixture was shaken vigorously for 5 min. The mixture was then centrifuged at 2000 rpm for 2 min to allow the layers to separate. Aliquots of 100 μ L were removed from each phase and the amount of radiopeptide present in each phase was measured by a Wizard gamma counter. Experiments were performed in triplicate, and $\log D_{7.4}$ values were calculated.

2.13. Determination of blood distribution and metabolic stability in vivo

3-30 MBq of radiopeptide in 100–150 μ L of 10% propylene glycol in sterile saline (0.9%) or 100 mM NH_4OAc buffer (pH 6) was injected as a bolus through a catheter into the tail vein of isoflurane anaesthetised BALB/c mice. Before radiopeptide injection, mice were heparinised by subcutaneous injection of 50 μ L heparin (1000 I.U.) and kept under anaesthesia during the course of the experiment. At selected time points of 5, 15, 30 and 60 min, tail vein samples (approximately 20-50 μ L) were collected through the catheter. Blood cells were separated by immediate centrifugation (5 min at 13,000 rpm). Proteins within the plasma samples were precipitated by adding 100-200 μ L methanol to the supernatant following a second centrifugation step (5 min at 13,000 rpm). Dr. Melinda Wuest prepared the mice, collected the blood samples and separated the blood components, which were then handed off to me. To determine the distribution of radiopeptide in the blood cells, protein and plasma, radioactivity present in each compartment was measured using a gamma counter. To analyze plasma samples for radiometabolites and original radiopeptide, the supernatant plasma fractions from each time point were analyzed by analytical HPLC.

2.14. Data analysis

All data are expressed as means \pm standard error of the mean (SEM) from three or more experiments. All graphs were constructed using GraphPad Prism 5.0 (GraphPad Software, San Diego, CA, USA). IC₅₀ values were calculated using a nonlinear regression (curve fit) analysis (GraphPad Prism 5.0). Statistical differences were considered significant if $p < 0.05$, and were tested using the Student's t-test.

3. RESULTS

3.1. Labelling wild-type annexin V with ^{18}F for PET imaging of cell death

3.1.1. Radiolabelling annexin V with ^{18}F -containing prosthetic groups

Random labelling of the 23 primary amine groups accessible on wild-type annexin V was achieved via an acylation reaction with prosthetic group [^{18}F]SFB. The reaction product [^{18}F]SFB-annexin V was synthesized in decay-corrected radiochemical yields of $9 \pm 1\%$ (based upon [^{18}F]SFB). Site-specific labelling of Cys315 in wild-type annexin V was achieved by an alkylation reaction with [^{18}F]FBEM to make [^{18}F]FBEM-annexin V in decay-corrected radiochemical yields of $4 \pm 2\%$ (based upon [^{18}F]FBEM). Both prosthetic groups were purified by HPLC prior to the reaction with wild-type annexin V. The synthesis route of randomly labelled and site-specifically labelled ^{18}F -annexin V is represented in figure 7.

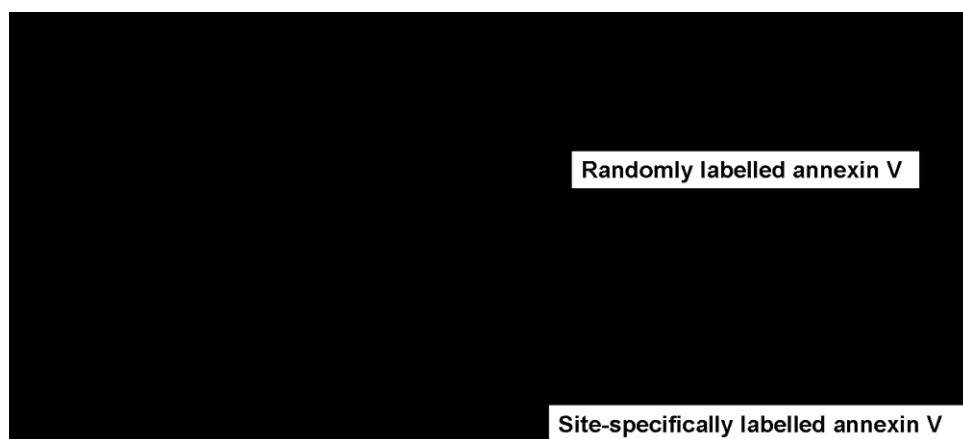


Figure 7. Random and site-specific labelling of annexin V with [^{18}F]SFB and [^{18}F]FBEM.

Both ^{18}F -labelled annexin V derivatives were obtained at high radiochemical purity (RCP) ($> 95\%$) after purification with SEC. Figure 8 shows the results of Coomassie-stained SDS-PAGE and radio-SDS-PAGE analyses of purified ^{18}F -labelled annexin V derivatives, with unlabelled wild-type annexin V as reference. Conjugation of prosthetic groups [^{18}F]SFB and [^{18}F]FBEM to wild-type annexin V proceeded under mild condition (PBS, pH 7.4, 30 min, 30 °C), and no degradation was observed during the radiosynthesis of ^{18}F -labelled annexin V as confirmed by SDS-PAGE analysis. Isolated radiolabelled protein corresponds with the expected molecular weight of wild-type annexin V derivatives of 36 kDa.

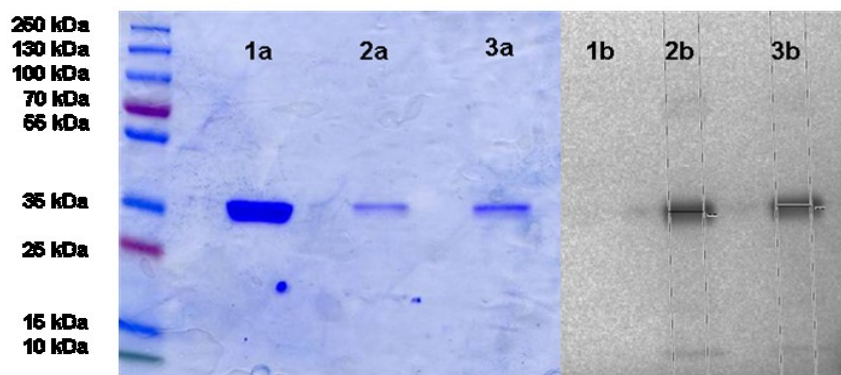


Figure 8. Quality control of ^{18}F -labelled annexin V. Stained SDS-PAGE gel (left) and corresponding radio-SDS-page analysis (right) of wild-type annexin V (lanes 1a and 1b), purified randomly labelled annexin V ([^{18}F]SFB-annexin V) (lanes 2a and 2b), and purified site-specifically labelled annexin V ([^{18}F]FBEM-annexin V) (lanes 3a and 3b).

3.1.2. *In vitro* evaluation of ^{18}F -labelled annexin V

3.1.2.1. Inducing apoptosis in EL4 cells using camptothecin

Results from the flow cytometry studies done to assess the effect of camptothecin concentration on the level of apoptosis induced in EL4 cells are provided in Figure 9.

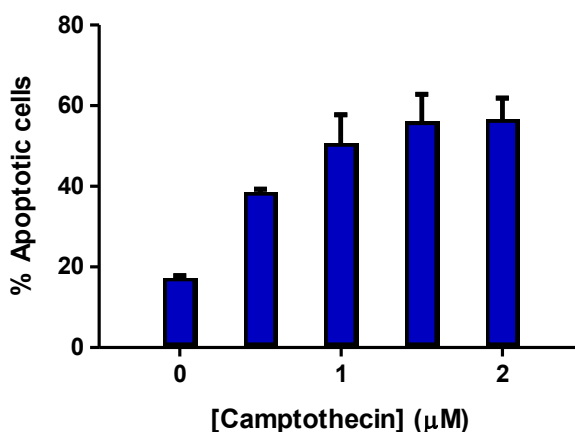


Figure 9. Flow cytometric analysis of EL4 cells undergoing camptothecin-induced apoptosis using FITC-annexin V as fluorescent stain. Proportions of EL4 cells undergoing apoptosis were measured as a function of camptothecin concentration ($n = 3$).

These data show a small amount of basal cell death (17%) in the untreated (control) cell population due to the unstable nature of the cell line. This baseline level of cell death in EL4 cells has been previously reported¹⁰⁰. Treatment with 1.5 μM of camptothecin induced the highest increase in total (early and late) apoptosis (as well as other PS-exposing cell death modes) relative to untreated cells, as 56% of the cells were stained with FITC-annexin V. Apoptosis levels did not significantly increase when camptothecin concentration was increased to 2.0 μM , which induced a similar apoptosis rate of 57%. Based on these results, we selected a drug concentration of 1.5 μM to induce cell death in

EL4 cells for the cell binding assay. Confocal microscopy images of camptothecin-treated EL4 cells stained with FITC-labelled annexin V and PI are shown in figure 10. These fluorescence confocal microscopy images confirm the successful induction of cell death in EL4 cells upon treatment with 1.5 μM of camptothecin as shown by the green stain from FITC-annexin V binding to PS in the treated cell population.

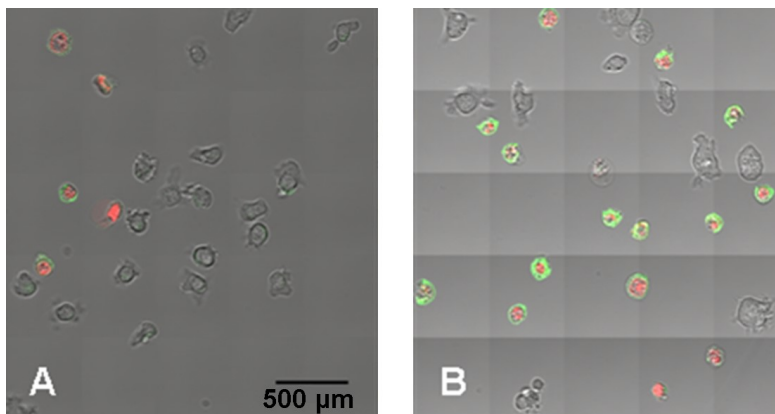


Figure 10. Fluorescence confocal microscopy images of apoptotic EL4 cells stained with FITC-annexin V and PI. (A) Control (untreated) EL4 cell population; (B) EL4 cell population treated with 1.5 μM camptothecin for 22-24 h. Green stain: FITC-annexin V (early apoptosis); red stain: PI (late apoptosis/necrosis).

3.1.2.2. Cell binding assay using [^{18}F]SFB-annexin V and [^{18}F]FBEM-annexin V

Cell binding results showed significantly higher binding of ^{18}F -labelled annexin V derivatives to EL4 mouse lymphoma cells treated with the apoptosis-inducing agent camptothecin compared to untreated cells over time. This finding was comparable for randomly labelled [^{18}F]SFB-annexin V and site-specifically labelled [^{18}F]FBEM-annexin V. After 60 min, a four-fold higher uptake of [^{18}F]SFB-annexin V to treated EL4 cells was found compared to non-treated cells (Figure 11).

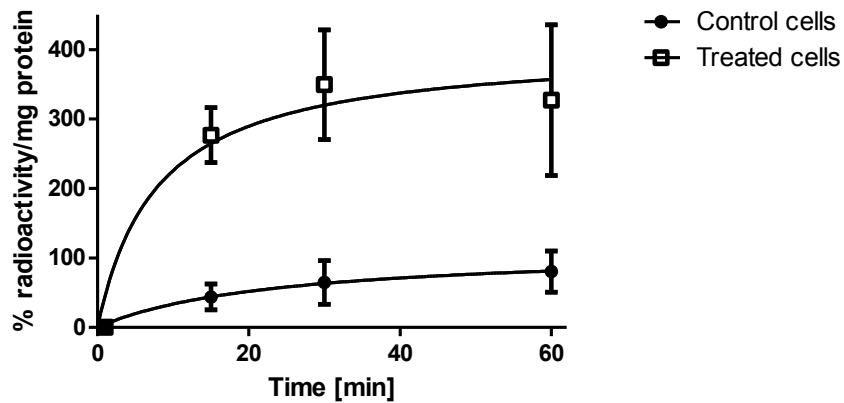


Figure 11. EL4 cell binding of [¹⁸F]SFB-annexin V. Cell binding of randomly-labelled [¹⁸F]SFB-annexin V was measured in untreated (control) EL4 cells and EL4 cells treated for 22-24 hours with 1.5 μ M camptothecin (n = 3).

Ionized calcium is known to be vital for PS binding of annexin V. Although most annexin V binding assays are carried out in 2.5 mM Ca^{2+} , Tait and colleagues found that annexin V binding to PS declines rapidly over a range of 2.5-1.25 mM¹⁶⁰. To address this issue, we conducted another set of cell binding studies using a Ca^{2+} concentration of 1.25 mM, which is suggested to be representative of Ca^{2+} levels in vivo¹³⁰. The results from these binding studies are shown in figures 12 and 13. As expected, binding of [¹⁸F]SFB-annexin V to both control (untreated) EL4 cells (figure 12) and cells treated with 1.5 μ M camptothecin (Figure 13) was significantly decreased by reducing the Ca^{2+} concentration from 2.5 mM to 1.25 mM. However, the lower Ca^{2+} concentration did not diminish the preferential binding of [¹⁸F]SFB-annexin V to cells treated with camptothecin compared to untreated cells. After 60 min, binding of the radioligand was still three times higher in treated cells versus control cells.

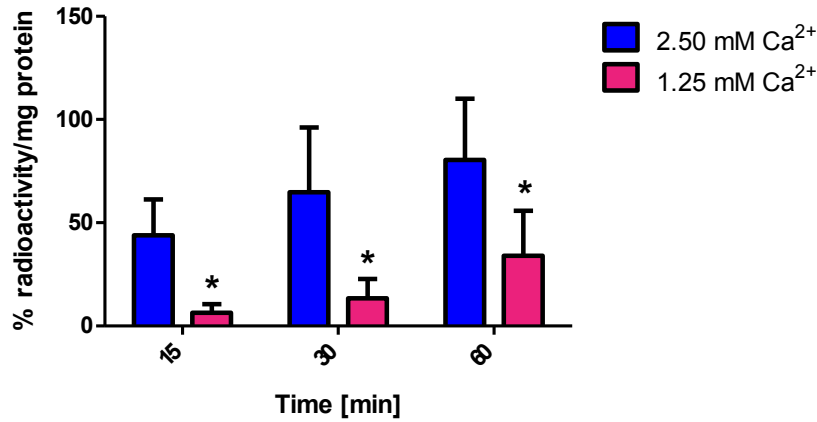


Figure 12. Effect of Ca²⁺ concentration on control EL4 cell binding of [¹⁸F]SFB-annexin V. Comparison of cell binding of [¹⁸F]SFB-annexin V to untreated EL4 cells in the presence of higher (2.5 mM) and lower (1.25 mM) concentrations of Ca²⁺ (n = 3).

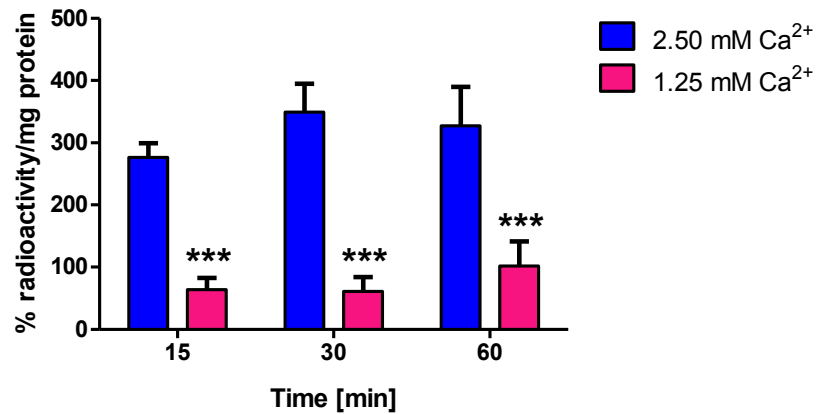


Figure 13. Effect of Ca²⁺ concentration on camptothecin-treated EL4 cell binding of [¹⁸F]SFB-annexin V. Comparison of cell binding of [¹⁸F]SFB-annexin V to EL4 cells treated for 22-24 h with 1.5 μM camptothecin in the presence of higher (2.5 mM) and lower (1.25 mM) concentrations of Ca²⁺ (n = 3).

When using site-selectively labelled [^{18}F]FBEM-annexin V, we observed a 2.6-fold increase in binding of the radioligand to treated EL4 cells compared to untreated cells (Figure 14).

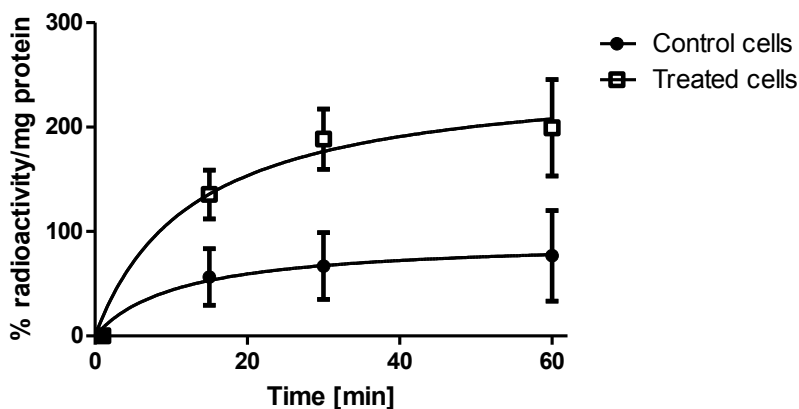


Figure 14. EL4 cell binding of [^{18}F]FBEM-annexin V. Cell binding of site-specifically labelled [^{18}F]FBEM-annexin V was measured in untreated (control) EL4 cells and EL4 cells treated for 22-24 hours with 1.5 μM camptothecin ($n = 3$).

These results confirm that both randomly labelled [^{18}F]SFB-annexin V and site-selectively labelled [^{18}F]FBEM-annexin V retained the ability to detect cell death *in vitro*. Both radiotracers demonstrated significantly higher binding to EL4 cells treated with 1.5 μM camptothecin compared to untreated cells. Binding kinetics were comparable between [^{18}F]SFB-annexin V and [^{18}F]FBEM-annexin V, and no significant differences in the extent of binding to EL4 cells undergoing cell death were observed between the two ^{18}F -labelled wild-type annexin V derivatives. This result suggests that random and site-selective methods for radiolabelling wild-type annexin V can provide radiotracers with comparable PS binding abilities.

3.1.3. Preclinical PET imaging of apoptosis using ¹⁸F-labelled annexin V

After confirming the ability of [¹⁸F]SFB-annexin V and [¹⁸F]FBEM-annexin V to detect chemotherapy-induced cell death *in vitro*, we next wanted to examine the ability of ¹⁸F-labelled annexin V to detect chemotherapy-induced cell death in tumours *in vivo*. Since we found no significant difference in PS-binding ability between randomly and site-specifically labelled ¹⁸F-annexin V, we used randomly labelled [¹⁸F]SFB-annexin V for our preclinical PET imaging studies due to the simpler, faster radiolabelling and better yields. The tumour uptake profile of ¹⁸F-annexin V was studied in EL4 tumour-bearing C57Bl6 mice treated with a chemotherapeutic mixture of 100 mg/kg cyclophosphamide + 76 mg/kg etoposide for 2 consecutive days, using untreated EL4 tumour-bearing mice as controls. A baseline tumour uptake of ¹⁸F-annexin V was observed in control (untreated) mice, shown in figure 15.

¹⁸F-annexin V was rapidly taken up into control EL4 tumours, where it remained trapped with no washout. At 10 min p.i., the control tumours had an SUV of 0.77, and no change in tumour uptake was observed over time (at 60 min p.i., control tumour SUV = 0.80). This is shown in the TACs provided in figure 16. The blood clearance TAC of ¹⁸F-annexin V shows that after 60 minutes, blood radioactivity was still higher than radioactivity in the EL4 tumours.

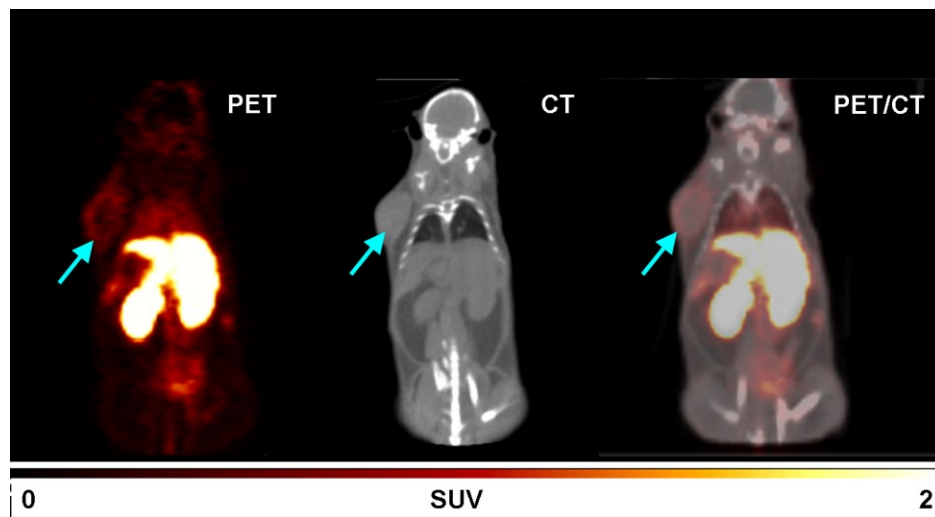


Figure 15. Preclinical PET/CT images of EL4 tumour uptake of ^{18}F -labelled annexin V in a control (untreated) mouse. Representative coronal PET, CT and fused PET/CT images were obtained from an EL4 tumor-bearing control (untreated) C57BL6 mouse 90 min after administration of 4–5 MBq of ^{18}F]SFB-annexin V. Blue arrows indicate tumours. Specific activity of ^{18}F]SFB-annexin V used for imaging was determined to be 3.4 ± 0.8 Ci/g.

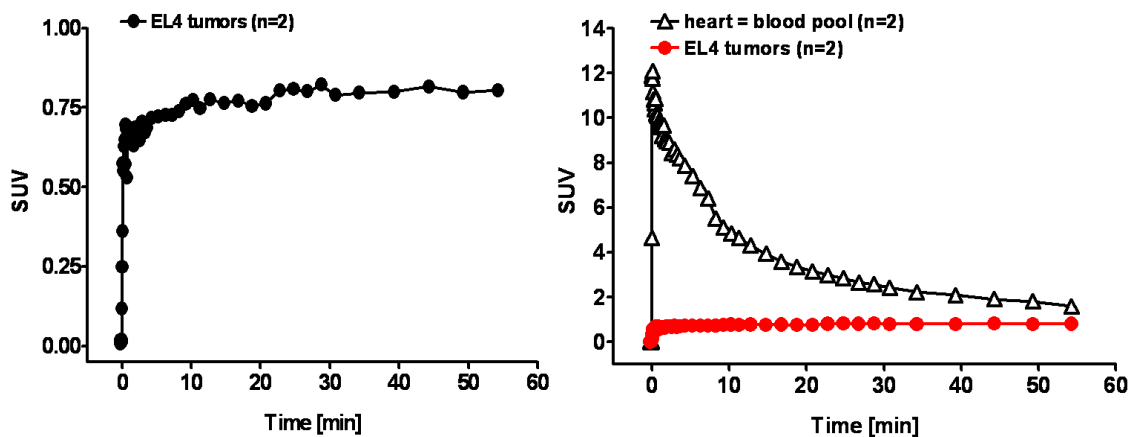


Figure 16. TACs of the blood clearance profile and radioactivity profile in control (untreated) EL4 tumours in mice injected with ^{18}F -labelled annexin V. Radioactivity profile of ^{18}F]SFB-annexin V in EL4 tumours in control (untreated) C57BL6 mice over time (left); Radioactivity profile of ^{18}F]SFB-annexin V in heart vs. EL4 tumour in control C57BL6 mice over time (right).

Although a baseline uptake of ^{18}F -annexin V was observed in control mice, we failed to see an increase in tumour uptake in mice treated for 2 consecutive days with cyclophosphamide and etoposide (figure 17). In fact, tumour SUVs were lower in treated mice compared to control mice, which might be explained by the decrease in overall tumour volume over the 2 days of treatment.

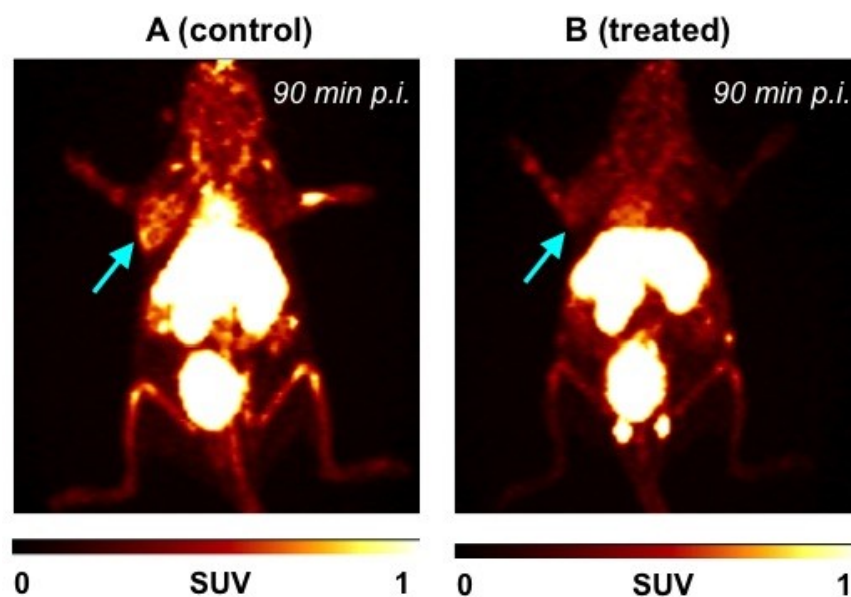


Figure 17. Preclinical PET images of EL4 tumour response to treatment with cyclophosphamide and etoposide using ^{18}F -labelled annexin V as radiotracer. Representative maximum intensity projections (MIPs) were obtained from A) control (untreated) EL4 tumour-bearing C57Bl6 mice and B) EL4 tumour-bearing C57Bl6 mice treated with 100 mg/kg cyclophosphamide + 76 mg/kg etoposide for 2 consecutive days. Imaging was done 24 h after the second drug injection (48 h after first drug injection). Images were taken 90 min after administration of 4–5 MBq of ^{18}F -annexin V. Blue arrows indicate tumours. Specific activity of [^{18}F]SFB-annexin V used for imaging was determined to be 3.4 ± 0.8 Ci/g.

Previous studies have found that the optimal time window for imaging apoptosis occurs before decreases in tumour size become visible¹²⁷. Since obvious tumour shrinkage occurred over 2 consecutive days of treatment with cyclophosphamide and

etoposide, we tried imaging the mice at earlier time points post treatment, and these mice received just one treatment instead of two. The mice were imaged 4, 12, and 24 h after injection of the drug mixture. Although higher tumour SUVs were obtained for these earlier time points compared to the 48 h time point (likely due to smaller decreases in overall tumour volume), treated tumours did not show higher uptake of ^{18}F -annexin V compared to control tumours at any time point post treatment (figure 18).

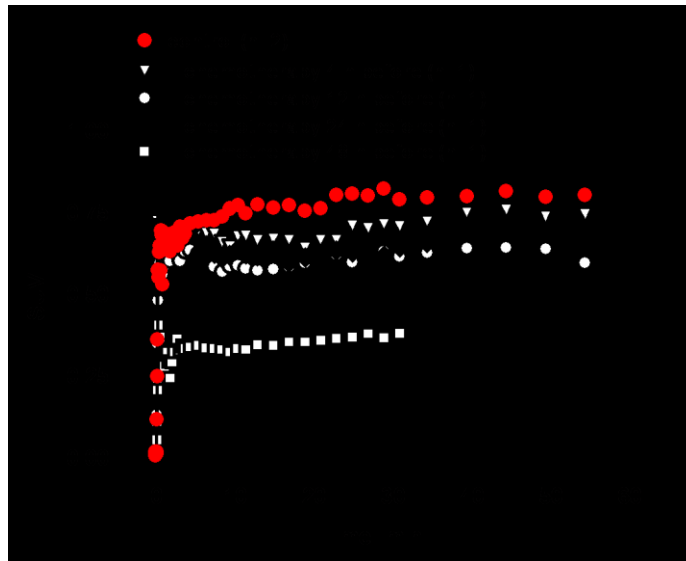


Figure 18. Effect of treatment with cyclophosphamide and etoposide on EL4 tumour uptake of ^{18}F -labelled annexin V in C57Bl6 mice. TACs were generated by measuring uptake of [^{18}F]SFB-annexin V into EL4 tumours of control (untreated) C57Bl6 mice as well as C57Bl6 mice treated with a chemotherapeutic mixture of 100 mg/kg cyclophosphamide and 76 mg/kg etoposide. Treated mice were imaged 4, 12, 24 and 48 h after initiation of treatment.

3.2. Evaluation of radiolabelled PS-binding peptides for PET imaging of apoptosis

3.2.1. Competitive radiometric PS binding assay to determine binding potency

Binding of ^{64}Cu -NOTA-annexin V to PS was challenged with different concentrations of peptides PGDLSR, LIKKPF, FBz-PGDLSR, FBz-LIKKPF, FBAM-C-PGDLSR, FBAM-C-LIKKPF, PSBP-6, FBz-PSBP-6, C-PSBP-6, NOTA-PSBP-6, Ga-NOTA-PSBP-6, and Cu-NOTA-PSBP-6, as well as wild-type annexin V, which was used as an internal reference. We were unable to examine FBAM-C-PSBP-6 in this assay, as synthesis of this cold reference was unsuccessful. Figures 19, 20 and 21 summarize the results from the competitive radiometric PS binding assay. PGDLSR, LIKKPF, FBz-PGDLSR, FBz-LIKKPF, FBAM-CPGDLSR, and FBAM-CLIKKPF all gave comparable IC_{50} values in the low millimolar range (1 to 15 mM), whereas the IC_{50} for wild-type annexin V was determined to be 51 nM in the assay. Hexapeptides PGDLSR and LIKKPF showed lowest PS inhibition as expressed by IC_{50} values of 10 mM and 15 mM, respectively. Introduction of the 4-fluorobenzoyl (FBz) group into peptides LIKKPF and PGDLSR, as well as the attachment of FBAM to CPGDLSR and CLIKKPF resulted in slightly better inhibitory potencies: $\text{IC}_{50}(\text{FBz-PGDLSR}) = 7 \text{ mM}$; $\text{IC}_{50}(\text{FBz-LIKKPF}) = 4 \text{ mM}$; $\text{IC}_{50}(\text{FBAM-CPGDLSR}) = 6 \text{ mM}$; $\text{IC}_{50}(\text{FBAM-CLIKKPF}) = 1 \text{ mM}$. However, all hexapeptides and hexapeptide derivatives were about four orders of magnitude less potent than annexin V in the assay (figure 19).

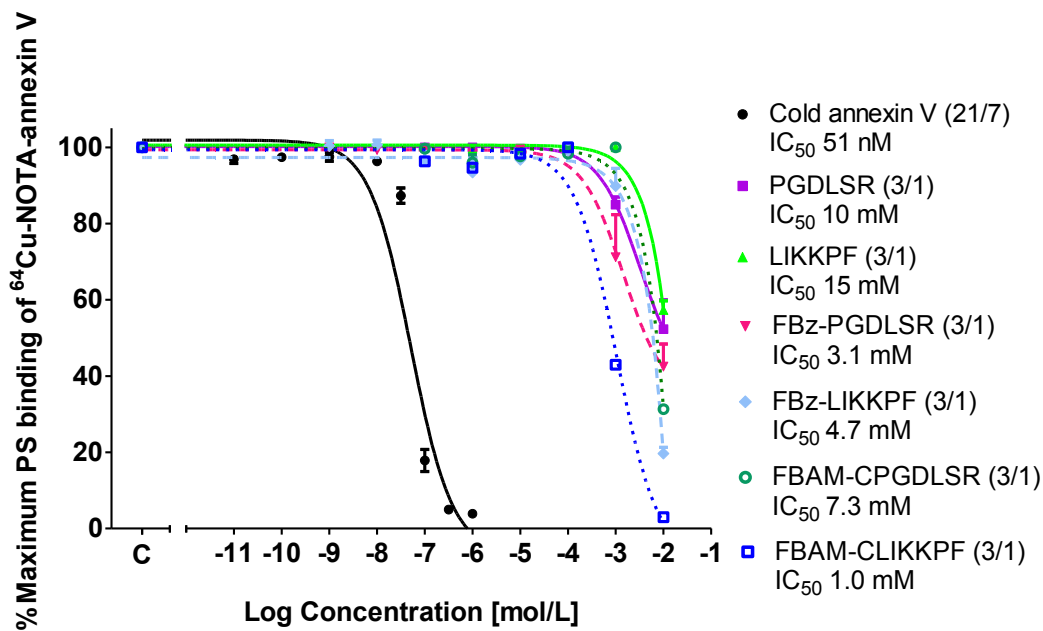


Figure 19. Inhibitory binding effect of unmodified and modified hexapeptides on PS binding of ^{64}Cu -NOTA-annexin V. IC_{50} values are given as mean values from n single data values out of x experiments (n/x).

Though still much less potent than the internal reference annexin V, 14-mer PSBP-6 and derivatives of PSBP-6 showed higher inhibitory potency than the hexapeptide derivatives, with IC_{50} values ranging from 6.4 μM to 0.6 mM (figures 20 and 21). Conjugation of PSBP-6 with FBz and NOTA groups increased its inhibitory potency by one order of magnitude, from 0.6 mM to 69 μM and 30 μM , respectively. Further complexation of Ga^{3+} and Cu^{2+} to NOTA-PSBP-6 did not drastically alter its potency: $\text{IC}_{50}(\text{Ga-NOTA-PSBP-6}) = 33 \mu\text{M}$; $\text{IC}_{50}(\text{Cu-NOTA-PSBP-6}) = 23 \mu\text{M}$. Modification of PSBP-6 with a terminal cysteine residue produced the highest inhibitory potency of 6.4 μM .

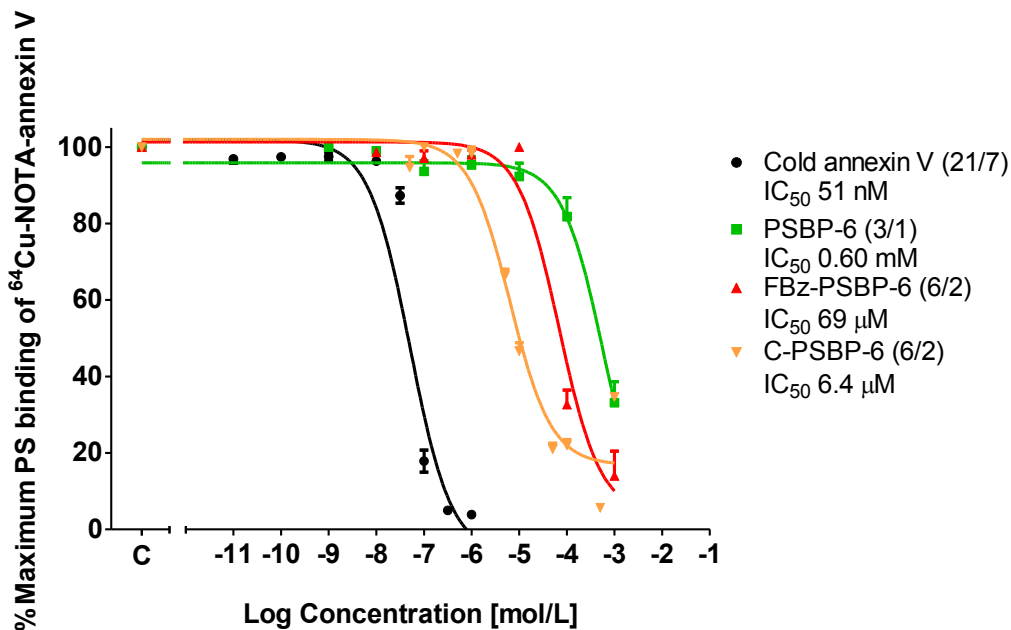


Figure 20. Inhibitory binding effect of unmodified, cysteine-tagged and fluorobenzoylated PSBP-6 on PS binding of ⁶⁴Cu-NOTA-annexin V. IC₅₀ values are given as mean values from n single data values out of x experiments (n/x).

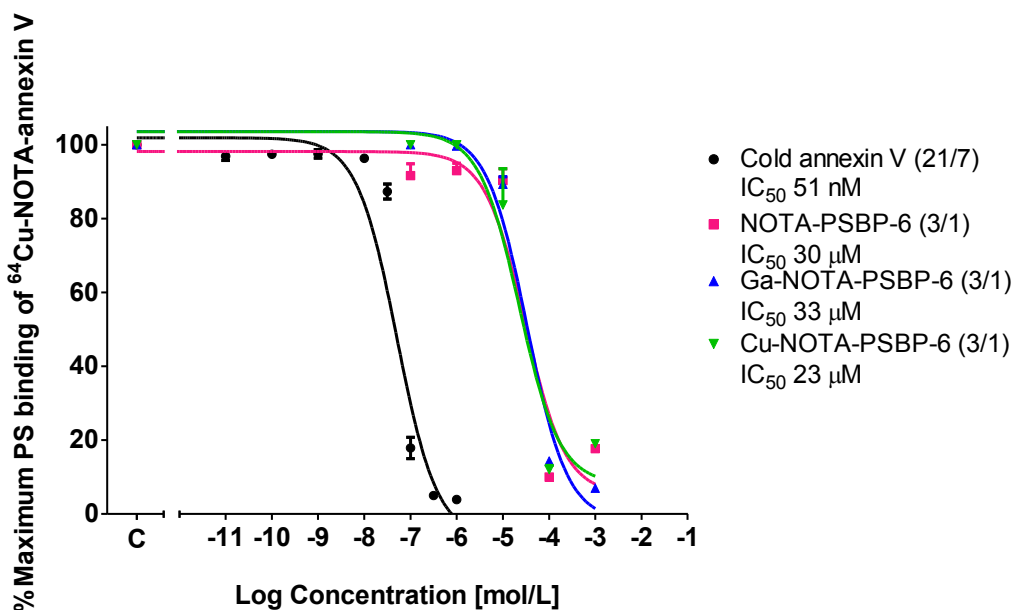


Figure 21. Inhibitory binding effect of NOTA-conjugated PSBP-6 coordinated with cold Ga³⁺ or Cu²⁺ on PS binding of ⁶⁴Cu-NOTA-annexin V. IC₅₀ values are given as mean values from n single data values out of x experiments (n/x).

3.2.2. Labelling PS-binding peptides with ^{18}F

3.2.2.1. Labelling PGDLSR with ^{18}F

Hexapeptide PGDLSR was labelled with [^{18}F]SFB in solution via an acylation reaction with its terminal amino group, giving [^{18}F]FB-PGDLSR in decay-corrected radiochemical yields of $36 \pm 8\%$ (based upon [^{18}F]SFB) with radiochemical purities of greater than 95%. The $\log D_{7.4}$ value of this radiopeptide was determined to be -1.6 ± 0.2 ($n = 3$). The reaction scheme for radiolabelling PGDLSR with [^{18}F]SFB is given in figure 22.

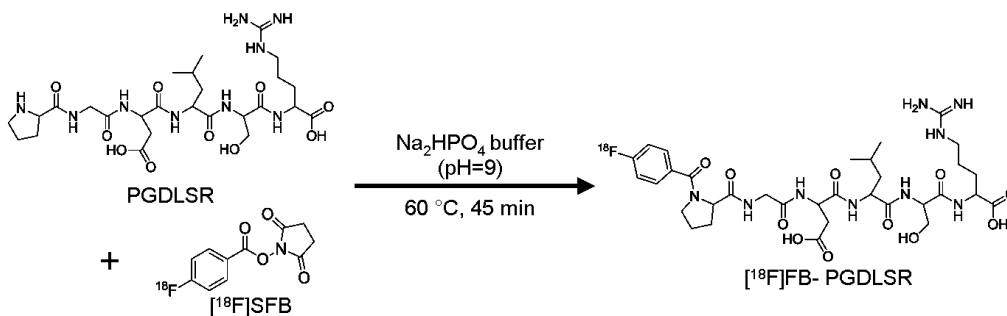


Figure 22. Synthesis of [^{18}F]FB-PGDLSR.

3.2.2.2. Labelling LIKKPF with ^{18}F

LIKKPF was labelled with [^{18}F]SFB via an acylation reaction with its terminal amino group using an on-resin approach. The primary amino groups on the two lysine residues present on resin-attached LIKKPF were protected by boc groups, preventing side reactions with these side chains. N-terminally labelled [^{18}F]FB-LIKKPF was obtained in decay-corrected radiochemical yields of $25 \pm 2\%$ (based upon [^{18}F]SFB) with radiochemical purities of $> 95\%$. The $\log D_{7.4}$ value of [^{18}F]FB-LIKKPF was determined

to be -0.80 ± 0.004 ($n = 3$). Figure 23 gives the reaction scheme for radiolabelling LIKKPF with $[^{18}\text{F}]\text{SFB}$ using the on-resin approach.

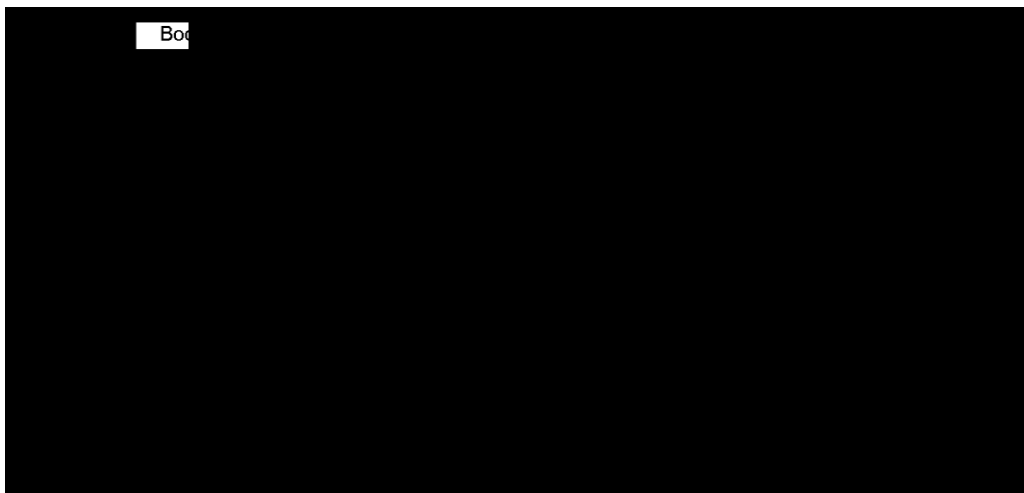


Figure 23. Synthesis of $[^{18}\text{F}]\text{FB-LIKKPF}$.

3.2.2.3. Labelling PSBP-6 with ^{18}F

We first attempted to label unmodified PSBP-6 on its N-terminus via an acylation reaction with $[^{18}\text{F}]\text{SFB}$, which was unsuccessful. PSBP-6 contains many reactive side chains that interfere with the synthesis of our desired product, $[^{18}\text{F}]\text{FB-PSBP-6}$, which is singly labelled on its N-terminus. When we attempted to label the N-terminus of PSBP-6 by protecting the reactive side chains using an on-resin approach, we were only able to obtain yields of $< 2\%$, probably due to the bulky protecting groups interfering with the desired N terminal reaction. For this reason, we modified PSBP-6 with a terminal cysteine residue for thiol-directed labelling with maleimide-based prosthetic group $[^{18}\text{F}]\text{FBAM}$. The thiol group of the terminal cys residue on C-PSBP-6 was labelled with $[^{18}\text{F}]\text{FBAM}$ via an alkylation reaction to provide $[^{18}\text{F}]\text{FBAM-C-PSBP-6}$ in decay-

corrected radiochemical yields of $41 \pm 1\%$ ($n = 2$) with $> 95\%$ RCP. The reaction scheme is provided in figure 24.

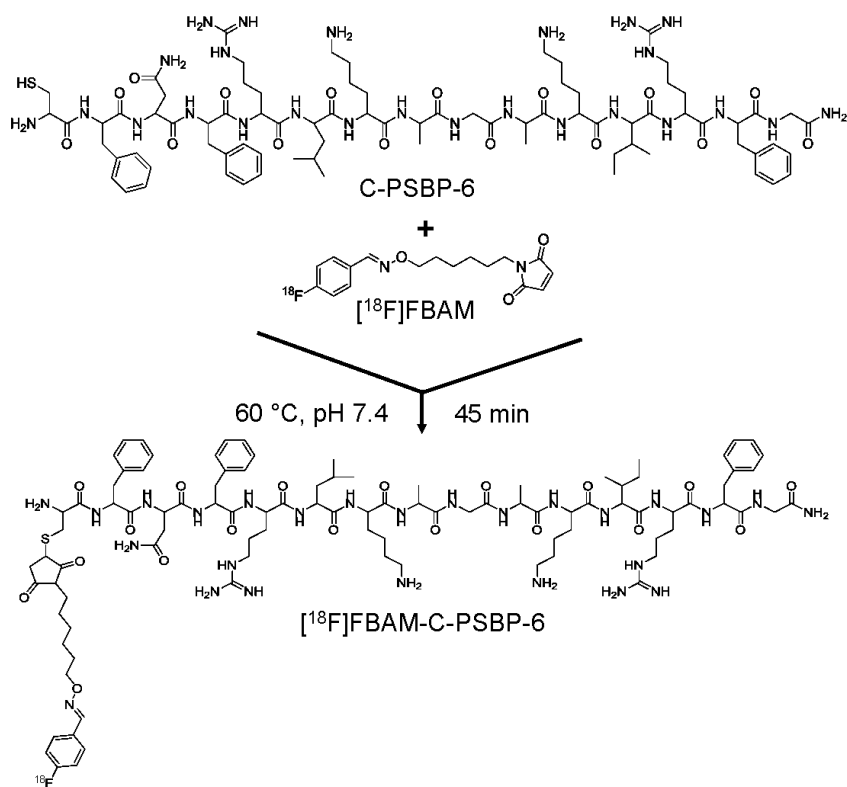


Figure 24. Synthesis of $[^{18}\text{F}]\text{FBAM-C-PSBP-6}$.

Although we were able to obtain ^{18}F -labelled C-PSBP-6 in good radiochemical yields using the thiol-directed reaction, this radiopeptide was difficult to dissolve in aqueous solutions, and tended to stick to plastic and glass containers. These limitations made further studies using $[^{18}\text{F}]\text{FBAM-C-PSBP-6}$ impractical.

3.2.3. Labelling PS-binding peptides with radiometals

Although ^{18}F is the most commonly used radionuclide for PET imaging, use of radiometals to label peptides for PET radiopharmaceutical development offers some

advantages. Labelling peptides with ^{18}F typically requires use of a prosthetic group, resulting in lengthier, multi-step procedures that require purification steps¹²¹. To label peptides with positron-emitting radiometals like ^{68}Ga or ^{64}Cu , peptides are usually first conjugated with a bifunctional chelator (BFC) like NOTA, using a spacer, like ava, to prevent steric interference of the BFC with peptide binding properties. Once this BFC-conjugated labelling precursor is prepared, radiolabelling the peptide by complexing the BFC with the radiometal of choice can usually be achieved in a simple, one-pot reaction using only microgram amounts of precursor. The challenges we encountered when labelling PSBP-6 with ^{18}F prompted us to try labelling this 14-mer peptide with radiometals instead.

3.2.3.1. Labelling PSBP-6 with ^{68}Ga

We established a procedure for radiolabelling NOTA-PSBP-6 with ^{68}Ga , which is depicted in figure 25. Decay-corrected radiochemical yields of $63 \pm 5\%$ ($n = 10$) were achieved, with radiochemical purities of $> 95\%$. The $\log D_{7.4}$ value for ^{68}Ga -NOTA-PSBP-6 was determined to be -1.7 ± 0.03 ($n = 3$).

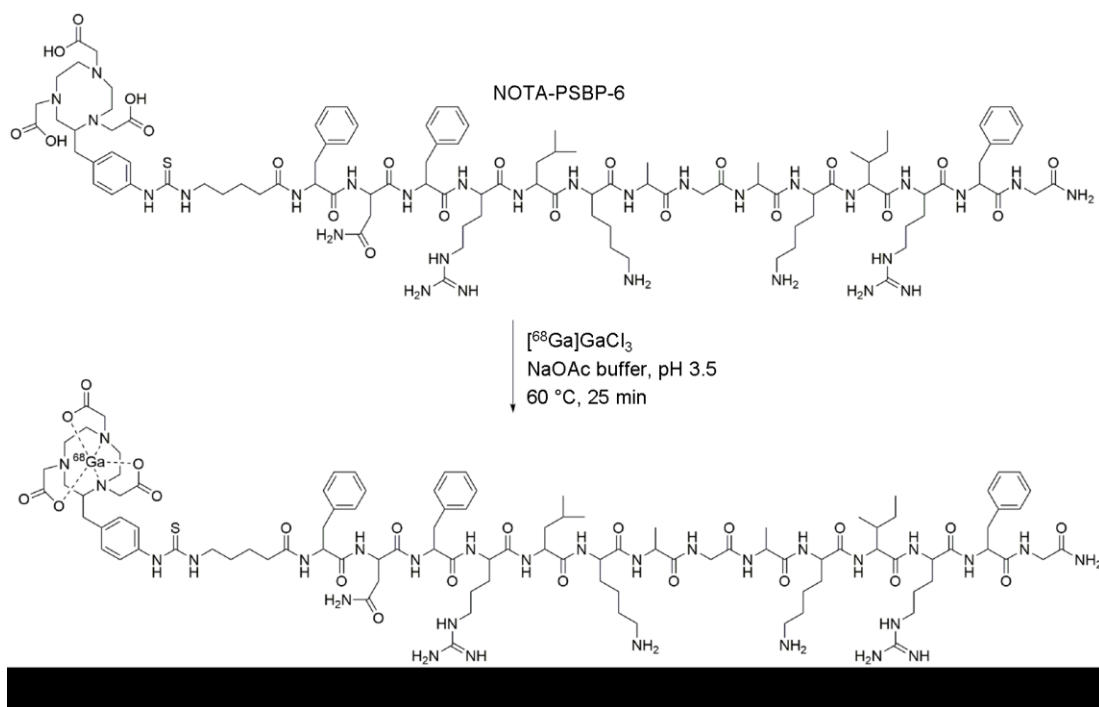


Figure 25. Radiolabelling NOTA-PSBP-6 with ^{68}Ga .

3.2.3.2. Labelling PSBP-6 with ^{64}Cu

Although we obtained ^{68}Ga -NOTA-PSBP-6 in good radiochemical yields, we were able to establish an even simpler procedure for radiolabelling NOTA-PSBP-6 with ^{64}Cu . No purification step was necessary, as decay-corrected radiochemical yields greater than 95% were achieved (RCP > 95%), as determined by radio-TLC, semi-preparative radio-HPLC, and analytical radio-HPLC. The reaction scheme for radiolabelling NOTA-PSBP-6 with ^{64}Cu is provided in figure 26. Lipophilicity determination of ^{64}Cu -NOTA-PSBP-6 gave a $\log D_{7.4}$ value of -1.6 ± 0.01 ($n = 3$).

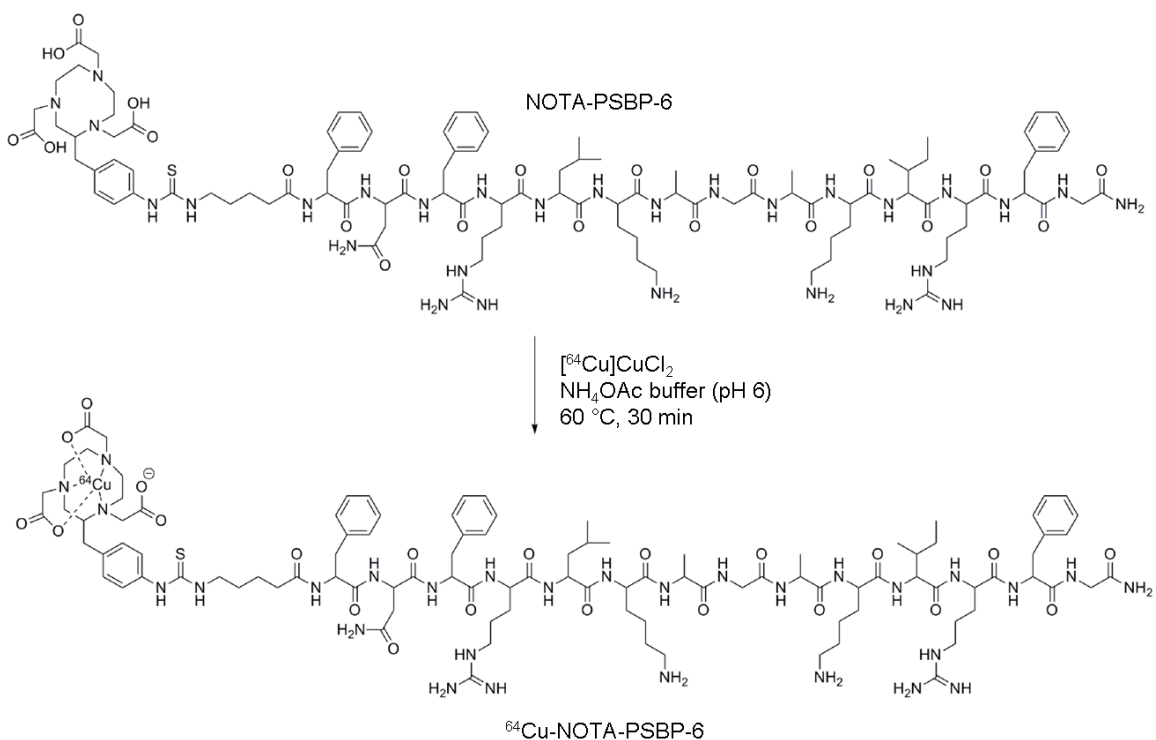


Figure 26. Radiolabelling NOTA-PSBP-6 with ^{64}Cu .

3.2.4. Metabolic stability studies

In vivo stability studies revealed that hexapeptide [^{18}F]FB-PGDLSR was very unstable in mouse blood plasma. After just 5 minutes in the plasma, there was almost no detectable intact peptide (3%). Although slightly more stable than [^{18}F]FB-PGDLSR, [^{18}F]FB-LIKKPF showed very poor stability *in vivo* as well. 15 minutes after injection, 45% of [^{18}F]FB-LIKKPF remained intact in the plasma, which decreased to 0% after 30 minutes (data not shown).

The ^{68}Ga labelled 14-mer peptide, ^{68}Ga -NOTA-PSBP-6, showed much better *in vivo* stability compared to the ^{18}F -labelled hexapeptides. HPLC determination of the presence of intact ^{68}Ga -NOTA-PSBP-6 in mouse plasma showed $58 \pm 8\%$ intact

radiopeptide 15 min after injection, after which it remained stable for the next 45 min (figure 27).

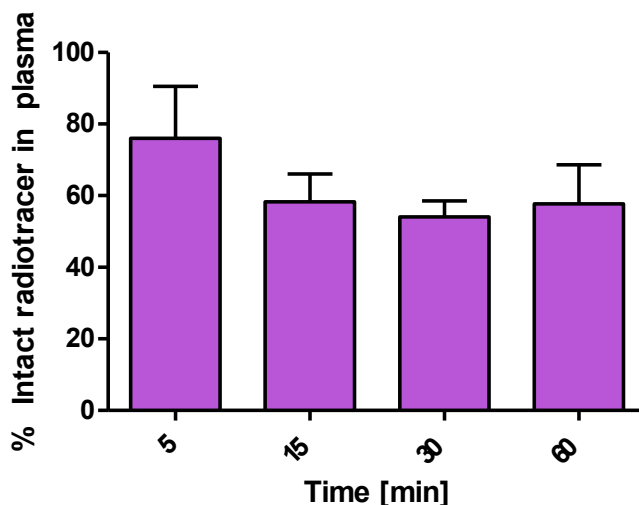


Figure 27. Stability of ^{68}Ga -NOTA-PSBP-6 in BALB/c mouse plasma over time. Plasma content of ^{68}Ga -NOTA-PSBP-6 at 5, 15, 30 and 60 min p.i. was determined by HPLC (n = 3).

The blood distribution pattern of ^{68}Ga -NOTA-PSBP-6 is shown in figure 28. At 30 min p.i., the radiopeptide was predominantly present in the plasma ($58 \pm 4\%$), where it remained over the next 30 min.

Like ^{68}Ga -NOTA-PSBP-6, ^{64}Cu -NOTA-PSBP-6 showed better *in vivo* stability than ^{18}F -labelled PGDLR and LIKKPF. At 5 min p.i., $83 \pm 4\%$ of radioactivity in the plasma was attributable to intact ^{64}Cu -NOTA-PSBP-6, which decreased to $31 \pm 11\%$ over the next 60 min (figure 29).

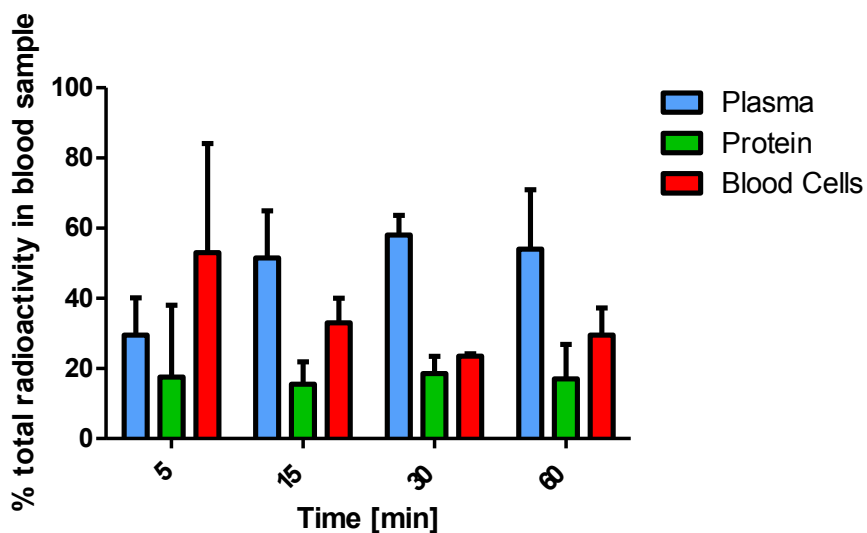


Figure 28. Blood distribution of ⁶⁸Ga-NOTA-PSBP-6 over time. Plasma, protein and blood cell content of ⁶⁸Ga-NOTA-PSBP-6 were measured from blood samples taken from BALB/c mice 5, 15, 30 and 60 min after injection of the radiopeptide (n = 3).

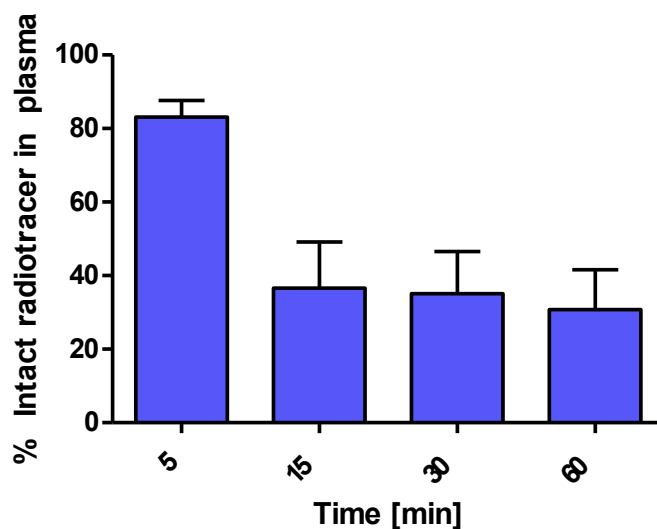


Figure 29. Stability of ⁶⁴Cu-NOTA-PSBP-6 in BALB/c mouse plasma over time. Plasma content of ⁶⁴Cu-NOTA-PSBP-6 at 5, 15, 30 and 60 min p.i. was determined by HPLC (n = 3).

A urine sample taken at 60 min p.i. was analyzed by HPLC and showed a high amount of radioactivity in the form of radiometabolites, demonstrating fast renal

clearance. The blood distribution pattern of ^{64}Cu -NOTA-PSBP-6, shown in figure 30, remained fairly constant over 60 min. At 60 min, ^{64}Cu -NOTA-PSBP-6 content in the plasma was $39 \pm 6\%$, while $41 \pm 6\%$ was bound to blood cells. Less of the radiopeptide was bound to blood proteins ($22 \pm 1\%$).

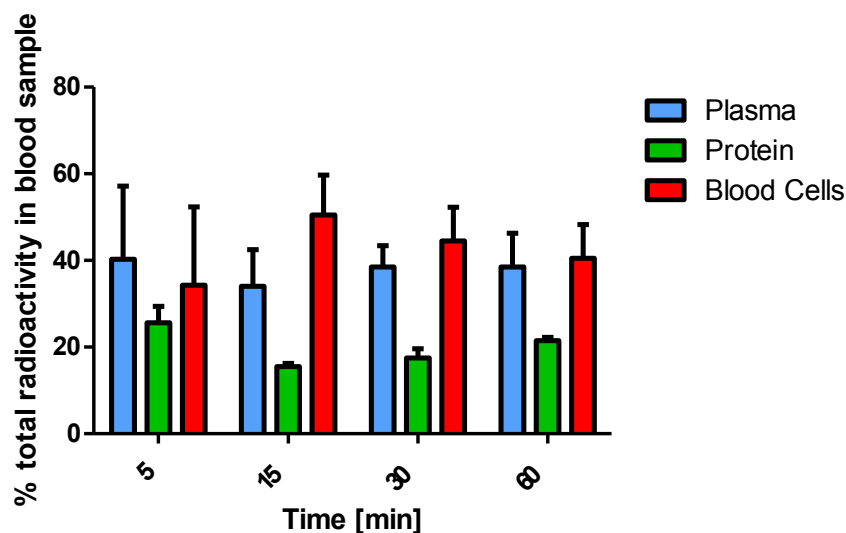


Figure 30. Blood distribution of ^{64}Cu -NOTA-PSBP-6 over time. Plasma, protein and blood cell content of ^{64}Cu -NOTA-PSBP-6 were measured from blood samples taken from BALB/c mice 5, 15, 30 and 60 min after injection of the radiopeptide (n = 3).

3.2.5. Cell binding assay using ^{64}Cu -NOTA-PSBP-6

A cell binding assay was used to evaluate binding of ^{64}Cu -NOTA-PSBP-6 to dying (treated with camptothecin) and control (untreated) EL4 cells. This assay was based on a previously described *in vitro* model of apoptosis¹⁴⁰. Figure 31 summarizes the cellular binding of ^{64}Cu -NOTA-PSBP-6 to control and apoptotic EL4 cells over 60 min of incubation. In order to confirm previous reports that PSBP-6 binding to PS is not dependent on Ca^{2+} , the assay was conducted in the absence of Ca^{2+} (figure 31a) as well as in the presence of 2.5 mM Ca^{2+} (figure 31b).

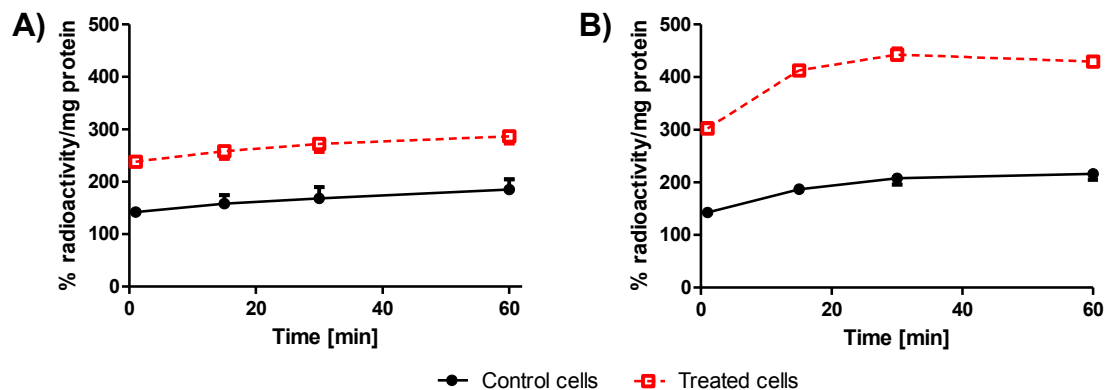


Figure 31. Binding of ⁶⁴Cu-NOTA-PSBP-6 to control and camptothecin-treated EL4 cells in the absence and presence of Ca²⁺. (A) binding of ⁶⁴Cu-NOTA-PSBP-6 to untreated (control) EL4 cells and EL4 cells treated for 22-24 h with 1.5 μM camptothecin in the absence of Ca²⁺ (n = 3); (B) binding of ⁶⁴Cu-NOTA-PSBP-6 to untreated (control) EL4 cells and EL4 cells treated for 22-24 h with 1.5 μM camptothecin in the presence of 2.5 mM Ca²⁺ (n = 3).

Similar to ¹⁸F-labelled annexin V, ⁶⁴Cu-NOTA-PSBP-6 showed baseline binding in control (untreated) cells (figures 31a and 31b). In the absence of Ca²⁺, binding of ⁶⁴Cu-NOTA-PSBP-6 to treated EL4 cells was approximately 1.5-fold higher than binding to control (untreated) cells, and this difference was consistent for the whole 60 min incubation (figure 31a). After 60 min, control cells showed 185 ± 20% radioactivity/mg protein, while treated cells had 286 ± 13% radioactivity/mg protein (n = 3, p < 0.05). Binding of ⁶⁴Cu-NOTA-PSBP-6 to control (untreated) cells was comparable between Ca²⁺-negative and Ca²⁺-positive binding assays. However, binding of ⁶⁴Cu-NOTA-PSBP-6 to camptothecin-treated EL4 cells was significantly higher (p < 0.0007) when carried out in the presence of 2.5 mM Ca²⁺. Binding of ⁶⁴Cu-NOTA-PSBP-6 in the presence of Ca²⁺ was approximately 2-fold higher in treated cells versus control cells, with 216 ± 11% radioactivity/mg protein in control cells and 429 ± 7% radioactivity/mg protein in treated cells (n = 3, p < 0.0001) (figure 31b).

3.2.6. Preclinical PET imaging of apoptosis in EL4 tumour-bearing mice using ⁶⁴Cu-labelled PSBP-6

The tumour uptake profile of ⁶⁴Cu-NOTA-PSBP-6 was studied in EL4 tumour-bearing C57Bl6 mice treated with a chemotherapeutic mixture of 100 mg/kg cyclophosphamide + 76 mg/kg etoposide for 24 h, using untreated EL4 tumour-bearing mice as controls. Figure 32 provides time-activity curves (TACs) for tumour uptake of the radiopeptide over 60 (figure 32a) and 20 min (figure 32b), as well as for tumour vs. muscle uptake of the radiopeptide over 60 min (figure 32c). During the first 10 min after injection with ⁶⁴Cu-NOTA-PSBP-6, a difference in tumour uptake between control and treated tumours was observed, which was most visible at approximately 5 min p.i. (figures 32a and 32b). At 5 min p.i., an SUV value of 0.74 ± 0.03 was obtained for control tumours, and an SUV value of 0.95 ± 0.04 was obtained for treated tumours, representing a 1.3-fold increase in ⁶⁴Cu-NOTA-PSBP-6 uptake in EL4 tumours upon treatment with a combination of cyclophosphamide and etoposide. This difference in ⁶⁴Cu-NOTA-PSBP-6 uptake between control and treated tumours is statistically significant ($p < 0.05$). However, radioactivity in the tumours was washed out over time. After 10 min, the control and treated curves begin to overlap, with no detectable difference after this point. The corresponding muscle curves shown in figure 32c do not show a difference between control and treated mice, which suggests that the difference in ⁶⁴Cu-NOTA-PSBP-6 uptake between control and treated mice is indeed tumour-specific.

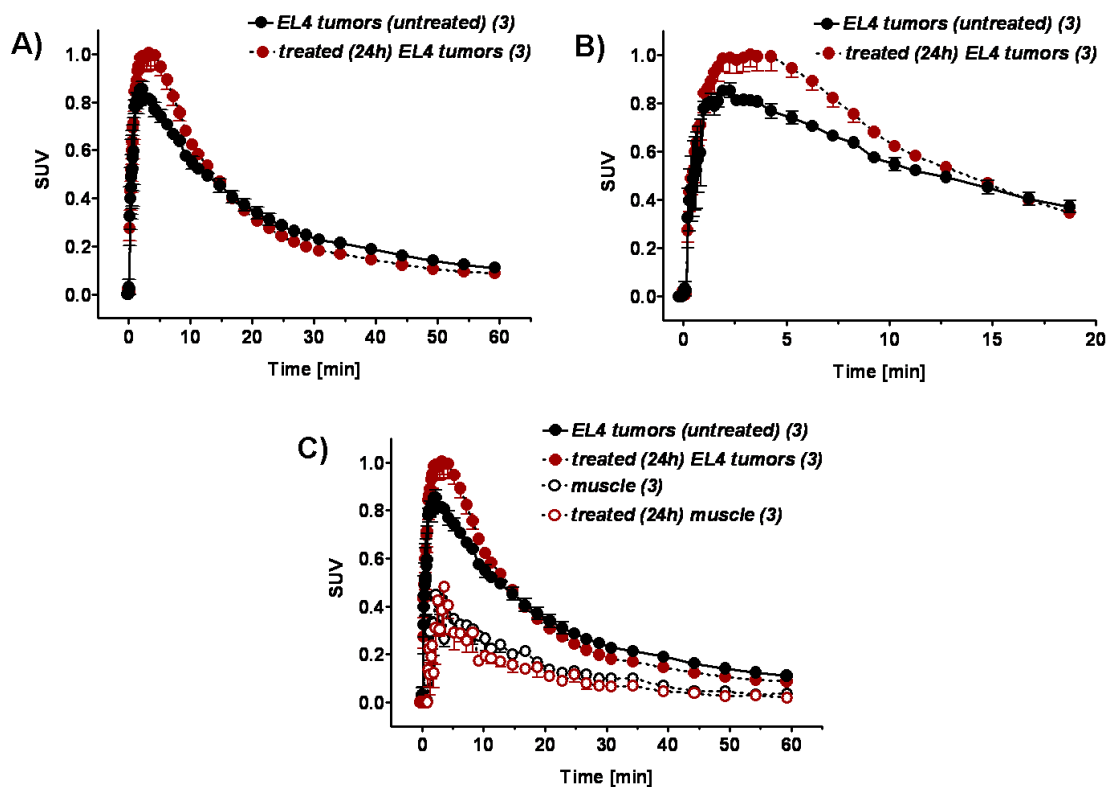


Figure 32. EL4 tumour and muscle uptake of ^{64}Cu -NOTA-PSBP-6 in C57Bl6 mice in response to treatment with cyclophosphamide and etoposide. TACs were generated from measurement of tumour and muscle uptake of ^{64}Cu -NOTA-PSBP-6 in both control (untreated) EL4 tumour-bearing mice and EL4 tumour-bearing mice treated with 100 mg/kg cyclophosphamide + 76 mg/kg etoposide 24 h before imaging. (A) Tumour uptake of the radiopeptide over 60 min; (B) Tumour uptake of the radiopeptide over 20 min; (C) Tumour vs. muscle uptake of the radiopeptide over 60 min. Data are shown as SUV mean \pm SEM (n = 3).

Figures 33 and 34 summarize the results from the dynamic PET studies displaying PET images at 5 min p.i., since differences between control and treated tumours were most visible at this time.

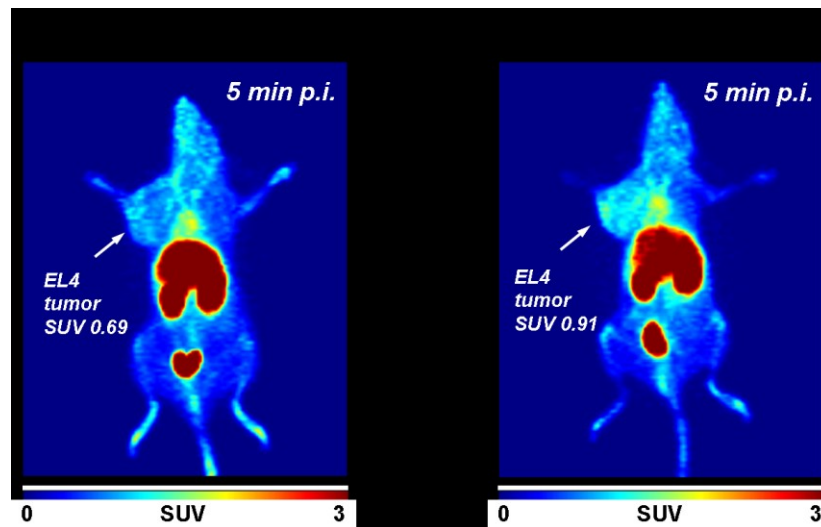


Figure 33. Representative preclinical PET images of EL4 tumour response to treatment with cyclophosphamide and etoposide using ^{64}Cu -NOTA-PSBP-6 as radiotracer, shown as MIPs. (A): control (untreated) EL4 tumour-bearing C57Bl6 mice; (B): EL4 tumour-bearing C57Bl6 mice treated with 100 mg/kg cyclophosphamide + 76 mg/kg etoposide 24 h before imaging. Images are shown as MIPs taken 5 min after a single tail vein injection of ^{64}Cu -NOTA-PSBP-6.

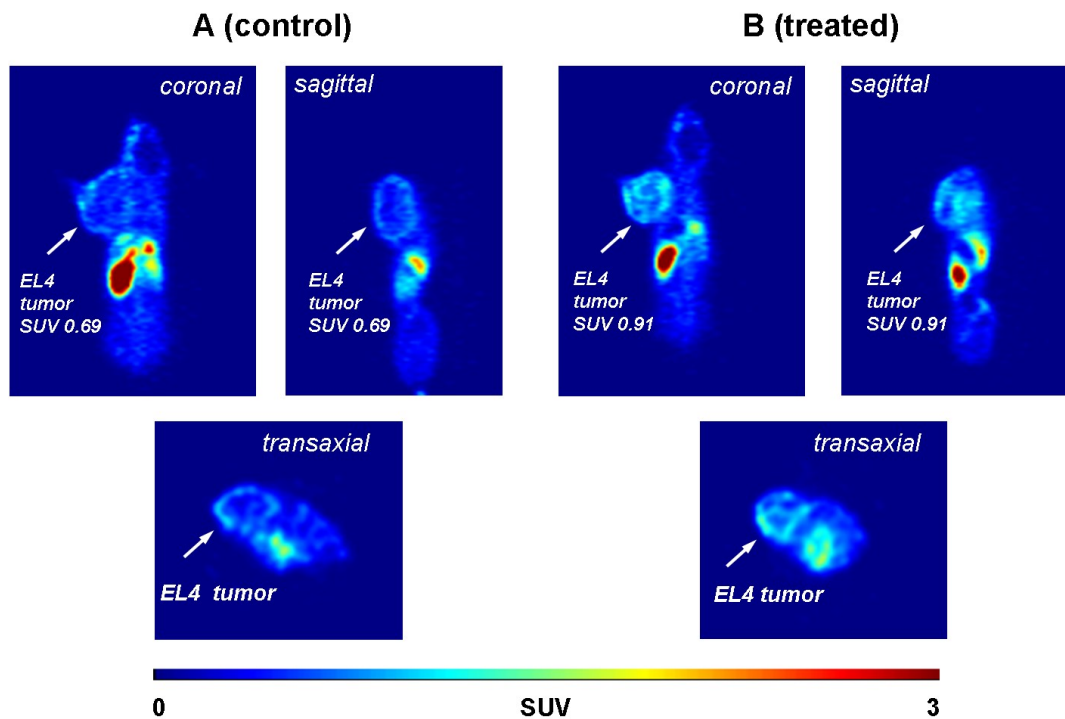


Figure 34. Representative preclinical PET images of EL4 tumour response to treatment with cyclophosphamide and etoposide using ^{64}Cu -NOTA-PSBP-6 as radiotracer, shown as coronal, sagittal and transaxial tumour slices. Images were taken 5 min after a single tail vein injection of ^{64}Cu -NOTA-PSBP-6 in both (A) control (untreated) EL4 tumour-bearing C57Bl6 mice and (B) EL4 tumour-bearing C57Bl6 mice treated with 100 mg/kg cyclophosphamide + 76 mg/kg etoposide 24 h before imaging.

3.3. Evaluation of fluorescently-labelled PS-binding peptides for detection of apoptosis

3.3.1. Flow cytometry of EL4 cells using FITC-PSBP-6

We also synthesized a fluorescently-labelled version of PSBP-6, FITC-PSBP-6, which we evaluated in flow cytometry experiments that examined its ability to fluorescently stain and thus detect apoptotic cells *in vitro*. The results from these experiments are depicted in figure 35. A low level of nonspecific binding of the

fluorescently-labelled peptide was observed. Binding of FITC-PSBP-6 doubled from baseline after treatment with apoptosis-inducing agent camptothecin. 20% of control cells were stained by FITC-PSBP-6, which significantly increased to 41% in treated cells ($p < 0.001$).

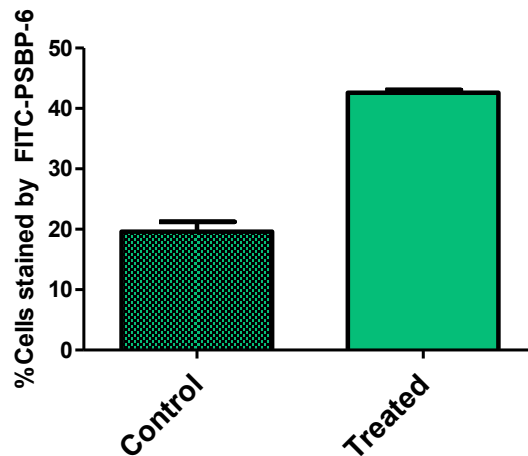


Figure 35. Flow cytometric analysis of EL4 cells undergoing camptothecin-induced apoptosis using FITC-PSBP-6 as fluorescent stain. FITC-PSBP-6 staining was measured in control (untreated) EL4 cells and EL4 cells treated with 1.5 μM camptothecin for 22-24 h ($n = 3$). 1 μM of FITC-PSBP-6 was used to stain the cells.

3.3.2. Confocal fluorescence microscopy using FITC-PSBP-6

The ability of FITC-PSBP-6 to bind to EL4 cells undergoing camptothecin-induced cell death was further examined using confocal fluorescence microscopy. Apoptotic response was visualized by staining the treated cells with FITC-PSBP-6 and DEVD-based fluorescent NucView 405 Caspase-3 Substrate. PI was used to distinguish between dead/necrotic/late apoptotic cells and early apoptotic cells. The images from these experiments are provided in figure 36. On cells with intact membranes (not stained with PI), FITC-PSBP-6 appeared to bind to just the cell membrane, without being internalized (figure 36b, 36c and 36d). Cells brightly stained by NucView 405 Caspase-3 Substrate but not PI showed binding of FITC-PSBP-6 on the cell membrane, indicating

cells undergoing early apoptosis (figure 36a, 36b and 36d). Cells that seemed to internalize FITC-PSBP-6, showing heavy green stain throughout the cell, were also heavily stained with PI and NucView 405 Caspase-3 Substrate, marking them as late apoptotic (figure 36d).

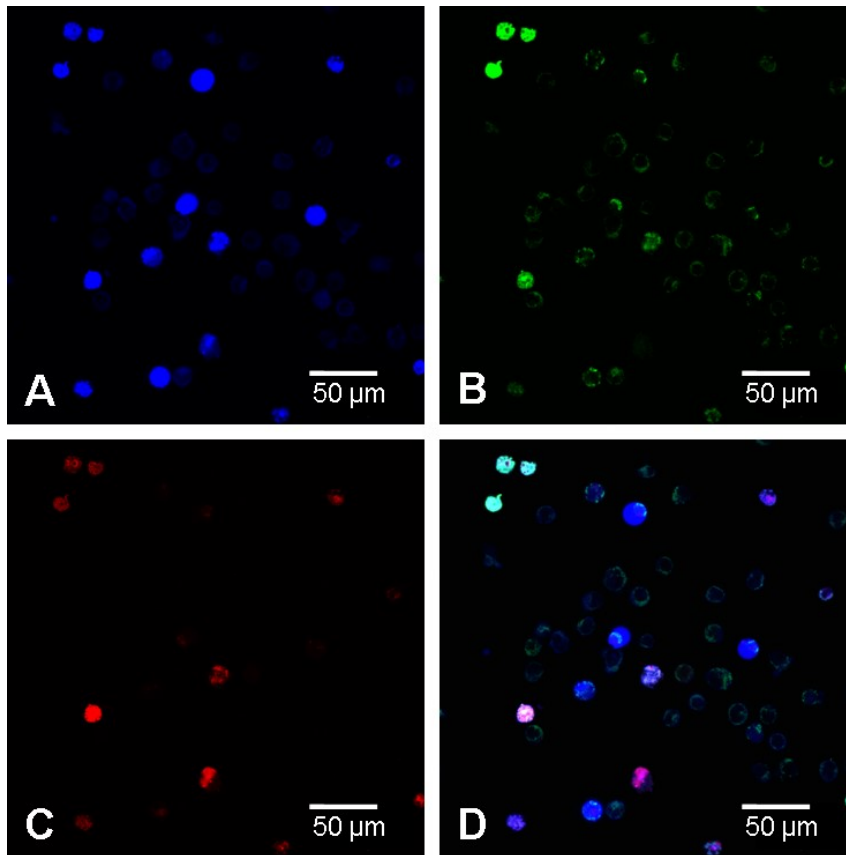


Figure 36. Fluorescence confocal microscopy images of EL4 cells stained with FITC-PSBP-6, NucView 405 Caspase-3 Substrate and PI to image camptothecin-induced cell death. Cells were treated with 1.5 μM of camptothecin for 22-24 h before imaging. (A) apoptotic cells stained with NucView 405 Caspase-3 Substrate (blue); (B) cells stained with FITC-PSBP-6 (green); (C) necrotic/late apoptotic cells stained with PI (red); (D) All three stains (red, green and blue) superimposed.

4. DISCUSSION

4.1. Comparison of wild-type annexin V radiolabelled with ¹⁸F using random vs. site-selective approaches

The first part of this study describes two different methods for radiolabelling wild-type annexin V with ¹⁸F, and evaluates the effect that radiolabelling technique has on the ability of this protein to detect dying cells *in vitro*. Radiolabelling wild-type annexin V with prosthetic group [¹⁸F]SFB has been reported by several groups over the past decades, and results from this study further confirm the feasibility of using [¹⁸F]SFB to label annexin V with ¹⁸F according to this random labelling method^{9,123–126}. Although we obtained lower radiochemical yields (9%) of ¹⁸F-labelled annexin V than other groups, this can be explained by the significantly smaller amount (0.1 mg) of wild-type annexin V used in our reactions. Other groups reported radiochemical yields of 42-70% using much higher annexin V amounts in the range of 1 mg of protein^{9,124,125}. However, our obtained radiochemical yield of 9% was comparable to the reported 10% radiochemical yield by Murakami and colleagues, who also used small amounts (0.1 mg) of wild-type annexin V for radiolabelling with [¹⁸F]SFB¹²⁶. Toretzky and colleagues described a linear relationship ($r^2=0.89$) between protein concentration and radiochemical yield of [¹⁸F]SFB-annexin V, which provides a good explanation for the obtained radiochemical yields. The fairly high cost of wild-type annexin V makes the use of small amounts of the protein during the radiolabelling reaction highly desirable. Moreover, smaller amounts of protein provide radiolabelled annexin V at higher specific radioactivity.

Successful bioconjugation of the single cysteine residue at position 315 in wild-type annexin V was recently reported¹³⁵. Glucose-based maleimide prosthetic group [¹⁸F]FDG-MHO gave ¹⁸F-labelled annexin V in radiochemical yields of 43-58% starting from 0.1 mg of wild-type annexin V. This result makes [¹⁸F]FDG-MHO a highly suitable prosthetic group for bioconjugation of wild-type annexin V. However, [¹⁸F]FDG-MHO is a rather large prosthetic group compared to [¹⁸F]SFB (figure 37). In addition to the maleimide group, it also contains a hydrophilic sugar moiety prone to modify the pharmacokinetic properties of the protein, unlike [¹⁸F]SFB, which lacks such a polar substitution pattern. These differences in size and pharmacokinetic profile create a challenge for direct comparison of wild-type annexin V labelled randomly using [¹⁸F]SFB versus annexin V site-specifically labelled with [¹⁸F]FDG-MHO.

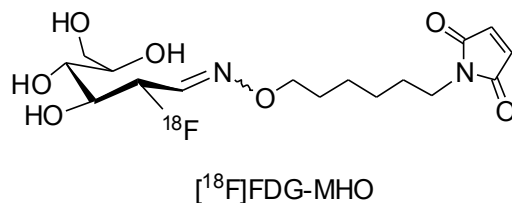


Figure 37. Structure of [¹⁸F]FDG-MHO.

Maleimide-containing compound [¹⁸F]FBEM is an alternative thiol-selective prosthetic group that is more comparable to the size of [¹⁸F]SFB. This consideration also applies to the corresponding [¹⁸F]FBEM-labelled annexin V derivative (figure 7). This makes [¹⁸F]FBEM a suitable prosthetic group for comparison with acylation agent [¹⁸F]SFB, despite the rather low radiochemical yield of 4% obtained for its bioconjugation to wild-type annexin V.

Our observed elevated binding of [^{18}F]SFB-annexin V to EL4 cells treated with camptothecin compared to untreated cells confirms previous reports on the feasibility of using randomly labelled [^{18}F]SFB-annexin V for the detection of cell death. The PS-binding ability of [^{18}F]SFB-annexin V has been evaluated in various other cell lines. Grierson and colleagues demonstrated PS-binding of [^{18}F]SFB-annexin V with a cell binding assay using red blood cells (RBCs) with exposed PS¹²⁴, while Zijlstra et al. demonstrated 60% increased binding of [^{18}F]SFB-annexin V to UV-irradiated Jurkat human T-lymphoma cells compared to non-irradiated cells¹²⁵. Another study by Toretsky et al. found 88% more binding of [^{18}F]SFB-annexin V to TC32 sarcoma cells treated with etoposide compared to untreated cells⁹. Calcium concentration used in these annexin V binding assays is a point of criticism, since concentrations of 2.5-5.0 mM Ca^{2+} were used, and it is known that annexin V binding is largely Ca^{2+} -dependent and declines rapidly over a range of 2.5-1.25 mM¹⁶⁰. When we conducted another set of cell binding assays using a lower Ca^{2+} concentration of 1.25 mM, we observed a significant reduction in ^{18}F -labelled annexin V binding to both treated and untreated EL4 cells as expected. However, the lower Ca^{2+} concentration did not diminish the preferential binding of ^{18}F -labelled annexin V to cells treated with the chemotherapeutic agent compared to untreated cells. Thus, our cellular binding assay remained robust even at a lower Ca^{2+} concentration. Results of the cell binding assays shown in Figures 11 and 14 confirm that both randomly labelled [^{18}F]SFB-annexin V and site-specifically labelled [^{18}F]FBEM-annexin V retained the ability to detect cell death *in vitro*. Both ^{18}F -labelled wild-type annexin V derivatives demonstrated significantly higher binding to EL4 cells treated with 1.5 μM

camptothecin compared to untreated cells, and showed comparable binding and kinetics. This suggests that random and site-selective methods for radiolabelling wild-type annexin V provide radiotracers with comparable PS-binding abilities. In our experiments, no significant differences were observed in binding of both ^{18}F -labelled annexin V derivatives to apoptotic cells. However, this finding is in contrast to a comparative study reported by Tait and colleagues, who found that amine-directed random modification of annexin V substantially reduced its ability to bind to PS-expressing RBCs, though it did not diminish it completely¹³⁰. They also showed that the more conjugated annexin V is, the lower its PS binding ability becomes. Site-selective conjugation of an additional cysteine residue present in the modified amino-terminal sequence of Ala-Gly-Gly-Cys-Gly-His of annexin V-128 (a second generation annexin V) resulted in an increased binding of the protein to RBCs¹³⁰. However, Grierson et al. determined that even high [^{18}F]SFB:annexin V molar ratios (32:1) during a 15 min incubation time for the conjugation reaction resulted in a rather low (2.1) average incorporation of the label into annexin V without loss of PS binding properties¹²⁴. Only extension of the reaction time from 15 min to 60 min resulted in a conjugated product with compromised PS binding ability.

Our described conjugation method uses HPLC-purified [^{18}F]SFB and [^{18}F]FBEM at high specific activity. Moreover, mild reaction conditions (PBS, 30 min, 30 °C, pH 7.4) during the conjugation reactions enable introduction of the radiolabel while preserving the structural and functional integrity of wild-type annexin V. This was demonstrated by the observed comparable PS-binding ability of both randomly labelled and site-specifically labelled annexin V derivatives. However, given the rather low

radiochemical yields for [^{18}F]FBEM-annexin V (4%) combined with the lengthier and more complex synthesis of maleimide-based prosthetic group [^{18}F]FBEM, it is more practical to use the random labelling technique with [^{18}F]SFB to prepare ^{18}F -labelled wild-type annexin V. Radiolabelling of wild-type annexin V with the more readily available prosthetic group [^{18}F]SFB provides ^{18}F -labelled annexin V in reasonable radiochemical yields of around 10% while using only small amounts of wild-type annexin V (0.1 mg) as starting material.

4.2. Limitations and challenges of using annexin V for molecular imaging of cell death

The EL4 tumour model used in this study has been previously used to analyze tumour apoptosis *in vivo*, induced by either radiation or chemotherapy^{68,100,157,161}. Daily treatment with a combination of cyclophosphamide and etoposide for 48 h has been shown to increase the amount of apoptosis in EL4 tumors from 4% (basal level) to 32% after treatment, confirmed by histological analysis using the terminal deoxynucleotidyl transferase-mediated deoxyuridine triphosphate nick-end labelling (TUNEL) assay¹⁶¹. Using this model, assessment of baseline (control) EL4 tumour uptake of our randomly labelled [^{18}F]SFB-annexin V using dynamic PET imaging revealed rapid uptake in the first 10 min followed by retention of the radiotracer over 90 min (figures 15 and 16). This finding agrees with the results from our *in vitro* experiments using EL4 cells, which also showed a baseline binding of [^{18}F]SFB-annexin V in control (untreated) cells.

Although our cell binding assay also showed a significant increase in [^{18}F]SFB-annexin V binding in EL4 cells when treated with an apoptosis-inducing agent, this was not reflected in our *in vivo* model. We observed no increase in [^{18}F]SFB-annexin V

uptake in drug-treated EL4 tumours compared to control (untreated) tumours, even when we tried imaging at various time points post-treatment in order to capture the time of maximum PS exposure in the tumour (figures 17 and 18). This finding is in contrast with the study done by Guo et al., who reported significant increases in ^{99m}Tc -HYNIC-annexin V uptake in the EL4 tumor model upon radiation-induced apoptosis, but no detectable baseline uptake in control (non-irradiated) tumours¹⁰⁰. The reported absolute uptake of radioactivity in their EL4 tumour model was rather low (0.355 %ID/g 2 h p.i.), with only a 1.7 to 2.3-fold increase in uptake in the tumour upon treatment, and this group failed to see any increase in ^{99m}Tc -HYNIC-annexin uptake in another tumour model using irradiated S180 sarcoma tumours.

Whereas absolute tumour uptake of radiolabelled annexin V and increases in tumour uptake upon treatment-induced apoptosis in tumour models have been quite small (usually a 1.5-fold increase, approximately)^{94,96,100,119,127,162}, other preclinical models of apoptosis such as treatment-induced liver apoptosis have shown a drastic increase (3- to 40-fold) in radiolabelled annexin V uptake and a much higher absolute uptake in the liver and other target organs^{117,119,123,127,163–167}. For example, a ^{68}Ga -labelled form of annexin V showed a 3- to 8-fold increase in uptake in mouse livers upon treatment with anti-Fas, but only a 1.5- to 2-fold increase in uptake in daudi lymphoma tumours upon treatment with cyclophosphamide, with a maximum uptake of only 0.156 %ID/g¹¹⁹. Similarly, Yagle et al. showed a 3- to 9-fold increase in uptake of [^{18}F]SFB-annexin V into cyclohexamide-treated liver tissue compared to healthy tissue in rats¹²³, demonstrating that randomly labelled wild-type [^{18}F]SFB-annexin V can indeed image cell death *in vivo*, contrary to the negative imaging results we obtained in our tumour model. Another preclinical study

that has demonstrated the feasibility of detecting cell death using randomly labelled wild-type [^{18}F]SFB-annexin V was carried out by Murakami and colleagues, who observed a 3-fold higher uptake of [^{18}F]SFB-annexin V in the infarct area of rat hearts compared to non-infarct areas in an *ex vivo* study of rat myocardial ischaemia and reperfusion¹²⁶. Apart from our present study, there is only one other report evaluating randomly labelled wild-type [^{18}F]SFB-annexin V in a tumour model of therapy-induced apoptosis¹²⁷. Hu and colleagues examined [^{18}F]SFB-annexin V uptake into UM-SCC-22B head and neck tumours in mice after treatment with chemotherapeutic agent doxorubicin, using a longitudinal imaging approach over several days in order to determine the most optimal time for imaging post-treatment (i.e., the time of greatest PS exposure)¹²⁷. They imaged the mice at day 0, 6 h, day 1, 3 and 7 after treatment was initiated, and found that the most significant increase in tumour uptake of [^{18}F]SFB-annexin V occurred 3 days post-treatment, (1.8-fold increase from 0.89 to 1.56 %ID/g). At day 7, differences in [^{18}F]SFB-annexin V uptake between control and treated tumours disappeared, and the tumours had begun to shrink. At day 3 when tumour uptake of [^{18}F]SFB-annexin V was highest, no visible changes in tumour size had occurred, suggesting that the optimal time for imaging with [^{18}F]SFB-annexin V precedes decreases in tumour volume. In accordance with many other studies of radiolabelled annexin V, when Hu et al. measured [^{18}F]SFB-annexin V uptake in mouse livers after treatment with cyclohexamide, they observed a much greater increase in uptake (4.3-fold) compared to the tumour model.

Taken together, these findings suggest that while radiolabelled annexin V appears to be extremely effective at imaging cell death in many preclinical models of cell death including treatment-induced liver apoptosis, use of this radiotracer in tumour models of

cell death may be more challenging. It is known that solid tumours have high interstitial fluid pressure due to a lack of functional intratumoural lymphatic vessels, which contributes to poor penetration and accumulation of targeted agents into tumours, particularly when using large molecules such as antibodies or proteins^{168,169}. Although annexin V is not as large as other molecules like antibodies, the moderately high molecular weight of this protein may contribute to its poor uptake into tumours compared to normal tissues such as the liver, which have lower interstitial fluid pressure. Furthermore, solid tumours often have chaotic, disorganized vasculature, which results in uneven blood distribution throughout the tumour, limiting access of annexin V to regions with poor blood supply¹⁶⁸. Many chemotherapeutic drugs also cause the unstable vasculature in tumours to collapse, further decreasing blood flow and thus annexin V access to the tumour¹⁷⁰. This idea is supported by the autoradiography studies done by Bauwen and colleagues, which revealed non-uniform uptake of radiolabelled annexin V into Daudi lymphoma tumours¹¹⁹. While some regions of the tumour showed a 20-fold increase in ⁶⁸Ga-labelled annexin V when treated with cyclophosphamide, other regions showed no increase at all. However, this might also be a result of heterogeneity of tumour cell response to therapy.

Although tumour models of apoptosis show smaller increases in radiolabelled annexin V uptake compared to other models of apoptosis, increases in tumour uptake have still been significant, which we did not see in the EL4 model we used for evaluating [¹⁸F]SFB-annexin V. The small increases in radiolabelled annexin V uptake that appear to occur during a short window of time emphasize the importance of precise optimization of imaging protocols according to the tumour model used. Based on the findings by Hu et

al., it is likely that despite the inclusion of earlier time points for imaging the mice post-treatment, we were unable to find the optimal time for imaging cyclophosphamide/etoposide-induced apoptosis in EL4 tumours using [¹⁸F]SFB-annexin V. Since the tumours had already begun to visibly decrease in size after 2 consecutive days of treatment, the absence of apoptotic cells in the tumours due to physiological removal by phagocytes resulted in a lack of [¹⁸F]SFB-annexin V uptake into the tumours. Thus, the dose we used to treat the tumours (100 mg/kg cyclophosphamide + 76 mg/kg etoposide) was possibly too high, causing rapid and extensive cell death with insufficient time to image the process. We then tried imaging at 4, 12 and 24 h post treatment, thus providing only one dose of treatment to the mice rather than two consecutive doses. At these earlier time points, no decreases in tumour size had occurred (figure 18). Although we observed higher uptake of [¹⁸F]SFB-annexin V at these earlier time points compared to the 48 h time point, we still did not observe an increase in uptake compared to control tumours. It is possible that we were simply unable to find the time of greatest PS exposure for imaging the tumours. Many other studies using ^{99m}Tc-HYNIC-annexin V uptake in tumour models of treatment-induced apoptosis have also described a need to optimize the time of imaging, as uptake of this radiotracer is heavily dependent on the amount of time between treatment and imaging, which varies according to tumour model and treatment type^{171,172}.

Another limitation associated with annexin V-based imaging of cell death *in vivo* is the need for sufficient levels of ionized calcium in order for the protein to bind to PS. The ability to control Ca²⁺ concentration in cell-based apoptosis assays makes the use of annexin V probes very feasible *in vitro*; however, it is difficult to control *in vivo* Ca²⁺

levels in the blood plasma and around the tumour tissue. The EL4 tumour model was also used to evaluate ^{111}In -labeled APOMAB, a DAB4 clone of a La/SSB-specific murine mAb. This antibody showed significantly increased uptake in EL4 tumours after drug treatment, which correlated with histological analyses of tumour biomarkers of apoptosis⁶⁶. With an entirely different mechanism of action for detection of cell death, APOMAB does not rely on sufficient Ca^{2+} levels in order to function. This may be a factor in explaining the ability of this antibody to image cell death in the same EL4 model used in our study, while [^{18}F]SFB-annexin V was unable to image cell death in a similar fashion. The EL4 lymphoma model may imply special challenges for targeting PS with [^{18}F]SFB-annexin V based on Ca^{2+} levels as well as tissue perfusion properties. Further studies of this EL4 tumour model would be needed in order to investigate these possibilities.

4.3. PS-binding peptides as promising alternatives for molecular imaging of cell death

Various peptides containing sequences LIKKPF, PGDLSR and FNFRLKAGAKIRFG (the amino acid sequence for PSBP-6) were evaluated for their PS binding abilities using a novel competitive radiometric binding assay. In this assay, PS was immobilized and competitive binding of ^{64}Cu -NOTA-annexin V was measured in a concentration-dependent manner in the presence of all compounds tested. Peptides LIKKPF, PGDLSR and PSBP-6 were selected as PS-binding lead structures based on previous reports that have described their dissociation constants (K_d) for PS as in the nanomolar range^{140,146}. Burtea et al. estimated IC_{50} values for PGDLSR and LIKKPF using an *in vitro* competitive PS binding assay with biotinylated annexin V as competitor,

reporting an IC_{50} value of 1.48 nM for LIKKPF and 1.33 nM for PGDLSR¹⁴⁰. In our present study, we have estimated IC_{50} values for PGDLSR, LIKKPF and derivatives of both peptides by analyzing PS-binding competition of these peptides against ⁶⁴Cu-NOTA-annexin V. Our assay revealed that all unmodified and modified versions of both hexapeptides displayed IC_{50} values in the low mM range, describing affinities of about four to five orders of magnitude higher than the nM IC_{50} value obtained for wild-type annexin V, our internal reference (figure 19). The found discrepancy in the determined IC_{50} values may result from different sensitivities of the detection methods used in the PS-immobilized in vitro assay. While Burtea et al. performed a staining reaction between horseradish peroxidase (HRP)-conjugated streptavidin and biotinylated annexin V¹⁴⁰, we detected PS-bound ⁶⁴Cu-NOTA-annexin V in our radiometric binding assay directly. This is important since all compounds, including annexin V, were assayed under the same conditions, allowing for an immediate and direct comparison of their individually determined IC_{50} values. The lack of data on directly determined IC_{50} values for annexin V in the report by Burtea et al. makes it difficult to compare the obtained IC_{50} values from both PS-binding assays. Our assay clearly demonstrated that all LIKKPF- and PGDLSR-based peptides (LIKKPF, PGDLSR, FBz-LIKKPF, FBz-PGDLSR, FBAM-CLIKKPF and FBAM-CPGDLSR) exhibit significantly less potent binding to PS compared with wild-type annexin V. FBz- and FBAM-conjugates of both hexapeptides exhibited slightly better affinities than the unmodified versions, probably due to the addition of lipophilic groups ($\log P_{SFB}=1.5$, $\log P_{FBAM}=3.22$) that enhance peptide interaction with phospholipids. However, our study could not confirm high potencies of

LIKKPF- or PGDLSR-based peptides towards PS in the nM range as reported by Burtea et al¹⁴⁰.

The reported PS-binding peptide PSBP-6¹⁴⁶ is a modified version of the synthetic 14-mer peptide PSBP-0 (sequence FNFRLKAGQKIRFG) identified by Igarashi et al. in 1995. PSBP-0 was derived from a conserved PS-specific binding site found on protein kinase C and PS decarboxylase, which converts PS to PE¹⁷³. Although PSBP-0 was found to bind specifically to PS, its low affinity prompted Xiong and colleagues to produce a library of 14-mer peptides based on the PSBP-0 sequence in order to identify a peptide with higher affinity for PS¹⁴⁶. From this peptide library, PSBP-6 was identified, displaying a K_d value of approximately 100 nM as determined by a surface-plasmon resonance (SPR) biosensory assay¹⁴⁶. When we evaluated the PS binding potency of PSBP-6-based peptides using our competitive radiometric binding assay with ⁶⁴Cu-NOTA-annexin V as competitor (figures 20 and 21), we observed an IC_{50} value of 0.60 mM for unmodified PSBP-6, which was about four orders of magnitude higher than that determined for annexin V (51 nM). It is difficult to directly compare the absolute affinities observed for PSBP-6 between our PS binding assay and the SPR assay used by Xiong and colleagues, since the methods are completely different, and we determined IC_{50} values while SPR generated K_d values. However, our IC_{50} value obtained for PSBP-6 was three orders of magnitude higher than the K_d value of 100 nM determined for PSBP-6 by Xiong et al., which is quite a large discrepancy¹⁴⁶. When we conjugated PSBP-6 on its N terminus with FBz, we found that this increased the affinity of PSBP-6 by one order of magnitude (a decrease in IC_{50} from 0.60 mM to 69 μ M), due to the addition of the lipophilic group that enhances binding to phospholipids. Addition of a

cysteine residue to the N-terminus of PSBP-6 resulted in an increase in affinity by two orders of magnitude (a decrease in IC_{50} from 0.60 mM to 6.4 μ M). A possible explanation for this increase might be gleaned from previous reports that cysteine-rich domains are required for binding of some proteins such as Raf-1 to PS, suggesting that cysteine residues somehow enhance PS binding^{174,175}. Xiong et al. next wanted to determine whether addition of Lys[di(2-pyridinemethyl)]-COOH, a single amino acid chelator (SAAC), to the N-terminus of PSBP-6 and subsequent complexation of ^{99m}Tc for SPECT imaging with this peptide would affect its PS binding affinity. In fact, conjugation of PSBP-6 with SAAC to make SAAC-PSBP-6 resulted in a peptide with improved binding affinity for PS due to the lipophilic nature of the SAAC, which strengthened interactions between the peptide and hydrophobic phospholipid. SAAC-PSBP-6 was then complexed with rhenium (Re), which is often used as a nonradioactive substitute for ^{99m}Tc due to similar properties of the complexes produced by these two metals (figure 38)¹⁴⁶.

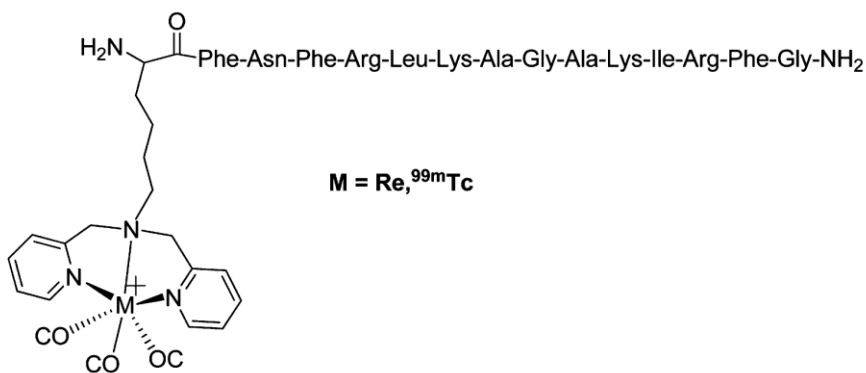


Figure 38. Structure of SAAC-PSBP-6 complexed with Re or ^{99m}Tc. Adapted from Xiong et al¹⁴⁶.

Complexation of SAAC-PSBP-6 with Re led to a further increase in PS-binding affinity of the peptide ($K_d = 26$ nM) due to the introduction of the positively-charged metal, which allows for stronger interactions with the negatively charged phospholipid

PS¹⁴⁶. Thus, conjugation of PSBP-6 to Re-SAAC-PSBP-6 lead to an increase in PS binding affinity by almost one order of magnitude. Similarly, when we conjugated PSBP-6 with NOTA to make NOTA-PSBP-6, we observed an improvement in PS binding affinity by approximately one order of magnitude for the peptide as well, from 0.6 mM to 30 μ M. The reasons for the increased affinity of NOTA-PSBP-6 compared to PSBP-6 are less clear, as NOTA is a relatively hydrophilic bifunctional chelator¹⁷⁶. Perhaps Ca²⁺ ions present in the assay buffer were recruited to the negatively charged NOTA group, enhancing PS binding interactions with NOTA-PSBP-6. Xiong et al. also conducted a competition experiment whereby a static concentration of annexin V (100 nM) was mixed with increasing concentrations of SAAC-PSBP-6, and they found that a SAAC-PSBP-6 concentration of 256 nM reduced annexin V binding to PS by 50%. This would correspond to an IC₅₀ value of 256 nM for SAAC-PSBP-6 competing with annexin V for PS. This suggests a much higher affinity of SAAC-PSBP-6 for PS compared to the affinities we obtained for any of our PSBP-6-based peptides, which all showed IC₅₀ values in the micromolar range. Complexation of NOTA-PSBP-6 with nonradioactive Ga³⁺ or Cu²⁺ did not induce significant changes in affinity: IC₅₀(Ga-NOTA-PSBP-6) = 33 μ M; IC₅₀(Cu-NOTA-PSBP-6) = 23 μ M. Again, however, the different methods for measuring PS binding affinity of PSBP-6 as well as a lack of internal reference (i.e. annexin V) used in the SPR assay used by Xiong and colleagues makes it difficult to compare the results obtained from both PS-binding assays. It is also important to note that our competitive PS binding assay cannot determine whether PS binding of each peptide is a Ca²⁺-independent or Ca²⁺-dependent process, since adequate Ca²⁺ levels are

required in the assay in order for the competitive tracer, ^{64}Cu -NOTA-annexin V, to function.

In order to investigate these PS-binding peptides as PS-targeting PET imaging probes, we developed protocols for radiolabelling them with positron-emitting isotopes. Hexapeptides LIKKPF and PGDLSR were labelled with ^{18}F , which is the most commonly used radionuclide in clinical PET imaging due to its favourable decay properties ($t_{1/2} = 110$ min; β^+ -decay = 97%; electron capture = 3%; maximum positron energy = 0.63 MeV)¹²⁰. In addition to giving a relatively low radiation dose to the patient, the high positron emission and low positron energy of ^{18}F produce good quality images, while the moderate half-life allows for short imaging procedures while still allowing time for radiolabelling procedures. A report by Kapyt et al. describes a thiol-targeted approach to labelling these peptides by modifying the N-terminus with a cysteine residue, which they then labelled with maleimide-containing prosthetic group [^{18}F]FBAM¹⁵¹. They attempted to radiolabel LIKKPF and PGDLSR on their N-termini using the more common prosthetic group [^{18}F]SFB, carrying out the reaction in Kolthoff buffer (pH 8.4) at 40 °C for 40 min. [^{18}F]FB-LIKKPF and [^{18}F]FB-PGDLSR were obtained in radiochemical yields of 18% and 19%, respectively. However, they could not recover the purified products by HPLC due to the presence of many different labelled products with similar retention times. In the present study, we were able to isolate purified [^{18}F]FB-LIKKPF and [^{18}F]FB-PGDLSR with improved radiochemical yields of 25% and 36%, respectively. In contrast to the procedure by Kapyt et al. that labelled unprotected LIKKPF in solution with [^{18}F]SFB, we used an on-resin labelling approach¹⁷⁷ for labelling LIKKPF on solid support with protection of the two lysine residues that contain

NHS-reactive amino groups that can be labelled by [^{18}F]SFB (figure 23). In this way we were able to achieve chemoselective labelling at the N-terminus and prevented the formation of multiple labelled products. We labelled PGDLSR with [^{18}F]SFB in Na_2HPO_4 buffer (pH 9) at 60 °C for 45 min (figure 22), and were able to recover a relatively stable product in solution in contrast to the product identified by Kapyt et al, which rapidly degraded before it could be isolated¹⁵¹.

We also successfully radiolabelled 14-mer PSBP-6 with ^{18}F . We were unable to obtain an [^{18}F]SFB-labelled product that was singly labelled on its N terminus due to the presence of many [^{18}F]SFB-reactive side chains present on PSBP-6. The on-resin labelling approach was not appropriate for radiolabelling PSBP-6, as the steric hindrance induced by the bulky protecting groups needed for this method resulted in negligible yields. Instead we employed the thiol-targeted approach using [^{18}F]FBAM as prosthetic group to target the cysteine residue we added to the N terminus of the peptide, obtaining moderate radiochemical yields of 41% (figure 24). However, the resulting peptide [^{18}F]FBAM-C-PSBP-6 was very difficult to handle, as it strongly adsorbed to the surface of any container it was in. We did not further evaluate or characterize this peptide, but instead shifted our attention to radiolabelling PSBP-6 with other popular positron-emitters.

While use of ^{18}F -containing prosthetic groups results in long, multi-step procedures often resulting in mediocre radiochemical yields, ^{64}Cu and ^{68}Ga labelling can be easily carried out in one-pot procedures resulting in extremely high yields using only microgram amounts of precursor peptide¹⁷⁶. Conjugation of a peptide N terminus with a metal chelator, commonly a macrocyclic chelator due to better *in vivo* stability¹⁷⁸,

provides a peptide precursor that can then be complexed with a radiometal in one step. In the past, 1,4,7,10-tetraazacyclododecane-1,4,7,10-tetraacetic acid (DOTA) has commonly been used for radiometal labelling, since diagnostic radiometals complexed by DOTA can be substituted for therapeutic radiometals such as ^{90}Y or ^{177}Lu ¹⁷⁹. However, NOTA is now preferable for labelling of peptides with ^{68}Ga and ^{64}Cu due to its rapid reaction kinetics under milder reaction conditions, high yields, and production of radiopeptides with improved targeting, better *in vivo* kinetics and better quality images^{176,180–182}. The chelate complex of ^{64}Cu -DOTA peptides has been shown to be unstable *in vivo*, with gradual release of ^{64}Cu from DOTA resulting in accumulation of ^{64}Cu in the liver^{183,184}. A report by Prasanphanich and colleagues showed that labelling bombesin (BBN) peptide analogs with ^{64}Cu using NOTA as chelator resulted in a targeting vector with little demetallation compared to ^{64}Cu -DOTA labelled BBN tracers, resulting in less accumulation in the liver¹⁸⁴. With these considerations, we chose NOTA as our chelator for labelling PSBP-6 with ^{68}Ga and ^{64}Cu .

Using ^{68}Ga ($t_{1/2} = 68$ min; β^+ -decay = 89%; electron capture = 11%; maximum positron energy = 1.9 MeV) to label peptides for PET imaging offers the advantage of easy and inexpensive access over cyclotron-produced radionuclides, since it can be produced in a small, in-house generator. Its short half-life is often appropriate for short-lived peptide probes; however, its high positron energy results in lower resolution images and higher radiation dose to the patient¹⁸⁵. We were able to label 20 nmol of NOTA-conjugated PSBP-6 with ^{68}Ga in fairly high yields of 63% within 25 min, although an elevated temperature of 60 °C was required to obtain these yields (figure 25). Reports for labelling NOTA-conjugated RGD- or BBN-based peptides with ^{68}Ga used 5-10 nmol of

precursor to obtain radiochemical yields of greater than 90% after 10 min at lower temperatures (room temperature to 40 °C)^{181,186,187}. However, apart from differences in peptide sequence, these other reports differ from our study in that they used ⁶⁸Ga eluted in 0.1 M HCl from a ⁶⁸Ge/⁶⁸Ga generator, while our in-house generator eluted ⁶⁸Ga in 1 M HCl and required 4 M NaOAc buffer (pH 9) to achieve a reaction pH of 3.5.

⁶⁴Cu ($t_{1/2} = 12.7$ h; β^+ -decay = 17.4%; β^- -decay = 38.5%; electron capture, 43%; maximum positron energy = 0.66 MeV) can be produced by a cyclotron in large quantities and at high specific activity, and its longer half-life of 12.7 h may be desirable if longer radiolabelling and imaging procedures are required. While its decay characteristics are not ideal due to the low positron emission and high β^- -decay resulting in higher radiation doses to patients, its positron energy is similar to that of ¹⁸F, producing high quality PET images¹⁸⁵. In comparison to ⁶⁸Ga-NOTA-PSBP-6, we were able to label NOTA-PSBP-6 with ⁶⁴Cu using even less precursor, and we obtained much higher radiochemical yields (figure 26). Labelling 1 nmol of NOTA-PSBP-6 with ⁶⁴Cu at 60 °C for 1 h resulted in the highest radiochemical yields of > 95%, and thus a purification step was not necessary. Another report for labelling RGD- and BBN-based peptides with ⁶⁴Cu used 5 nmol of precursor with NaOAc as buffer instead of NH₄OAc, reacted at 40 °C for only 15 min and were able to obtain yields of greater than 90%, with the products being cartridge- or HPLC-purified^{182,186}. However, when dealing with ⁶⁴Cu, short radiolabelling times are not as important as they are for ⁶⁸Ga labelling procedures, because the decay half-life of ⁶⁴Cu is much longer than the half life of ⁶⁸Ga.

When we examined the ability of ⁶⁴Cu-NOTA-PSBP-6 to detect cell death *in vitro*, we found that, similar to [¹⁸F]SFB-annexin V, ⁶⁴Cu-NOTA-PSBP-6 showed low

baseline binding to control EL4 cells (figure 31). In the absence and the presence of Ca^{2+} , this binding significantly increased upon treatment with camptothecin 1.5-fold and 2-fold, respectively. This observed increase is less than the 4-fold increase we observed for ^{18}F -labelled annexin V (both randomly- and site specifically-labelled forms), which is compatible with our knowledge that nonradioactive Cu-NOTA-PSBP-6 has a much lower affinity for PS than annexin V, as shown by our competitive PS binding assay. Xiong et al. examined binding of SPECT agent $^{99\text{m}}\text{Tc}$ -SAAC-PSBP-6 to DLD1 human colon carcinoma cells treated with increasing doses of tumor necrosis factor-related apoptosis-inducing ligand (TRAIL), and found that as they increased the dose of TRAIL, binding of $^{99\text{m}}\text{Tc}$ -SAAC-PSBP-6 increased¹⁴⁶. Although direct comparison of these *in vitro* results between $^{99\text{m}}\text{Tc}$ -SAAC-PSBP-6 and ^{64}Cu -NOTA-PSBP-6 is difficult since the peptides were analyzed using different *in vitro* models of cell death, both results agree that radiolabelled PSBP-6 can detect chemotherapy-induced tumour cell death.

Our EL4 cell binding assay results show that ^{64}Cu -NOTA-PSBP-6 can detect cell death in the absence of Ca^{2+} , as the increase in ^{64}Cu -NOTA-PSBP-6 binding using Ca^{2+} negative binding buffer was significantly higher in cells treated with camptothecin compared to control cells. We saw a significantly higher increase in ^{64}Cu -NOTA-PSBP-6 binding to treated cells when supplemented with 2.5 mM of Ca^{2+} , which does not entirely agree with the report by Xiong et al. that there was no significant difference in Re-SAAC-PSBP-6 binding to PS in the presence or absence of Ca^{2+} . However, Xiong et al. used an SPR assay (monitoring changes in annexin V binding to PS-coated L1 sensor chips) to determine this Ca^{2+} independence rather than a cell binding assay, which might have caused this different result. Another possible explanation for the observed

discrepancy might be the partial coordination of bivalent $^{64}\text{Cu}^{2+}$ with two of the three carboxylate anions available for coordination on NOTA, which leaves one negatively charged anion free. While there is no net negative charge on $^{99\text{m}}\text{Tc}/\text{Re}\text{-SAAC-PSBP-6}$, the negative charge on $^{64}\text{Cu}\text{-NOTA-PSBP-6}$ might slightly interfere with binding of this radiopeptide to anionic PS due to electrostatic resistance. However, if Ca^{2+} ions are present, these might be recruited to the negatively charged $^{64}\text{Cu}\text{-NOTA}$ complex through electrostatic interactions, which would neutralize the net negative charge and thus reduce the electrostatic resistance between $^{64}\text{Cu}\text{-NOTA-PSBP-6}$ and PS, enhancing the binding interactions. This idea is compatible with the similar IC_{50} values we obtained for NOTA-PSBP-6 , $\text{Ga}\text{-NOTA-PSBP-6}$ and $\text{Cu}\text{-NOTA-PSBP-6}$ in our competitive PS-binding assay, which was supplemented with Ca^{2+} (due to the use of annexin V as competitor). Although each of these three peptide conjugates have different degrees of net electrostatic charges, which seemingly would result in different binding affinities to the negatively charged phospholipid PS, the neutralization of the negative charges with Ca^{2+} ions might minimize the effect of the net charges on PS binding ability. Nonetheless, the ability of $^{64}\text{Cu}\text{-NOTA-PSBP-6}$ to detect cell death in the absence of Ca^{2+} represents a significant advantage of this PS-targeting peptide over annexin V for imaging cell death. In fact, the blood plasma of animals normally contains low levels of Ca^{2+} , which would seemingly enhance the binding of $^{64}\text{Cu}\text{-NOTA-PSBP-6}$ to dying cells *in vivo*.

When we evaluated tumour uptake of $^{64}\text{Cu}\text{-NOTA-PSBP-6}$ in our EL4 tumour model, we observed a small baseline uptake of the radiopeptide in control tumours as expected (0.74 SUV), similar to the baseline tumour uptake of $[^{18}\text{F}]\text{SFB-annexin V}$ we saw at 10 min p.i. (0.77 SUV). However, unlike $[^{18}\text{F}]\text{SFB-annexin V}$, which remained

trapped in the tumour once it had accumulated, tumour uptake of the radiopeptide was quickly followed by a rapid washout (figures 32, 33 and 34). Thus, binding of the radiopeptide to PS-expressing tumor cells seems to be a fast and reversible process, in contrast to the higher-affinity, irreversible binding of annexin V. One day after treatment with the chemotherapeutic mixture of cyclophosphamide (100 mg/kg) and etoposide (76 mg/kg), EL4 tumour uptake of ^{64}Cu -NOTA-PSBP-6 increased 1.3-fold compared to control tumours, which was seen at 5 min p.i. These *in vivo* results agree with our *in vitro* data, which showed a baseline binding of the radiopeptide in control EL4 cells as well as a significant increase in binding to EL4 cells treated with a chemotherapeutic agent, and binding of the peptide was fast, with equilibrium being reached almost immediately upon addition of the radiopeptide.

The increase in tumour uptake of ^{64}Cu -NOTA-PSBP-6 that we observed in treated EL4 tumours at 5 min p.i. is supported by results seen in other tumour models of apoptosis using radiolabelled PSBP-6 as radiotracer. Song et al. evaluated $^{99\text{m}}\text{Tc}$ -SAAC-PSBP-6 uptake into 38C13 lymphoma tumours treated with a single dose of cyclophosphamide (100 mg/kg), and found a 2-fold increase in tumour uptake of $^{99\text{m}}\text{Tc}$ -SAAC-PSBP-6. They also found that uptake of $^{99\text{m}}\text{Tc}$ -SAAC-PSBP-6 into B16/F10 melanoma tumours treated with a single dose of paclitaxel (80 mg/kg) was 2.5-fold higher compared to control tumours. In addition, the biodistribution study carried out by Xiong et al. showed a 2.6-fold increase in B16/F10 melanoma tumour uptake of SAAC($^{99\text{m}}\text{Tc}$)-PSBP-6 upon treatment with paclitaxel¹⁴⁶. The higher reported increases in uptake of SAAC($^{99\text{m}}\text{Tc}$)-PSBP-6 in these other tumour models compared to the smaller increase in ^{64}Cu -NOTA-PSBP-6 (1.3-fold) that we saw in our model can be attributed to

the very different tumour models and treatments used. Some of the challenges incurred by the EL4 tumour model when evaluating [^{18}F]SFB-annexin V as cell death-detecting radiotracer might still apply when ^{64}Cu -NOTA-PSBP-6 is used as tracer. The time at which we imaged the tumours post-treatment may not have corresponded to the time of greatest PS exposure, which would result in less of a tumour uptake response.

The observed increase in uptake of ^{64}Cu -NOTA-PSBP-6 in the EL4 model after just one day of treatment, which we did not see with [^{18}F]SFB-annexin V, might have been achieved due to the higher tissue penetrating ability that peptides have as an advantage over larger proteins such as annexin V, particularly in tumours with poor blood supply and high interstitial fluid pressure. Differences in calcium dependency between PSBP-6 and annexin V may also have contributed to the discrepancy in imaging results we observed when imaging cyclophosphamide/etoposide-induced EL4 tumour cell death using ^{64}Cu -NOTA-PSBP-6 and [^{18}F]SFB-annexin V. Previous reports show that binding of PSBP-6 to PS is a calcium-independent process¹⁴⁶, and our *in vitro* results confirm that ^{64}Cu -NOTA-PSBP-6 can detect cell death in the absence of Ca^{2+} . However, this ability might be enhanced by the presence of Ca^{2+} (possibly at physiological concentrations present in the EL4 tumours). On the other hand, annexin V cannot bind PS at all in the absence of Ca^{2+} , and this Ca^{2+} dependency combined with its poor perfusion into tumour tissues might explain why we failed to see any change in [^{18}F]SFB-annexin V uptake into EL4 tumours, particularly if we did not image at the time of greatest PS exposure.

In order for peptide-based radiotracers to be suitable for molecular imaging, they must demonstrate good metabolic stability *in vivo*, as this allows the radiopeptide to remain intact in the blood and accumulate in the target tissue at sufficient

concentrations¹⁸⁸. This is because most peptides are rapidly degraded by endogenous peptidases in the plasma or by a rapid first pass metabolism by liver enzymes^{189,190}. Burtea et al. hypothesized that LIKKPF would be more stable than PGDLSR based on their structures. When we carried out *in vivo* stability studies using [¹⁸F]FB-PGDLSR and [¹⁸F]FB-LIKKPF, we indeed found that [¹⁸F]FB-LIKKPF was slightly more stable; however, both radiopeptides showed very poor *in vivo* stability. [¹⁸F]FB-LIKKPF was completely degraded after 30 minutes in the plasma, while [¹⁸F]FB-PGDLSR was almost undetectable (3% intact) in the plasma after just 5 min p.i. These radiopeptides showed even worse stability than their [¹⁸F]FBAM-labelled derivatives, [¹⁸F]FBAM-CLIKKPF and [¹⁸F]FBAM-CPGDLSR, which were developed by Kapy et al^{151,157}. Wuest and colleagues reported that less than 30% of [¹⁸F]FBAM-CLIKKPF and only marginal amounts of [¹⁸F]FBAM-CPGDLSR remained in the mouse plasma after 15 min¹⁵⁷. The poor *in vivo* stability of [¹⁸F]FB-PGDLSR and [¹⁸F]FB-LIKKPF in addition to their low PS binding affinities determined by the competitive radiometric PS-binding assay lead us to cease further efforts to “fine-tune” these peptides for PET imaging of cell death and focus our attention on the more promising 14-mer peptide, PSBP-6.

⁶⁸Ga-NOTA-PSBP-6 showed good metabolic stability *in vivo*, as HPLC analysis showed minimal radiolysis breakdown products over 60 min (figure 27). The C terminus of PSBP-6 used in this study has been end-capped through conversion of the carboxylic acid to an amide, which prevents metabolism by exopeptidases that target the C terminus¹⁹¹. This likely contributes to the radiopeptide’s good metabolic stability, in addition to the good thermodynamic stability of the Ga(III) triaza complex with NOTA, which minimizes instability due to radiometal release from the chelator^{192–194}. The

preferential distribution of ^{68}Ga -NOTA-PSBP-6 into the blood plasma rather than blood cells or proteins (figure 28) can be explained by its moderately hydrophilic nature, shown by our obtained $\log D_{7.4}$ value of -1.7. ^{64}Cu -NOTA-PSBP-6 was also shown to be moderately hydrophilic with a $\log D_{7.4}$ value of -1.6, and showed a similar blood distribution pattern to ^{68}Ga -NOTA-PSBP-6, although a greater proportion of ^{64}Cu -NOTA-PSBP-6 was found to bind to blood cells (figure 30). Since circulating blood cells gradually expose PS as they age, some binding of radiolabelled PSBP-6 to blood cells can be reasonably expected⁵³. Like ^{68}Ga -NOTA-PSBP-6, ^{64}Cu -NOTA-PSBP-6 showed much higher *in vivo* stability than ^{18}F -labelled hexapeptides [^{18}F]FB-PGDLSR and [^{18}F]FB-LIKKPF (figure 29). Other groups have reported good *in vivo* stability for ^{64}Cu -NOTA-labelled peptide derivatives, confirming that the ^{64}Cu -NOTA chelate complex is quite stable *in vivo* with respect to demetallation¹⁸⁴. Interestingly, however, ^{64}Cu -NOTA-PSBP-6 seems to be less stable *in vivo* compared to the similar radiopeptide ^{68}Ga -NOTA-PSBP-6, with only $31 \pm 11\%$ intact radiopeptide after 60 min in the plasma. This lower stability of ^{64}Cu -NOTA-PSBP-6 compared to ^{68}Ga -NOTA-PSBP-6 might be partially due to the higher chelating ability of NOTA for ^{68}Ga compared to ^{64}Cu , resulting in a more stable complex for ^{68}Ga -NOTA-PSBP-6 and thus less possibility for release of the radiometal¹⁹³. Endogenous metal binding proteins/peptides in the plasma may also have a preference for ^{64}Cu over ^{68}Ga , which compete with NOTA resulting in transchelation of the metal into the plasma protein/peptide¹⁷⁸. This finding of lower *in vivo* stability combined with the binding of ^{64}Cu -NOTA-PSBP-6 to blood proteins, which reduces its plasma availability for tumour binding/uptake, likely contributes to the overall low uptake levels of ^{64}Cu -NOTA-PSBP-6 in EL4 tumours over the observed 60 min time

frame. In addition, high levels of radioactivity were present in a urine sample taken 60 min p.i., which suggests extensive renal clearance from the blood.

Taken together, the lower affinity binding of ^{64}Cu -NOTA-PSBP-6 combined with *in vivo* degradation and rapid clearance from the blood might all explain the short-lived tumour uptake of this radiopeptide in the EL4 tumour model. Efforts to improve the plasma stability of ^{64}Cu -NOTA-PSBP-6 could be the subject of future work. This would involve identification of the cleavage sites on the peptide and characterization of metabolites, which would allow for modification of the peptide to prevent proteolytic cleavage by endopeptidases and enhance *in vivo* stability¹⁹⁵. Once cleavage sites are identified, amino acids at the cleavage site can be substituted with non-natural or modified amino acids that cannot be recognized or cleaved by peptidases, such as D-amino acids, *N*-methylated amino acids, or statine^{196–198}. Substitution of peptide bonds for pseudo-peptide bonds can also shield a peptide from peptidases, and glycosylation or cyclization might stabilize a peptide as well^{199,200}. Another technique for improving metabolic stability *in vivo* has recently been reported, which involves coadministration of an enzyme inhibitor, such as the endopeptidase inhibitor phosphoramidon, with the radiopeptide in order to reduce proteolytic degradation by that enzyme¹⁹⁰.

In order to image PSBP-6 binding to EL4 cells and examine this peptide's potential as a fluorescent marker of cell death *in vitro*, we labelled PSBP-6 with the fluorescent molecule FITC. The 2-fold increase in proportion of EL4 cells stained with FITC-PSBP-6 upon treatment with camptothecin (figure 35), which was observed in the absence of Ca^{2+} , agrees with the 1.5- to 2-fold increase in ^{64}Cu -NOTA-PSBP-6 binding we observed in our radiometric cell binding assay in the absence and presence of Ca^{2+} ,

respectively. These studies further confirm the ability of PSBP-6 to bind to chemotherapy-treated, PS-exposing EL4 cells in a Ca^{2+} -independent manner. Xiong et al. labelled their nonradioactive peptide, Re-SAAC-PSBP-6, with 5-carboxyfluorescein (FAM), and measured its ability to stain DLD1 human colon carcinoma cells that had been treated with TRAIL to induce greater than 50% apoptosis¹⁴⁶. They observed a 3.4-fold increase in cells stained with FAM-Re-SAAC-PSBP-6 (from 18% to 62% of cells) upon treatment with TRAIL. However, 20 μM of FAM-Re-SAAC-PSBP-6 was used to incubate the cells for their fluorescence studies, whereas we used a concentration of 1 μM of FITC-PSBP-6 for our fluorescence studies in order to induce more specific (albeit less) binding of the fluorescent peptide.

Our fluorescence microscopy images revealed that FITC-PSBP-6 binds to the cell membrane of early apoptotic EL4 cells, but is not internalized (figure 36). This is in accordance with the fluorescence microscopy images obtained by Xiong et al. using FAM-Re-SAAC-PSBP-6 as a cell death-detecting probe, which showed that FAM-Re-SAAC-PSBP-6 bound to the cell membrane as well, and was not internalized¹⁴⁶. The use of a caspase-3 probe, NucView 405 Caspase-3 Substrate, was used as a co-stain in order to identify apoptotic cells. Cells with intact membranes (not stained by PI) that were stained by the caspase-3 probe also showed staining by FITC-PSBP-6 on the membrane, confirming that FITC-PSBP-6 was binding to the membranes of early apoptotic cells. Cells that were very heavily stained and seemed to internalize FITC-PSBP-6 were also heavily stained with PI, thus showing that the cell membrane was not intact and the cell was necrotic or in the late stages of apoptosis.

The results of our flow cytometry and confocal microscopy studies indicate that FITC-PSBP-6 can be used to detect and image camptothecin-induced cell death *in vitro*, by binding to the membranes of early apoptotic cells as well as being taken up by late apoptotic/necrotic cells. In the past, it was accepted that internalization was an essential characteristic of radiopeptides to allow accumulation and retention in tissues^{188,201}. However, more recent studies have suggested that internalization may not be necessary for sufficient tumour uptake of a radiotracer. High-affinity G-protein coupled receptor (GPCR) antagonists that are not internalized have shown improved tumour uptake, binding and retention compared to internalized GPCR agonists due to more available receptor binding sites²⁰²⁻²⁰⁴. The abundance of PS available on apoptotic cells (50-200 million PS molecules externalized on an apoptotic cell²⁰⁵) may make internalization of PSBP-6 unnecessary for sufficient uptake into apoptotic tumour tissue. We found that, *in vivo*, uptake of PS-binding radiopeptide ⁶⁴Cu-NOTA-PSBP-6 into treated EL4 tumours is increased compared to control tumours, probably due to a combination of ⁶⁴Cu-NOTA-PSBP-6 binding to the membranes of early apoptotic cells as well as entrance of the peptide into necrotic/late apoptotic cells. The poor retention of ⁶⁴Cu-NOTA-PSBP-6 in EL4 tumours can be explained by its rather low binding affinity (IC₅₀ = 23 μM), which is exacerbated by degradation in the plasma, blood cell binding, and fast blood clearance of the radiopeptide. However, in addition to improving the *in vivo* stability of ⁶⁴Cu-NOTA-PSBP-6 through modification of the peptide or coadministration of a peptidase inhibitor,

efforts to improve the radiopeptide's PS-binding affinity, blood clearance profile and retention in tumours can also be made²⁰⁶.

5. CONCLUSIONS and FUTURE DIRECTIONS

In this study, we have shown that in addition to the previously reported method for randomly labelling wild-type annexin V on its 23 primary amines, wild-type annexin V can also be site-selectively labelled with ^{18}F on its single, naturally-occurring cys315 residue. Although site-selectively labelled ^{18}F -annexin V has similar PS-binding ability to randomly-labelled ^{18}F -annexin V, the more complex radiolabelling procedure as well as the very low radiochemical yields obtained limits further application of the site-selective technique.

Despite previous reports that [^{18}F]SFB-annexin V can effectively detect tumour response to treatment in other tumour models of cell death, [^{18}F]SFB-annexin V failed to detect EL4 lymphoma tumour response to treatment with cyclophosphamide and etoposide in mice. This may be due to poor penetration of ^{18}F -annexin V into the EL4 tumours, lack of sufficient Ca^{2+} concentrations in *in vivo* EL4 tumours, lack of imaging during the time of greatest PS exposure, or any combination of these factors. Optimization of this EL4 tumour model might be necessary in order to find the time of maximum PS exposure after treatment during which to image. Optimization may include lessening the dose and/or imaging at more time points post-treatment. Otherwise, a completely different tumour model of therapy-induced cell death might be useful for preclinical PET imaging with [^{18}F]SFB-annexin V. Nonetheless, these results have important implications that the utility of radiolabelled annexin V for imaging tumour response to treatment is variable based on tumour characteristics and treatment protocol.

14-mer peptide PSBP-6, on the other hand, appears to be a promising alternative to annexin V for PET imaging of tumour response to chemotherapy. PSBP-6 offers advantages over annexin V for *in vivo* imaging, as it has better tissue penetration due to its smaller size, and it does not require Ca^{2+} for binding to PS, as determined by our cell binding assays. PSBP-6 is simple and inexpensive to produce, whereas annexin V is quite expensive and less readily available. Procedures for radiolabelling PSBP-6 with positron emitting radionuclides were much easier and resulted in markedly better radiochemical yields than procedures for radiolabelling annexin V. Preclinical PET images showed that ^{64}Cu -NOTA-PSBP-6 uptake into EL4 tumours significantly increased after treatment with cyclophosphamide and etoposide. However, this uptake occurred quickly within 5 minutes, after which the radiopeptide was rapidly washed out and any differences between control and treated tumours were no longer visible. This poor tumour retention is likely due to the low binding affinity of ^{64}Cu -NOTA-PSBP-6 we determined from our radiometric competitive PS binding assay ($\text{IC}_{50} = 23 \mu\text{M}$), the partial binding of the radiopeptide to blood cells, which reduces its plasma availability, as well as the observed poor metabolic stability and apparent rapid clearance of this radiopeptide *in vivo*. However, a major advantage of using peptide-based probes for the development of molecular imaging agents is that peptides can be modified to improve their pharmacokinetic and pharmacodynamic properties.

As outlined previously, the metabolic stability of peptides can be improved by substitution of non-natural amino acids or pseudo-peptide bonds that cannot be

recognized or cleaved by proteolytic enzymes present in the plasma, or by coadministration of a peptidase inhibitor^{190,195,196,198,199}. In addition, peptides can be stabilized by glycosylation or cyclization²⁰⁰. The blood half-life of a peptide can also be increased by the addition of polyethylene glycol (PEG) polymer chains to the peptide termini, called PEGylation, which increases the molecular mass of the peptide and protects it from peptidase activity^{200,207}. In order to improve the affinity or potency of a peptide, the linker between chelator and peptide can be altered. For example, Parry et al. showed that switching from a short linker like Ava to a longer linker like aminooctanoic acid (Aoc) on a ⁶⁴Cu-DOTA-BBN derivative significantly increased the binding potency of this peptide, possibly due to less interference of the radiolabel with binding interactions between the peptide and its receptor²⁰⁸. Peptide potency can also be increased via the multivalent effect, which can be achieved by synthesis of branched, multivalent peptides (dendrimers) or by conjugation of many peptides to nanoparticles²⁰⁹⁻²¹¹.

Synthesis of a branched molecule or nanoparticle containing several PSBP-6 peptides would provide several PS-binding sites per probe molecule, which enhance the affinity of the molecule for PS, an amplified signal at the target area, as well as improved stability/pharmacokinetics and targeting efficiency of the probe. The use of nanoparticles could also increase specificity by reducing nonspecific binding²¹¹. Finally, peptides that show poor internalization, such as PSBP-6, can be coupled to cell-penetrating peptides, such as cathelicidin-derived peptide sC18, in order to facilitate internalization into the cell and possibly enhance tumour retention of the peptide probe²¹². Once the peptide can internalize, it can be conjugated with another molecule that binds to an intracellular

target, termed dual-conjugate targeting, which might enhance retention in the cell²¹³. Future work should involve these types of modifications in order to improve the binding affinity, metabolic stability, and blood clearance of ⁶⁴Cu-NOTA-PSBP-6, which might improve tumour retention and thus imaging ability of this radiopeptide.

6. REFERENCES

1. Kalia M. Personalized oncology: recent advances and future challenges. *Metabolism*. 2013;62 Suppl 1:S11-S14. doi:10.1016/j.metabol.2012.08.016.
2. Huang M, Shen A, Ding J, Geng M. Molecularly targeted cancer therapy: some lessons from the past decade. *Trends Pharmacol Sci*. 2014;35(1):41-50. doi:10.1016/j.tips.2013.11.004.
3. Gerlinger M, Rowan AJ, Horswell S, et al. Intratumor heterogeneity and branched evolution revealed by multiregion sequencing. *N Engl J Med*. 2012;366(10):883-892. doi:10.1056/NEJMoa1113205.
4. Bardin C, Veal G, Paci A, et al. Therapeutic drug monitoring in cancer--are we missing a trick? *Eur J Cancer*. 2014;50(12):2005-2009. doi:10.1016/j.ejca.2014.04.013.
5. Harry VN, Semple SI, Parkin DE, Gilbert FJ. Use of new imaging techniques to predict tumour response to therapy. *Lancet Oncol*. 2010;11(1):92-102. doi:10.1016/S1470-2045(09)70190-1.
6. Husband JE, Schwartz LH, Spencer J, et al. Evaluation of the response to treatment of solid tumours - a consensus statement of the International Cancer Imaging Society. *Br J Cancer*. 2004;90(12):2256-2260. doi:10.1038/sj.bjc.6601843.
7. Padhani AR. Functional MRI for anticancer therapy assessment. *Eur J Cancer*. 2002;38(16):2116-2127. <http://www.ncbi.nlm.nih.gov/pubmed/12387837>. Accessed July 3, 2015.
8. Thiesse P, Ollivier L, Di Stefano-Louineau D, et al. Response rate accuracy in oncology trials: reasons for interobserver variability. Groupe Français d'Immunothérapie of the Fédération Nationale des Centres de Lutte Contre le Cancer. *J Clin Oncol*. 1997;15(12):3507-3514. <http://www.ncbi.nlm.nih.gov/pubmed/9396404>. Accessed July 4, 2015.
9. Toretzky J, Levenson A, Weinberg IN, Tait JF, Üren A, Mease RC. Preparation of F-18 labeled annexin V: A potential PET radiopharmaceutical for imaging cell death. *Nucl Med Biol*. 2004;31(6):747-752. doi:10.1016/j.nucmedbio.2004.02.007.

10. Smith TA. FDG uptake, tumour characteristics and response to therapy: a review. *Nucl Med Commun.* 1998;19(2):97-105. <http://www.ncbi.nlm.nih.gov/pubmed/9548192>. Accessed July 4, 2015.
11. Pickles MD, Gibbs P, Lowry M, Turnbull LW. Diffusion changes precede size reduction in neoadjuvant treatment of breast cancer. *Magn Reson Imaging.* 2006;24(7):843-847. doi:10.1016/j.mri.2005.11.005.
12. Junttila MR, de Sauvage FJ. Influence of tumour micro-environment heterogeneity on therapeutic response. *Nature.* 2013;501(7467):346-354. doi:10.1038/nature12626.
13. Zeng W, Wang X, Xu P, Liu G, Eden HS, Chen X. Molecular imaging of apoptosis: from micro to macro. *Theranostics.* 2015;5(6):559-582. doi:10.7150/thno.11548.
14. Gambhir SS. Molecular imaging of cancer with positron emission tomography. *Nat Rev Cancer.* 2002;2(9):683-693. doi:10.1038/nrc882.
15. Weissleder R, Pittet MJ. Imaging in the era of molecular oncology. *Nature.* 2008;452(7187):580-589. doi:10.1038/nature06917.
16. Li Z, Conti PS. Radiopharmaceutical chemistry for positron emission tomography. *Adv Drug Deliv Rev.* 2010;62(11):1031-1051. doi:10.1016/j.addr.2010.09.007.
17. Saad FFA. *Selected Topics on Computed Tomography.* Vol (Wang D, ed.). InTech; 2013. doi:10.5772/45935.
18. Juweid ME, Cheson BD. Positron-emission tomography and assessment of cancer therapy. *N Engl J Med.* 2006;354(5):496-507. doi:10.1056/NEJMra050276.
19. Zhang C, Tong J, Sun X, Liu J, Wang Y, Huang G. 18F-FDG-PET evaluation of treatment response to neo-adjuvant therapy in patients with locally advanced rectal cancer: a meta-analysis. *Int J Cancer.* 2012;131(11):2604-2611. doi:10.1002/ijc.27557.
20. Godoy A, Ulloa V, Rodríguez F, et al. Differential subcellular distribution of glucose transporters GLUT1-6 and GLUT9 in human cancer: ultrastructural localization of GLUT1 and GLUT5 in breast tumor tissues. *J Cell Physiol.* 2006;207(3):614-627. doi:10.1002/jcp.20606.
21. Trigonis I, Jackson A. Imaging pharmacodynamics in oncology: the potential significance of “flares”. *Ann Nucl Med.* 2010;24(3):137-147. doi:10.1007/s12149-009-0332-7.

22. Wahl RL, Jacene H, Kasamon Y, Lodge MA. From RECIST to PERCIST: Evolving Considerations for PET response criteria in solid tumors. *J Nucl Med*. 2009;50 Suppl 1(Suppl_1):122S - 50S. doi:10.2967/jnumed.108.057307.
23. Willmann JK, van Bruggen N, Dinkelborg LM, Gambhir SS. Molecular imaging in drug development. *Nat Rev Drug Discov*. 2008;7(7):591-607. doi:10.1038/nrd2290.
24. Padhani AR, Miles KA. Multiparametric imaging of tumor response to therapy. *Radiology*. 2010;256(2):348-364. doi:10.1148/radiol.10091760.
25. Stafford JH, Hao G, Best AM, Sun X, Thorpe PE. Highly specific PET imaging of prostate tumors in mice with an iodine-124-labeled antibody fragment that targets phosphatidylserine. *PLoS One*. 2013;8(12):e84864. doi:10.1371/journal.pone.0084864.
26. Belhocine T, Steinmetz N, Hustinx R, et al. Increased Uptake of the Apoptosis-imaging Agent 99mTc Recombinant Human Annexin V in Human Tumors after One Course of Chemotherapy as a Predictor of Tumor Response and Patient Prognosis. *Clin Cancer Res*. 2002;8(9):2766-2774. <http://clincancerres.aacrjournals.org.login.ezproxy.library.ualberta.ca/content/8/9/2766.long>. Accessed June 26, 2015.
27. Cherry SR. Fundamentals of positron emission tomography and applications in preclinical drug development. *J Clin Pharmacol*. 2001;41(5):482-491. <http://www.ncbi.nlm.nih.gov/pubmed/11361044>. Accessed July 6, 2015.
28. Vaalburg W, Hendrikse NH, de Vries EF. Drug development, radiolabelled drugs and PET. *Ann Med*. 1999;31(6):432-437. <http://www.ncbi.nlm.nih.gov/pubmed/10680858>. Accessed July 6, 2015.
29. Saikumar P, Dong Z, Mikhailov V, Denton M, Weinberg JM, Venkatachalam MA. Apoptosis: definition, mechanisms, and relevance to disease. *Am J Med*. 1999;107(5):489-506. doi:10.1016/S0002-9343(99)00259-4.
30. Okada H, Mak TW. Pathways of apoptotic and non-apoptotic death in tumour cells. *Nat Rev Cancer*. 2004;4(8):592-603. doi:10.1038/nrc1412.
31. Burton DGA, Krizhanovsky V. Physiological and pathological consequences of cellular senescence. *Cell Mol Life Sci*. 2014;71(22):4373-4386. doi:10.1007/s00018-014-1691-3.
32. Galluzzi L, Maiuri MC, Vitale I, et al. Cell death modalities: classification and pathophysiological implications. *Cell Death Differ*. 2007;14(7):1237-1243. doi:10.1038/sj.cdd.4402148.

33. Giansanti V, Torriglia A, Scovassi AI. Conversation between apoptosis and autophagy: "Is it your turn or mine?". *Apoptosis*. 2011;16(4):321-333. doi:10.1007/s10495-011-0589-x.
34. Cavallo F, De Giovanni C, Nanni P, Forni G, Lollini PL. 2011: The immune hallmarks of cancer. In: *Cancer Immunology, Immunotherapy*. Vol 60. ; 2011:319-326.
35. Vandenabeele P, Galluzzi L, Vanden Berghe T, Kroemer G. Molecular mechanisms of necroptosis: an ordered cellular explosion. *Nat Rev Mol Cell Biol*. 2010;11(10):700-714. doi:10.1038/nrm2970.
36. Hanahan D, Weinberg RA. Hallmarks of cancer: The next generation. *Cell*. 2011;144(5):646-674.
37. Castedo M, Perfettini J-L, Roumier T, Andreau K, Medema R, Kroemer G. Cell death by mitotic catastrophe: a molecular definition. *Oncogene*. 2004;23(16):2825-2837. doi:10.1038/sj.onc.1207528.
38. Kerr J. F. R., Wyllie A. H. C a. R. Apoptosis : a Basic Biological Phenomenon With Wide-. *Br J Cancer*. 1972;26:239-257.
39. Fulda S, Debatin K-M. Extrinsic versus intrinsic apoptosis pathways in anticancer chemotherapy. *Oncogene*. 2006;25(34):4798-4811. doi:10.1038/sj.onc.1209608.
40. Hengartner MO. The biochemistry of apoptosis. *Nature*. 2000;407(6805):770-776. doi:10.1038/35037710.
41. Goping IS, Barry M, Liston P, et al. Granzyme B-induced apoptosis requires both direct caspase activation and relief of caspase inhibition. *Immunity*. 2003;18(3):355-365. <http://www.ncbi.nlm.nih.gov/pubmed/12648453>. Accessed May 17, 2015.
42. Clarke P, Tyler KL. Apoptosis in animal models of virus-induced disease. *Nat Rev Microbiol*. 2009;7(2):144-155. doi:10.1038/nrmicro2071.
43. Düssmann H, Rehm M, Kögel D, Prehn JHM. Outer mitochondrial membrane permeabilization during apoptosis triggers caspase-independent mitochondrial and caspase-dependent plasma membrane potential depolarization: a single-cell analysis. *J Cell Sci*. 2003;116(Pt 3):525-536. <http://www.ncbi.nlm.nih.gov/pubmed/12508113>. Accessed July 1, 2015.
44. Ward TH, Cummings J, Dean E, et al. Biomarkers of apoptosis. *Br J Cancer*. 2008;99(6):841-846. doi:10.1038/sj.bjc.6604519.

45. Martin SJ, Reutelingsperger CP, McGahon AJ, et al. Early redistribution of plasma membrane phosphatidylserine is a general feature of apoptosis regardless of the initiating stimulus: inhibition by overexpression of Bcl-2 and Abl. *J Exp Med*. 1995;182(5):1545-1556. doi:10.1084/jem.182.5.1545.
46. Schutters K, Reutelingsperger C. Phosphatidylserine targeting for diagnosis and treatment of human diseases. *Apoptosis*. 2010;15(9):1072-1082. doi:10.1007/s10495-010-0503-y.
47. Bitbol M, Fellmann P, Zachowski A, Devaux PF. Ion regulation of phosphatidylserine and phosphatidylethanolamine outside-inside translocation in human erythrocytes. *Biochim Biophys Acta*. 1987;904(2):268-282. <http://www.ncbi.nlm.nih.gov/pubmed/3117114>. Accessed June 26, 2015.
48. Suzuki J, Imanishi E, Nagata S. Exposure of phosphatidylserine by Xk-related protein family members during apoptosis. *J Biol Chem*. 2014;289(44):30257-30267. doi:10.1074/jbc.M114.583419.
49. Smith BA, Smith BD. Biomarkers and molecular probes for cell death imaging and targeted therapeutics. *Bioconjug Chem*. 2012;23(10):1989-2006. doi:10.1021/bc3003309.
50. Alam IS, Neves AA, Witney TH, Boren J, Brindle KM. Comparison of the C2A domain of synaptotagmin-I and annexin-V as probes for detecting cell death. *Bioconjug Chem*. 2010;21(5):884-891. doi:10.1021/bc9004415.
51. Zwaal RFA, Comfurius P, Bevers EM. Surface exposure of phosphatidylserine in pathological cells. *Cell Mol Life Sci*. 2005;62(9):971-988. doi:10.1007/s00018-005-4527-3.
52. Denecker G, Dooms H, Van Loo G, et al. Phosphatidyl serine exposure during apoptosis precedes release of cytochrome c and decrease in mitochondrial transmembrane potential. *FEBS Lett*. 2000;465(1):47-52. doi:10.1016/S0014-5793(99)01702-0.
53. Allen TM, Williamson P, Schlegel RA. Phosphatidylserine as a determinant of reticuloendothelial recognition of liposome models of the erythrocyte surface. *Proc Natl Acad Sci U S A*. 1988;85(21):8067-8071. <http://www.pubmedcentral.nih.gov/articlerender.fcgi?artid=282355&tool=pmcentrez&rendertype=abstract>. Accessed June 29, 2015.
54. Heemskerk JWM, Bevers EM, Lindhout T. Platelet activation and blood coagulation. *Thromb Haemost*. 2002;88(2):186-193. <http://www.ncbi.nlm.nih.gov/pubmed/12195687>. Accessed June 28, 2015.

55. Hamon Y, Broccardo C, Chambenoit O, et al. ABC1 promotes engulfment of apoptotic cells and transbilayer redistribution of phosphatidylserine. *Nat Cell Biol.* 2000;2(7):399-406. doi:10.1038/35017029.
56. Tait JF. Imaging of apoptosis. *J Nucl Med.* 2008;49(10):1573-1576. doi:10.2967/jnumed.108.052803.
57. Kaptj J, Murray D, Mercer J. Radiotracers for noninvasive molecular imaging of tumor cell death. *Cancer Biother Radiopharm.* 2010;25(6):615-628. doi:10.1089/cbr.2010.0793.
58. Neves A a, Brindle KM. Imaging cell death. *J Nucl Med.* 2014;55(1):1-4. doi:10.2967/jnumed.112.114264.
59. Podichetty AK, Wagner S, Schröer S, et al. Fluorinated isatin derivatives. Part 2. New N-substituted 5-pyrrolidinylsulfonyl isatins as potential tools for molecular imaging of caspases in apoptosis. *J Med Chem.* 2009;52(11):3484-3495. doi:10.1021/jm8015014.
60. Nguyen Q-D, Smith G, Glaser M, Perumal M, Arstad E, Aboagye EO. Positron emission tomography imaging of drug-induced tumor apoptosis with a caspase-3/7 specific [18F]-labeled isatin sulfonamide. *Proc Natl Acad Sci U S A.* 2009;106(38):16375-16380. doi:10.1073/pnas.0901310106.
61. Nguyen Q-D, Lavdas I, Gubbins J, et al. Temporal and spatial evolution of therapy-induced tumor apoptosis detected by caspase-3-selective molecular imaging. *Clin Cancer Res.* 2013;19(14):3914-3924. doi:10.1158/1078-0432.CCR-12-3814.
62. Witney TH, Fortt R, Fortt RR, Aboagye EO. Preclinical assessment of carboplatin treatment efficacy in lung cancer by 18F-ICMT-11-positron emission tomography. *PLoS One.* 2014;9(3):e91694. doi:10.1371/journal.pone.0091694.
63. Merchant S, Aboagye EO, Lim A, et al. Abstract P5-01-02: Evaluation of apoptosis in breast cancer using the novel PET probe [18 F]ICMT-11 in patients treated with neoadjuvant FEC chemotherapy: Initial assessment of optimum imaging time and relation to caspase-3 immunostaining. *Cancer Res.* 2015;75(9 Supplement):P5-01 - 02-P5 - 01-02. doi:10.1158/1538-7445.SABCS14-P5-01-02.
64. Madar I, Huang Y, Ravert H, et al. Detection and quantification of the evolution dynamics of apoptosis using the PET voltage sensor 18F-fluorobenzyl triphenyl phosphonium. *J Nucl Med.* 2009;50(5):774-780. doi:10.2967/jnumed.108.061283.
65. Al-Ejeh F, Darby JM, Brown MP. The La autoantigen is a malignancy-associated cell death target that is induced by DNA-damaging drugs. *Clin Cancer Res.* 2007;13(18 Pt 2):5509s - 5518s. doi:10.1158/1078-0432.CCR-07-0922.

66. Al-Ejeh F, Darby JM, Tsopelas C, Smyth D, Manavis J, Brown MP. APOMAB, a La-specific monoclonal antibody, detects the apoptotic tumor response to life-prolonging and DNA-damaging chemotherapy. *PLoS One*. 2009;4(2):e4558. doi:10.1371/journal.pone.0004558.
67. Al-Ejeh F, Staudacher AH, Smyth DR, et al. Postchemotherapy and tumor-selective targeting with the La-specific DAB4 monoclonal antibody relates to apoptotic cell clearance. *J Nucl Med*. 2014;55(5):772-779. doi:10.2967/jnumed.113.130559.
68. Al-Ejeh F, Darby JM, Pensa K, Diener KR, Hayball JD, Brown MP. In vivo targeting of dead tumor cells in a murine tumor model using a monoclonal antibody specific for the La autoantigen. *Clin Cancer Res*. 2007;13(18 Pt 2):5519s - 5527s. doi:10.1158/1078-0432.CCR-07-0964.
69. Lee M-J, Wang K, Kim I-S, Lee B-H, Han HS. Molecular imaging of cell death in an experimental model of Parkinson's disease with a novel apoptosis-targeting peptide. *Mol Imaging Biol*. 2012;14(2):147-155. doi:10.1007/s11307-011-0497-z.
70. Acharya B, Wang K, Kim I-S, Kang W, Moon C, Lee B-H. In vivo imaging of myocardial cell death using a peptide probe and assessment of long-term heart function. *J Control Release*. 2013;172(1):367-373. doi:10.1016/j.jconrel.2013.08.294.
71. Jung H-K, Wang K, Jung MK, Kim I-S, Lee B-H. In vivo near-infrared fluorescence imaging of apoptosis using histone H1-targeting peptide probe after anti-cancer treatment with cisplatin and cetuximab for early decision on tumor response. *PLoS One*. 2014;9(6):e100341. doi:10.1371/journal.pone.0100341.
72. Damianovich M, Ziv I, Heyman SN, et al. ApoSense: a novel technology for functional molecular imaging of cell death in models of acute renal tubular necrosis. *Eur J Nucl Med Mol Imaging*. 2006;33(3):281-291. doi:10.1007/s00259-005-1905-x.
73. Bao X, Yang Z, Zheng Y-J, et al. The 18F-ML10 micro-PET/CT in early predicting irradiation response of human nasopharyngeal carcinoma xenografts. *J Nucl Med*. 2014;55(supplement_1):1431 - . http://jnm.snmjournals.org/content/55/supplement_1/1431.short. Accessed July 25, 2015.
74. Wang M-W, Bao X, Zhang Y. Noninvasive Apoptosis Detection by 18F-ML10 MicroPET/CT Imaging for Early Monitoring Cancer Anti-Angiogenic Therapy Response. *J Nucl Med*. 2015;56(supplement_3):1217 - . http://jnm.snmjournals.org/content/56/supplement_3/1217.short. Accessed July 25, 2015.

75. De Saint-Hubert M, Prinsen K, Mortelmans L, Verbruggen A, Mottaghy FM. Molecular imaging of cell death. *Methods*. 2009;48(2):178-187. doi:10.1016/j.ymeth.2009.03.022.
76. Höglund J, Shirvan A, Antoni G, et al. 18F-ML-10, a PET tracer for apoptosis: first human study. *J Nucl Med*. 2011;52(5):720-725. doi:10.2967/jnumed.110.081786.
77. Allen AM, Ben-Ami M, Reshef A, et al. Assessment of response of brain metastases to radiotherapy by PET imaging of apoptosis with ¹⁸F-ML-10. *Eur J Nucl Med Mol Imaging*. 2012;39(9):1400-1408. doi:10.1007/s00259-012-2150-8.
78. Shirvan A, Reshef A, Allen A, et al. Apoptosis imaging with PET-18F-ML-10 for early assessment of response of brain metastases to radiotherapy. *Soc Nucl Med Annu Meet Abstr*. 2009;50(Supplement 2):453. http://jnumedmtg.snmjournals.org/cgi/content/meeting_abstract/50/2_MeetingAbstracts/453. Accessed July 25, 2015.
79. Oborski MJ, Laymon CM, Lieberman FS, Drappatz J, Hamilton RL, Mountz JM. First use of (18)F-labeled ML-10 PET to assess apoptosis change in a newly diagnosed glioblastoma multiforme patient before and early after therapy. *Brain Behav*. 2014;4(2):312-315. doi:10.1002/brb3.217.
80. Luo Q-Y, Zhang Z-Y, Wang F, Lu H-K, Guo Y-Z, Zhu R-S. Preparation, in vitro and in vivo evaluation of (99m)Tc-Annexin B1: a novel radioligand for apoptosis imaging. *Biochem Biophys Res Commun*. 2005;335(4):1102-1106. doi:10.1016/j.bbrc.2005.07.188.
81. Ogasawara A, Tinianow JN, Vanderbilt AN, et al. ImmunoPET imaging of phosphatidylserine in pro-apoptotic therapy treated tumor models. *Nucl Med Biol*. 2013;40(1):15-22. doi:10.1016/j.nucmedbio.2012.09.001.
82. Wyffels L, Gray BD, Barber C, et al. Synthesis and preliminary evaluation of radiolabeled bis(zinc(II)-dipicolylamine) coordination complexes as cell death imaging agents. *Bioorg Med Chem*. 2011;19(11):3425-3433. doi:10.1016/j.bmc.2011.04.029.
83. Wang H, Tang X, Tang G, et al. Noninvasive positron emission tomography imaging of cell death using a novel small-molecule probe, (18)F labeled bis(zinc(II)-dipicolylamine) complex. *Apoptosis*. 2013;18(8):1017-1027. doi:10.1007/s10495-013-0852-4.
84. Tait JF, Gibson DF, Smith C. Measurement of the affinity and cooperativity of annexin V–membrane binding under conditions of low membrane occupancy. *Anal Biochem*. 2004;329(1):112-119. doi:10.1016/j.ab.2004.02.043.

85. Yen T-C, Wey S-P, Liao C-H, et al. Measurement of the binding parameters of annexin derivative-erythrocyte membrane interactions. *Anal Biochem.* 2010;406(1):70-79. doi:10.1016/j.ab.2010.06.048.
86. Tait JF, Cerqueira MD, Dewhurst TA, Fujikawa K, Ritchie JL, Stratton JR. Evaluation of annexin V as a platelet-directed thrombus targeting agent. *Thromb Res.* 1994;75(5):491-501. doi:10.1016/0049-3848(94)90224-0.
87. Huber R, Berendes R, Burger A, et al. Crystal and molecular structure of human annexin V after refinement. Implications for structure, membrane binding and ion channel formation of the annexin family of proteins. *J Mol Biol.* 1992;223(3):683-704. <http://research.bmn.com/medline/search/record?uid=MDLN.92177413>.
88. Gerke V, Moss SE. Annexins: from structure to function. *Physiol Rev.* 2002;82(2):331-371. doi:10.1152/physrev.00030.2001.
89. Lahorte CMM, Vanderheyden J-L, Steinmetz N, Van de Wiele C, Dierckx RA, Slegers G. Apoptosis-detecting radioligands: current state of the art and future perspectives. *Eur J Nucl Med Mol Imaging.* 2004;31(6):887-919. doi:10.1007/s00259-004-1555-4.
90. Bazzi MD, Nelsestuen GL. Highly sequential binding of protein kinase C and related proteins to membranes. *Biochemistry.* 1991;30(32):7970-7977. <http://www.ncbi.nlm.nih.gov/pubmed/1868071>. Accessed June 26, 2015.
91. Corsten MF, Hofstra L, Narula J, Reutelingsperger CPM. Counting heads in the war against cancer: defining the role of annexin A5 imaging in cancer treatment and surveillance. *Cancer Res.* 2006;66(3):1255-1260. doi:10.1158/0008-5472.CAN-05-3000.
92. Koopman G, Reutelingsperger C, Kuijten G, Keehnen R, Pals S, van Oers M. Annexin V for flow cytometric detection of phosphatidylserine expression on B cells undergoing apoptosis. *Blood.* 1994;84(5):1415-1420. <http://www.ncbi.nlm.nih.gov/pubmed/12528562> \n <http://bloodjournal.hematologylibrary.org/content/84/5/1415.short>.
93. Vangestel C, Peeters M, Mees G, et al. In vivo imaging of apoptosis in oncology: An update. *Mol Imaging.* 2011;10(5):340-358. doi:10.2310/7290.2010.00058.
94. Blankenberg FG, Katsikis PD, Tait JF, et al. In vivo detection and imaging of phosphatidylserine expression during programmed cell death. *Proc Natl Acad Sci U S A.* 1998;95(11):6349-6354. [internal-pdf:/Blankenberg-1998-In vivo detection an.pdf\nhttp://www.ncbi.nlm.nih.gov/entrez/query.fcgi?cmd=Retrieve&db=PubMed&dopt=Citation&list_uids=9600968](http://www.ncbi.nlm.nih.gov/entrez/query.fcgi?cmd=Retrieve&db=PubMed&dopt=Citation&list_uids=9600968).

95. Subbarayan M, Häfeli UO, Feyes DK, Unnithan J, Emancipator SN, Mukhtar H. A simplified method for preparation of ^{99m}Tc -annexin V and its biologic evaluation for in vivo imaging of apoptosis after photodynamic therapy. *J Nucl Med.* 2003;44(4):650-656.
96. Mochizuki T, Kuge Y, Zhao S, et al. Detection of apoptotic tumor response in vivo after a single dose of chemotherapy with ^{99m}Tc -annexin V. *J Nucl Med.* 2003;44(1):92-97.
97. Takei T, Kuge Y, Zhao S, et al. Time course of apoptotic tumor response after a single dose of chemotherapy: comparison with ^{99m}Tc -annexin V uptake and histologic findings in an experimental model. *J Nucl Med.* 2004;45(12):2083-2087. doi:45/12/2083 [pii].
98. Wong E, Kumar V, Howman-Giles RB, Vanderheyden J-L. Imaging of therapy-induced apoptosis using (^{99m}Tc)-HYNIC-annexin V in thymoma tumor-bearing mice. *Cancer Biother Radiopharm.* 2008;23(6):715-726. doi:10.1089/cbr.2008.0504.
99. Lan X li, Zhang Y xue, He Y, et al. Feasibility of apoptosis-imaging agent ^{99m}Tc -HYNIC-annexin V in early assessment of chemotherapeutic effect on tumor models. *Zhonghua Zhong Liu Za Zhi.* 2008;30(10):737-740.
100. Guo M, Zhao Y, Tian R, et al. In vivo ^{99m}Tc -HYNIC-annexin V imaging of early tumor apoptosis in mice after single dose irradiation. *J Exp Clin Cancer Res.* 2009;28:136. doi:10.1186/1756-9966-28-136.
101. Erba PA, Manfredi C, Lazzeri E, et al. Time course of Paclitaxel-induced apoptosis in an experimental model of virus-induced breast cancer. *J Nucl Med.* 2010;51(5):775-781. doi:10.2967/jnumed.109.071621.
102. Beekman CAC, Buckle T, van Leeuwen AC, et al. Questioning the value of ^{99m}Tc -HYNIC-annexin V based response monitoring after docetaxel treatment in a mouse model for hereditary breast cancer. *Appl Radiat Isot.* 2011;69(4):656-662. doi:10.1016/j.apradiso.2010.12.012.
103. De Saint-Hubert M, Wang H, Devos E, et al. Preclinical imaging of therapy response using metabolic and apoptosis molecular imaging. *Mol Imaging Biol.* 2011;13(5):995-1002. doi:10.1007/s11307-010-0412-z.
104. Van de Wiele C, Lahorte C, Vermeersch H, et al. Quantitative tumor apoptosis imaging using Technetium- 99m -HYNIC annexin V single photon emission computed tomography. *J Clin Oncol.* 2003;21(18):3483-3487. doi:10.1200/JCO.2003.12.096.

105. Vermeersch H, Ham H, Rottey S, et al. Intraobserver, interobserver, and day-to-day reproducibility of quantitative ^{99m}Tc-HYNIC annexin-V imaging in head and neck carcinoma. *Cancer Biother Radiopharm*. 2004;19(2):205-210. doi:10.1089/108497804323071986.
106. Haas RL, de Jong D, Valdes Olmos RA, et al. In vivo imaging of radiation-induced apoptosis in follicular lymphoma patients. *Int J Radiat Oncol Biol Phys*. 2004;59(3):782-787. http://www.ncbi.nlm.nih.gov/entrez/query.fcgi?cmd=Retrieve&db=PubMed&dopt=Citation&list_uids=15183481.
107. Kartachova M, Van Zandwijk N, Burgers S, Van Tinteren H, Verheij M, Olmos RAV. Prognostic significance of ^{99m}Tc Hynic-rh-annexin V scintigraphy during platinum-based chemotherapy in advanced lung cancer. *J Clin Oncol*. 2007;25(18):2534-2539. doi:10.1200/JCO.2006.10.1337.
108. Rottey S, Slegers G, Van Belle S, Goethals I, Van de Wiele C. Sequential ^{99m}Tc-Hydrazinonicotinamide-Annexin V Imaging for Predicting Response to Chemotherapy. *J Nucl Med*. 2006;47(11):1813-1818. <http://jnm.snmjournals.org/login.ezproxy.library.ualberta.ca/content/47/11/1813.long>. Accessed June 26, 2015.
109. Rottey S, Loose D, Vakaet L, et al. ^{99m}Tc-HYNIC Annexin-V imaging of tumors and its relationship to response to radiotherapy and/or chemotherapy. *Q J Nucl Med Mol imaging Off Publ Ital Assoc Nucl Med [and] Int Assoc Radiopharmacol (IAR), [and] Sect Soc Radiopharm*. 2007;51(2):182-188. <http://www.ncbi.nlm.nih.gov/pubmed/17220821>. Accessed July 9, 2015.
110. Loose D, Vermeersch H, De Vos F, Deron P, Slegers G, Van De Wiele C. Prognostic value of ^{99m}Tc-HYNIC Annexin-V imaging in squamous cell carcinoma of the head and neck. *Eur J Nucl Med Mol Imaging*. 2008;35(1):47-52. doi:10.1007/s00259-007-0577-0.
111. Kurihara H, Yang DJ, Cristofanilli M, et al. Imaging and dosimetry of ^{99m}Tc EC annexin V: Preliminary clinical study targeting apoptosis in breast tumors. *Appl Radiat Isot*. 2008;66(9):1175-1182. doi:10.1016/j.apradiso.2008.01.012.
112. Kartachova MS, Valdés Olmos RA, Haas RLM, Hoebbers FJP, van Herk M, Verheij M. *^{99m}Tc-HYNIC-Rh-Annexin-V Scintigraphy: Visual and Quantitative Evaluation of Early Treatment-Induced Apoptosis to Predict Treatment Outcome*. Vol 29. 2008. doi:10.1097/MNM.0b013e3282f1bc22.
113. Hoebbers FJP, Kartachova M, De Bois J, et al. ^{99m}Tc Hynic-rh-Annexin V scintigraphy for in vivo imaging of apoptosis in patients with head and neck cancer treated with chemoradiotherapy. *Eur J Nucl Med Mol Imaging*. 2008;35(3):509-518. doi:10.1007/s00259-007-0624-x.

114. Rottey S, Van den Bossche B, Slegers G, Van Belle S, van de Wiele C. Influence of chemotherapy on the biodistribution of [^{99m}Tc]hydrazinonicotinamide annexin V in cancer patients. *Q J Nucl Med Mol imaging Off Publ Ital Assoc Nucl Med [and] Int Assoc Radiopharmacol (IAR), [and] Sect Soc Radiopharm.* 2009;53(2):127-132. <http://www.ncbi.nlm.nih.gov/pubmed/19039304>. Accessed June 26, 2015.
115. Vermeersch H, Loose D, Lahorte C, et al. *^{99m}Tc-HYNIC Annexin-V Imaging of Primary Head and Neck Carcinoma*. Vol 25. 2004. doi:10.1097/00006231-200403000-00008.
116. Collingridge DR, Glaser M, Osman S, et al. In vitro selectivity, in vivo biodistribution and tumour uptake of annexin V radiolabelled with a positron emitting radioisotope. *Br J Cancer.* 2003;89(7):1327-1333. doi:10.1038/sj.bjc.6601262.
117. Keen HG, Dekker BA, Disley L, et al. Imaging apoptosis in vivo using ¹²⁴I-annexin V and PET. *Nucl Med Biol.* 2005;32(4):395-402. doi:10.1016/j.nucmedbio.2004.12.008.
118. Dekker B, Keen H, Lyons S, et al. MBP-annexin V radiolabeled directly with iodine-124 can be used to image apoptosis in vivo using PET. *Nucl Med Biol.* 2005;32(3):241-252. doi:10.1016/j.nucmedbio.2004.11.006.
119. Bauwens M, De Saint-Hubert M, Devos E, et al. Site-specific ⁶⁸Ga-labeled Annexin A5 as a PET imaging agent for apoptosis. *Nucl Med Biol.* 2011;38(3):381-392. doi:10.1016/j.nucmedbio.2010.09.008.
120. Smith G, Carroll L, Aboagye EO. New frontiers in the design and synthesis of imaging probes for PET oncology: current challenges and future directions. *Mol Imaging Biol.* 2012;14(6):653-666. doi:10.1007/s11307-012-0590-y.
121. Fani M, Maecke HR. Radiopharmaceutical development of radiolabelled peptides. *Eur J Nucl Med Mol Imaging.* 2012;39 Suppl 1:S11-S30. doi:10.1007/s00259-011-2001-z.
122. Vaidyanathan G, Zalutsky MR. Labeling proteins with fluorine-18 using N-succinimidyl 4-[¹⁸F]fluorobenzoate. *Int J Rad Appl Instrum B.* 1992;19(3):275-281. <http://www.ncbi.nlm.nih.gov/pubmed/1629016>. Accessed July 9, 2015.
123. Yagle KJ, Eary JF, Tait JF, et al. Evaluation of ¹⁸F-annexin V as a PET imaging agent in an animal model of apoptosis. *J Nucl Med.* 2005;46(4):658-666. doi:46/4/658 [pii].

124. Grierson JR, Yagle KJ, Eary JF, et al. Production of [F-18]Fluoroannexin for Imaging Apoptosis with PET. *Bioconjug Chem.* 2004;15(2):373-379. doi:10.1021/bc0300394.
125. Zijlstra S, Gunawan J, Burchert W. Synthesis and evaluation of a 18F-labelled recombinant annexin-V derivative, for identification and quantification of apoptotic cells with PET. *Appl Radiat Isot.* 2003;58(2):201-207. <http://www.ncbi.nlm.nih.gov/pubmed/12573319>. Accessed June 26, 2015.
126. Murakami Y, Takamatsu H, Taki J, et al. 18F-labelled annexin V: a PET tracer for apoptosis imaging. *Eur J Nucl Med Mol Imaging.* 2004;31(4):469-474. doi:10.1007/s00259-003-1378-8.
127. Hu S, Kiesewetter DO, Zhu L, et al. Longitudinal PET imaging of doxorubicin-induced cell death with 18F-annexin v. *Mol Imaging Biol.* 2012;14(6):762-770. doi:10.1007/s11307-012-0551-5.
128. Zhang X, Paule MG, Newport GD, et al. A minimally invasive, translational biomarker of ketamine-induced neuronal death in rats: microPET Imaging using 18F-annexin V. *Toxicol Sci.* 2009;111(2):355-361. doi:10.1093/toxsci/kfp167.
129. Zhu J-C, Wang F, Fang W, Hua Z-C, Wang Z. 18F-annexin V apoptosis imaging for detection of myocardium ischemia and reperfusion injury in a rat model. *J Radioanal Nucl Chem.* 2013;298(3):1733-1738. doi:10.1007/s10967-013-2667-8.
130. Tait JF, Smith C, Levashova Z, Patel B, Blankenberg FG, Vanderheyden J-L. Improved detection of cell death in vivo with annexin V radiolabeled by site-specific methods. *J Nucl Med.* 2006;47(9):1546-1553. doi:47/9/1546 [pii].
131. Li X, Link JM, Stekhova S, et al. Site-specific labeling of annexin V with F-18 for apoptosis imaging. *Bioconjug Chem.* 2008;19(8):1684-1688. doi:10.1021/bc800164d.
132. Lu C, Jiang Q, Hu M, Tan C, Yu H, Hua Z. Preliminary biological evaluation of ¹⁸F-FBEM-Cys-Annexin V a novel apoptosis imaging agent. *Molecules.* 2015;20(3):4902-4914. doi:10.3390/molecules20034902.
133. Reutelingsperger CPM, Moonen P, Vermaire A. Annexin derivatives suitable for pretargeting in therapy and diagnosis. June 2007. <https://www.google.com/patents/WO2007069895A1>. Accessed July 10, 2015.
134. Tait JF, Brown DS, Gibson DF, Blankenberg FG, Strauss HW. Development and characterization of annexin V mutants with endogenous chelation sites for ^{99m}Tc. *Bioconjug Chem.* 2000;11(6):918-925. doi:10.1021/bc000059v.

135. Wuest F, Berndt M, Bergmann R, van den Hoff J, Pietzsch J. Synthesis and application of [18F]FDG-maleimidehexyloxime ([18F]FDG-MHO): a [18F]FDG-based prosthetic group for the chemoselective 18F-labeling of peptides and proteins. *Bioconjug Chem.* 2008;19(6):1202-1210. doi:10.1021/bc8000112.
136. Wang K, Purushotham S, Lee J-Y, et al. In vivo imaging of tumor apoptosis using histone H1-targeting peptide. *J Control Release.* 2010;148(3):283-291. doi:10.1016/j.jconrel.2010.09.010.
137. Okarvi SM. Peptide-based radiopharmaceuticals: future tools for diagnostic imaging of cancers and other diseases. *Med Res Rev.* 2004;24(3):357-397. doi:10.1002/med.20002.
138. Lee S, Xie J, Chen X. Peptides and peptide hormones for molecular imaging and disease diagnosis. *Chem Rev.* 2010;110(5):3087-3111. doi:10.1021/cr900361p.
139. Aina OH, Liu R, Sutcliffe JL, Marik J, Pan C-X, Lam KS. From combinatorial chemistry to cancer-targeting peptides. *Mol Pharm.* 4(5):631-651. doi:10.1021/mp700073y.
140. Burtea C, Laurent S, Lancelot E, et al. Peptidic targeting of phosphatidylserine for the MRI detection of apoptosis in atherosclerotic plaques. *Mol Pharm.* 6(6):1903-1919. doi:10.1021/mp900106m.
141. Caberoy NB, Zhou Y, Alvarado G, Fan X, Li W. Efficient identification of phosphatidylserine-binding proteins by ORF phage display. *Biochem Biophys Res Commun.* 2009;386(1):197-201. doi:10.1016/j.bbrc.2009.06.010.
142. Hong H-Y, Choi JS, Kim YJ, et al. Detection of apoptosis in a rat model of focal cerebral ischemia using a homing peptide selected from in vivo phage display. *J Control Release.* 2008;131(3):167-172. doi:10.1016/j.jconrel.2008.07.020.
143. Laumonier C, Segers J, Laurent S, et al. A new peptidic vector for molecular imaging of apoptosis, identified by phage display technology. *J Biomol Screen.* 2006;11(5):537-545. doi:10.1177/1087057106288220.
144. Shao R, Xiong C, Wen X, Gelovani JG, Li C. Targeting phosphatidylserine on apoptotic cells with phages and peptides selected from a bacteriophage display library. *Mol Imaging.* 6(6):417-426. <http://www.ncbi.nlm.nih.gov/pubmed/18053412>. Accessed July 10, 2015.
145. Thapa N, Kim S, So I-S, et al. Discovery of a phosphatidylserine-recognizing peptide and its utility in molecular imaging of tumour apoptosis. *J Cell Mol Med.* 12(5A):1649-1660. doi:10.1111/j.1582-4934.2008.00305.x.

146. Xiong C, Brewer K, Song S, et al. Peptide-based imaging agents targeting phosphatidylserine for the detection of apoptosis. *J Med Chem.* 2011;54(6):1825-1835. doi:10.1021/jm101477d.
147. Kapy J, Banman S, Goping IS, Mercer JR. Evaluation of phosphatidylserine-binding peptides targeting apoptotic cells. *J Biomol Screen.* 2012;17(10):1293-1301. doi:10.1177/1087057112453313.
148. Kim S, Bae SM, Seo J, et al. Advantages of the Phosphatidylserine-Recognizing Peptide PSP1 for Molecular Imaging of Tumor Apoptosis Compared with Annexin V. *PLoS One.* 2015;10(3):e0121171. doi:10.1371/journal.pone.0121171.
149. Radermacher KA, Boutry S, Laurent S, et al. Iron oxide particles covered with hexapeptides targeted at phosphatidylserine as MR biomarkers of tumor cell death. *Contrast Media Mol Imaging.* 5(5):258-267. doi:10.1002/cmimi.382.
150. Burtea C, Ballet S, Laurent S, et al. Development of a magnetic resonance imaging protocol for the characterization of atherosclerotic plaque by using vascular cell adhesion molecule-1 and apoptosis-targeted ultrasmall superparamagnetic iron oxide derivatives. *Arterioscler Thromb Vasc Biol.* 2012;32(6):e36-e48. doi:10.1161/ATVBAHA.112.245415.
151. Kapy J, Kniess T, Wuest F, Mercer JR. Radiolabeling of phosphatidylserine-binding peptides with prosthetic groups N-[6-(4-[18F]fluorobenzylidene)aminoxyhexyl]maleimide ([18F]FBAM) and N-succinimidyl-4-[18F]fluorobenzoate ([18F]SFB). *Appl Radiat Isot.* 2011;69(9):1218-1225. doi:10.1016/j.apradiso.2011.05.012.
152. Song S, Xiong C, Lu W, Ku G, Huang G, Li C. Apoptosis imaging probe predicts early chemotherapy response in preclinical models: A comparative study with 18F-FDG PET. *J Nucl Med.* 2013;54(1):104-110. doi:10.2967/jnumed.112.109397.
153. Mäding P, Füchtner F, Wüst F. Module-assisted synthesis of the bifunctional labelling agent N-succinimidyl 4-[18F]fluorobenzoate ([18F]SFB). *Appl Radiat Isot.* 2005;63(3):329-332. doi:10.1016/j.apradiso.2005.03.005.
154. Cai W, Zhang X, Wu Y, Chen X. A thiol-reactive 18F-labeling agent, N-[2-(4-18F-fluorobenzamido)ethyl]maleimide, and synthesis of RGD peptide-based tracer for PET imaging of alpha v beta 3 integrin expression. *J Nucl Med.* 2006;47(7):1172-1180.
155. Berndt M, Pietzsch J, Wuest F. Labeling of low-density lipoproteins using the 18F-labeled thiol-reactive reagent N-[6-(4-[18F]fluorobenzylidene)aminoxyhexyl]maleimide. *Nucl Med Biol.* 2007;34(1):5-15. doi:10.1016/j.nucmedbio.2006.09.009.

156. Kniess T, Kuchar M, Pietzsch J. Automated radiosynthesis of the thiol-reactive labeling agent N-[6-(4-[¹⁸F]fluorobenzylidene)aminoxyhexyl]maleimide ([¹⁸F]FBAM). *Appl Radiat Isot.* 2011;69(9):1226-1230. doi:10.1016/j.apradiso.2011.03.043.
157. Wuest M, Perreault A, Kaptj J, et al. Radiopharmacological evaluation of ¹⁸F-labeled phosphatidylserine-binding peptides for molecular imaging of apoptosis. *Nucl Med Biol.* June 2015. doi:10.1016/j.nucmedbio.2015.06.011.
158. Blankenberg FG. In vivo detection of apoptosis. *J Nucl Med.* 2008;49 Suppl 2:81S - 95S. doi:10.2967/jnumed.107.045898.
159. Waterhouse RN. Determination of lipophilicity and its use as a predictor of blood-brain barrier penetration of molecular imaging agents. *Mol Imaging Biol.* 5(6):376-389. <http://www.ncbi.nlm.nih.gov/pubmed/14667492>. Accessed July 25, 2015.
160. Tait JF, Gibson DF, Smith C. Measurement of the affinity and cooperativity of annexin V–membrane binding under conditions of low membrane occupancy. *Anal Biochem.* 2004;329(1):112-119. doi:10.1016/j.ab.2004.02.043.
161. Zhao M, Beauregard DA, Loizou L, Davletov B, Brindle KM. Non-invasive detection of apoptosis using magnetic resonance imaging and a targeted contrast agent. *Nat Med.* 2001;7(11):1241-1244. doi:10.1038/nm1101-1241.
162. Yang DJ, Azhdarinia A, Wu P, et al. In vivo and in vitro measurement of apoptosis in breast cancer cells using ^{99m}Tc-EC-annexin V. *Cancer Biother Radiopharm.* 2001;16(1):73-83. doi:10.1089/108497801750096087.
163. De Saint-Hubert M, Mottaghy FM, Vunckx K, et al. Site-specific labeling of “second generation” annexin V with ^{99m}Tc(CO)₃ for improved imaging of apoptosis in vivo. *Bioorg Med Chem.* 2010;18(3):1356-1363. doi:10.1016/j.bmc.2009.12.021.
164. Fonge H, de Saint Hubert M, Vunckx K, et al. Preliminary in vivo evaluation of a novel ^{99m}Tc-labeled HYNIC-cys-annexin A5 as an apoptosis imaging agent. *Bioorg Med Chem Lett.* 2008;18(13):3794-3798. doi:10.1016/j.bmcl.2008.05.044.
165. Blankenberg FG, Katsikis PD, Tait JF, et al. Imaging of apoptosis (programmed cell death) with ^{99m}Tc annexin V. *J Nucl Med.* 1999;40(1):184-191.
166. Russell J, O’Donoghue JA, Finn R, et al. Iodination of Annexin V for Imaging Apoptosis. *J Nucl Med.* 2002;43(5):671-677. <http://jnm.snmjournals.org/login.ezproxy.library.ualberta.ca/content/43/5/671.long>. Accessed July 30, 2015.

167. Ohtsuki K, Akashi K, Aoka Y, et al. Technetium-99m HYNIC-annexin V: A potential radiopharmaceutical for the in-vivo detection of apoptosis. *Eur J Nucl Med.* 1999;26(10):1251-1258. doi:10.1007/s002590050580.
168. Jain RK. Barriers to drug delivery in solid tumors. *Sci Am.* 1994;271(1):58-65. <http://www.ncbi.nlm.nih.gov/pubmed/8066425>. Accessed April 30, 2015.
169. Goel S, Duda DG, Xu L, et al. Normalization of the vasculature for treatment of cancer and other diseases. *Physiol Rev.* 2011;91(3):1071-1121. doi:10.1152/physrev.00038.2010.
170. Heath VL, Bicknell R. Anticancer strategies involving the vasculature. *Nat Rev Clin Oncol.* 2009;6(7):395-404. doi:10.1038/nrclinonc.2009.52.
171. Blankenberg F. To scan or not to scan, it is a question of timing: technetium-99m-annexin V radionuclide imaging assessment of treatment efficacy after one course of chemotherapy. *Clin Cancer Res.* 2002;8(9):2757-2758. <http://www.ncbi.nlm.nih.gov/pubmed/12231512>. Accessed July 30, 2015.
172. Mandl SJ, Mari C, Edinger M, et al. Multi-modality imaging identifies key times for annexin V imaging as an early predictor of therapeutic outcome. *Mol Imaging.* 2004;3(1):1-8. doi:10.1162/153535004773861679.
173. Igarashi K, Kaneda M, Yamaji A, et al. A novel phosphatidylserine-binding peptide motif defined by an anti-idiotypic monoclonal antibody. Localization of phosphatidylserine-specific binding sites on protein kinase C and phosphatidylserine decarboxylase. *J Biol Chem.* 1995;270(49):29075-29078. <http://www.ncbi.nlm.nih.gov/pubmed/7493929>. Accessed August 1, 2015.
174. Mott HR, Carpenter JW, Zhong S, Ghosh S, Bell RM, Campbell SL. The solution structure of the Raf-1 cysteine-rich domain: a novel ras and phospholipid binding site. *Proc Natl Acad Sci U S A.* 1996;93(16):8312-8317. <http://www.pubmedcentral.nih.gov/articlerender.fcgi?artid=38667&tool=pmcentrez&rendertype=abstract>. Accessed August 2, 2015.
175. Improtta-Brears T, Ghosh S, Bell RM. Mutational analysis of Raf-1 cysteine rich domain: requirement for a cluster of basic aminoacids for interaction with phosphatidylserine. *Mol Cell Biochem.* 1999;198(1-2):171-178. <http://www.ncbi.nlm.nih.gov/pubmed/10497893>. Accessed August 2, 2015.
176. Maecke HR, Hofmann M, Haberkorn U. 68Ga-Labeled Peptides in Tumor Imaging. *J Nucl Med.* 2005;46(1_suppl):172S - 178. http://jnm.snmjournals.org/login.ezproxy.library.ualberta.ca/content/46/1_suppl/172S.long. Accessed August 2, 2015.

177. Kuchar M, Pretze M, Kniess T, Steinbach J, Pietzsch J, Löser R. Site-selective radiolabeling of peptides by (18)F-fluorobenzoylation with [(18F)]SFB in solution and on solid phase: a comparative study. *Amino Acids*. 2012;43(4):1431-1443. doi:10.1007/s00726-012-1216-z.
178. Fischer CA. Towards the optimization of tumor targeting radiolabeled peptides for molecular imaging and therapy. September 2014. http://edoc.unibas.ch/34088/1/Dissertation_Ch_Fischer.pdf. Accessed July 31, 2015.
179. Decristoforo C, Pickett RD, Verbruggen A. Feasibility and availability of ⁶⁸Ga-labelled peptides. *Eur J Nucl Med Mol Imaging*. 2012;39 Suppl 1:S31-S40. doi:10.1007/s00259-011-1988-5.
180. Fani M, Del Pozzo L, Abiraj K, et al. PET of somatostatin receptor-positive tumors using ⁶⁴Cu- and ⁶⁸Ga-somatostatin antagonists: the chelate makes the difference. *J Nucl Med*. 2011;52(7):1110-1118. doi:10.2967/jnumed.111.087999.
181. Li Z-B, Chen K, Chen X. (68)Ga-labeled multimeric RGD peptides for microPET imaging of integrin alpha(v)beta (3) expression. *Eur J Nucl Med Mol Imaging*. 2008;35(6):1100-1108. doi:10.1007/s00259-007-0692-y.
182. Liu Z, Li Z-B, Cao Q, Liu S, Wang F, Chen X. Small-animal PET of tumors with (64)Cu-labeled RGD-bombesin heterodimer. *J Nucl Med*. 2009;50(7):1168-1177. doi:10.2967/jnumed.108.061739.
183. Boswell CA, Sun X, Niu W, et al. Comparative in vivo stability of copper-64-labeled cross-bridged and conventional tetraazamacrocyclic complexes. *J Med Chem*. 2004;47(6):1465-1474. doi:10.1021/jm030383m.
184. Prasanphanich AF, Nanda PK, Rold TL, et al. [⁶⁴Cu-NOTA-8-Aoc-BBN(7-14)NH₂] targeting vector for positron-emission tomography imaging of gastrin-releasing peptide receptor-expressing tissues. *Proc Natl Acad Sci U S A*. 2007;104(30):12462-12467. doi:10.1073/pnas.0705347104.
185. Reubi JC, Maecke HR. Peptide-based probes for cancer imaging. *J Nucl Med*. 2008;49(11):1735-1738. doi:10.2967/jnumed.108.053041.
186. Liu Z, Yan Y, Liu S, Wang F, Chen X. (18)F, (64)Cu, and (68)Ga labeled RGD-bombesin heterodimeric peptides for PET imaging of breast cancer. *Bioconjug Chem*. 2009;20(5):1016-1025. doi:10.1021/bc9000245.
187. Liu Z, Niu G, Wang F, Chen X. (68)Ga-labeled NOTA-RGD-BBN peptide for dual integrin and GRPR-targeted tumor imaging. *Eur J Nucl Med Mol Imaging*. 2009;36(9):1483-1494. doi:10.1007/s00259-009-1123-z.

188. Reubi JC, Maecke HR. Peptide-based probes for cancer imaging. *J Nucl Med*. 2008;49(11):1735-1738. doi:10.2967/jnumed.108.053041.
189. Dahms P, Mentlein R. Purification of the main somatostatin-degrading proteases from rat and pig brains, their action on other neuropeptides, and their identification as endopeptidases 24.15 and 24.16. *Eur J Biochem*. 1992;208(1):145-154. <http://www.ncbi.nlm.nih.gov/pubmed/1355047>. Accessed August 2, 2015.
190. Nock BA, Maina T, Krenning EP, de Jong M. "To serve and protect": enzyme inhibitors as radiopeptide escorts promote tumor targeting. *J Nucl Med*. 2014;55(1):121-127. doi:10.2967/jnumed.113.129411.
191. Langer M, Beck-Sickinger AG. Peptides as carrier for tumor diagnosis and treatment. *Curr Med Chem Anticancer Agents*. 2001;1(1):71-93. <http://www.ncbi.nlm.nih.gov/pubmed/12678771>. Accessed August 3, 2015.
192. De Sá A, Matias AA, Prata MIM, Geraldes CFGC, Ferreira PMT, André JP. Gallium labeled NOTA-based conjugates for peptide receptor-mediated medical imaging. *Bioorg Med Chem Lett*. 2010;20(24):7345-7348. doi:10.1016/j.bmcl.2010.10.059.
193. Clarke ET, Martell AE. Stabilities of the Fe(III), Ga(III) and In(III) chelates of N,N',N"-triazacyclononanetriacetic acid. *Inorganica Chim Acta*. 1991;181(2):273-280. doi:10.1016/S0020-1693(00)86821-8.
194. Craig AS, Parker D, Adams H, Bailey NA. Stability, ⁷¹Ga NMR, and crystal structure of a neutral gallium(III) complex of 1,4,7-triazacyclononanetriacetate: a potential radiopharmaceutical? *J Chem Soc Chem Commun*. 1989;(23):1793. doi:10.1039/c39890001793.
195. Zhang H, Chen J, Waldherr C, et al. Synthesis and evaluation of bombesin derivatives on the basis of pan-bombesin peptides labeled with indium-111, lutetium-177, and yttrium-90 for targeting bombesin receptor-expressing tumors. *Cancer Res*. 2004;64(18):6707-6715. doi:10.1158/0008-5472.CAN-03-3845.
196. Richter S, Wuest M, Krieger SS, et al. Synthesis and radiopharmacological evaluation of a high-affinity and metabolically stabilized ¹⁸F-labeled bombesin analogue for molecular imaging of gastrin-releasing peptide receptor-expressing prostate cancer. *Nucl Med Biol*. 2013;40(8):1025-1034. doi:10.1016/j.nucmedbio.2013.07.005.
197. Mu L, Honer M, Becaude J, et al. In vitro and in vivo characterization of novel ¹⁸F-labeled bombesin analogues for targeting GRPR-positive tumors. *Bioconjug Chem*. 2010;21(10):1864-1871. doi:10.1021/bc100222u.

198. Höhne A, Mu L, Honer M, et al. Synthesis, ¹⁸F-labeling, and in vitro and in vivo studies of bombesin peptides modified with silicon-based building blocks. *Bioconjug Chem.* 2008;19(9):1871-1879. doi:10.1021/bc800157h.
199. Powell MF, Stewart T, Otvos L, et al. Peptide stability in drug development. II. Effect of single amino acid substitution and glycosylation on peptide reactivity in human serum. *Pharm Res.* 1993;10(9):1268-1273. <http://www.ncbi.nlm.nih.gov/pubmed/8234161>. Accessed August 4, 2015.
200. Werle M, Bernkop-Schnürch A. Strategies to improve plasma half life time of peptide and protein drugs. *Amino Acids.* 2006;30(4):351-367. doi:10.1007/s00726-005-0289-3.
201. Reubi JC. Peptide receptors as molecular targets for cancer diagnosis and therapy. *Endocr Rev.* 2003;24(4):389-427. doi:10.1210/er.2002-0007.
202. Wang X, Fani M, Schulz S, Rivier J, Reubi JC, Maecke HR. Comprehensive evaluation of a somatostatin-based radiolabelled antagonist for diagnostic imaging and radionuclide therapy. *Eur J Nucl Med Mol Imaging.* 2012;39(12):1876-1885. doi:10.1007/s00259-012-2231-8.
203. Ginj M, Zhang H, Waser B, et al. Radiolabeled somatostatin receptor antagonists are preferable to agonists for in vivo peptide receptor targeting of tumors. *Proc Natl Acad Sci U S A.* 2006;103(44):16436-16441. doi:10.1073/pnas.0607761103.
204. Nock B, Nikolopoulou A, Chiotellis E, et al. [^{99m}Tc]Demobesin 1, a novel potent bombesin analogue for GRP receptor-targeted tumour imaging. *Eur J Nucl Med Mol Imaging.* 2003;30(2):247-258. doi:10.1007/s00259-002-1040-x.
205. Alam IS, Neves AA, Witney TH, Boren J, Brindle KM. Comparison of the C2A domain of synaptotagmin-I and annexin-V as probes for detecting cell death. *Bioconjug Chem.* 2010;21(5):884-891. doi:10.1021/bc9004415.
206. Lee S, Xie J, Chen X. Peptides and peptide hormones for molecular imaging and disease diagnosis. *Chem Rev.* 2010;110(5):3087-3111. doi:10.1021/cr900361p.
207. Harris JM, Chess RB. Effect of pegylation on pharmaceuticals. *Nat Rev Drug Discov.* 2003;2(3):214-221. doi:10.1038/nrd1033.
208. Parry JJ, Andrews R, Rogers BE. MicroPET imaging of breast cancer using radiolabeled bombesin analogs targeting the gastrin-releasing peptide receptor. *Breast Cancer Res Treat.* 2007;101(2):175-183. doi:10.1007/s10549-006-9287-8.
209. Kiessling LL, Gestwicki JE, Strong LE. Synthetic multivalent ligands in the exploration of cell-surface interactions. *Curr Opin Chem Biol.* 2000;4(6):696-703. <http://www.ncbi.nlm.nih.gov/pubmed/11102876>. Accessed August 4, 2015.

210. Falciani C, Brunetti J, Pagliuca C, et al. Design and in vitro evaluation of branched peptide conjugates: turning nonspecific cytotoxic drugs into tumor-selective agents. *ChemMedChem*. 2010;5(4):567-574. doi:10.1002/cmdc.200900527.
211. Chen K, Conti PS. Target-specific delivery of peptide-based probes for PET imaging. *Adv Drug Deliv Rev*. 2010;62(11):1005-1022. doi:10.1016/j.addr.2010.09.004.
212. Richter S, Bouvet V, Wuest M, et al. (18)F-Labeled phosphopeptide-cell-penetrating peptide dimers with enhanced cell uptake properties in human cancer cells. *Nucl Med Biol*. 2012;39(8):1202-1212. doi:10.1016/j.nucmedbio.2012.06.003.
213. Kluba CA, Bauman A, Valverde IE, Vomstein S, Mindt TL. Dual-targeting conjugates designed to improve the efficacy of radiolabeled peptides. *Org Biomol Chem*. 2012;10(37):7594-7602. doi:10.1039/c2ob26127h.